Summer 8-14-2015

Development of Polymer Peptide Conjugates for Enhanced Pancreatic Cancer Imaging

Wen Shi
University of Nebraska Medical Center

DEVELOPMENT OF POLYMER PEPTIDE CONJUGATES FOR ENHANCED PANCREATIC CANCER IMAGING

BY

Wen Shi

A DISSERTATION

Presented to the Faculty of

the University of Nebraska Graduate College

in Partial Fulfillment of the Requirements

for the Degree of Doctor of Philosophy

Pharmaceutical Sciences Graduate Program

Under the Supervision of Professor Jered Garrison

University of Nebraska Medical Center

Omaha, Nebraska

July 2015

Supervisory Committee:

Surinder Batra, Ph.D.

Dong Wang, Ph.D.

Yazen Alnouti, Ph.D.

Table of Contents

Acknowledgements

First, I would like to thank my mentor, Dr. Jered Garrison, for his enthusiastic and tireless guidance throughout my Ph.D. studies. He has always been willing to share his knowledge, to answer my questions, to discuss details of my work and to emphasize on high standard and quality in my research. I also want to thank him for teaching me to be not just a good researcher but also a good listener and communicator. Without his support and patience, I would not have been able to overcome my limitations and so many difficulties. His creativity and his passion for research are always encouraging me to devote myself to the development of pharmaceutical sciences.

I would like to thank my supervisory committee members - Dr. Surinder Batra, Dr. Dong Wang and Dr. Yazen Alnouti for their valuable suggestions and helps. It's been a great honor and wonderful experience to work with and guided by such a group of talented professors. Their profound insight and critical review of my work and progress helped me grow as an independent scientist with critical thinking.

I would like to acknowledge all the past and present members in Dr. Garrison's lab. You all have been very supportive and helpful. My special thanks to our post-doctors Dr. Sunny Ogbomo and Dr. Nilesh Wagh for their consistent help during my graduate studies. They have always been patient to explain things to me and teach me a lot about chemical synthesis. I would like to thank Sonne (Zhengyuan Zhou), who came to the lab at the same time with me and worked with me for five years. His expertise in equipments and IT has been a great help to all. Thank Sue Brusnahan for her five years' dedicated support to my cell culture and animal work. Without her, many of these couldn't be achieved. Thank her for checking every abstract and manuscript I wrote. She's always a good teacher and a good friend.

I would like to thank all the faculty members from the Department of Pharmaceutical Sciences for teaching me a variety of useful courses, thank all the past and present staff members from College of Pharmacy, especially Ms. Katina Winters, Ms. Christine Allmon, Ms. Micelle Parks, Ms. Ashley Calhoon and Ms. Erin Plouzek for their generous support and indispensable help in administrative matters.

I would like to thank all the graduate students from the Department of Pharmaceutical Sciences. They are always kind and ready to help me. Special thanks to a few friends: thank my previous roommate Weike Ji. He’s a good researcher and great thinker. We always discussed scientific questions till midnight. Thank my best friend and partner Li Zheng, who always takes care of me and encouraged me when I was down.

Finally, I would like to thank the most important people - my parents. I am very sorry for being always from them for almost ten years now. Without their love, understanding and encouragement, I would not achieve all these. Thank you!

DEVELOPMENT OF POLYMER PEPTIDE CONJUGATES FOR ENHANCED PANCREATIC CANCER IMAGING

Wen Shi, Ph.D.

University of Nebraska, 2015

Supervisor: Jered Garrison, Ph.D.

Pancreatic ductal adenocarcinoma (PDAC) is the fourth leading cause of cancer-related deaths in the US with very poor prognosis. All clinically available biomarkers and diagnostic tools either fail to detect early stage PDAC or suffer from low specificity and sensitivity. There is an urgent need for diagnostic agents with greater efficacy for PDAC detection and staging. Nanomaterials such as N-(2-Hydroxypropyl) methacrylamide (HPMA) copolymers can effectively target tumors, and offer novel opportunities for the development of effective diagnostic agents for cancer. However, a major problem of many nanomaterials-based diagnostics is their opsonization and sequestration by the mononuclear phagocyte system (MPS), leading to substantial accumulation in MPS tissues such as the liver and spleen. This MPS accumulation in non-target tissues can hinder identification of resident or nearby metastatic malignant lesions thereby decreasing the diagnostic efficacy.

In this thesis, we focused on developing new approaches in which radiolabeled HPMA copolymers can be synthetically modified to significantly reduce the MPS accumulation and/or to increase the tumor accumulation, thereby enhancing the diagnostic and/or radiotherapeutic efficacy of the agents. First, we evaluated the effectiveness of incorporating metabolic active linkers into HPMA copolymers to decrease the radioactivity retention in the liver and spleen in pancreatic tumor xenograft

mice. We demonstrated that ^{177}Lu-labeled HPMA copolymers conjugated with cathepsin B/S cleavable peptide linkers exhibited significant long-term reduction in hepatic and splenic radioactivity accumulation as compared to the non-cleavable control. Next we conjugated a 109 kDa HPMA copolymer with three different cathepsin S cleavable linkers and evaluated the structure-activity relationship with regard to the lengths of the linking groups on the in vitro and in vivo efficacy of ^{177}Lu-labeled cathepsin S cleavable HPMA copolymers. Biodistribution results showed that the ^{177}Lu-labeled HPMA copolymer with the shortest length linker had a significant enhancement in the tumor-to-non-target ratios, which was also confirmed by SPECT/CT imaging. Finally, the potential of active tumor targeting for PDAC was evaluated using a plectin-1 targeted peptide (PTP) conjugated HPMA copolymer on pancreatic cancer cells in vitro. Unfortunately, we found that incorporation of the PTP into the HPMA copolymer diminished the binding of the peptide, possibly due to steric hindrance.

Overall, our ^{177}Lu-labeled cathepsin cleavable HPMA copolymer showed decreased MPS tissue accumulation and significant improvement in tumor-to-non-target organ ratio, and was successfully applied to SPECT/CT imaging of pancreatic tumors in a xenograft mouse model.

List of Figures

List of Tables

List of Abbreviations

PDAC	pancreatic ductal adenocarcinoma
PanIN	pancreatic intraepithelial neoplasia
MCN	mucinous cystic neoplasm
IPMN	intraductal papillary mucinous neoplasm
US	abdominal ultrasound
CT	computed tomography
MRI	magnetic resonance imaging
PET	positron emission tomography
EUS	endoscopic ultrasound
FDG	Fluorodeoxyglucose
MDCT	multi-detector-row computed tomography
SPECT	single-photon emission computed tomography
c(RGDfK)	cyclic arginine-glycine-aspartic acid-lysine peptide
RGD	arginine-glycine-aspartic acid peptide
RGD4C	double cyclized arginine-glycine-aspartic acid
EPR	enhanced permeability and retention
SPION	superparamagnetic iron oxide nanoparticles
uPAR	urokinase plasminogen activator receptor
EGFR	epidermal growth factor receptor
IO	iron oxide
QD	quantum dots
ScFvEGFR	single chain anti-EGFR antibody
HPMA	N-(2-Hydroxypropyl)methacrylamide
ATRP	the atom transfer radical polymerization
RAFT	reversible addition-fragmentation chain transfer polymerization

HER2	human epidermal growth factor receptor 2
APMA-CHX-A''-DTPA	N-methacryloylaminopropul-2-amino-3-(isothiurea-phenyl)-propylcyclohexane-1,2-diamine-N,N-N',N',N'',N''-pentaacetic acid
MA-GG-KCCYSL	N-methacryl-oylglycylglycyllysylcystyl-cystyltyrylserylleucine
APMA	N-(3-aminopropyl)methacrylamide
MA-Tyr	N-methacryloyl-tyrosinamide
^{99m}Tc	Technetium-99m
^{111}In	Indium-111
^{177}Lu	Lutium-177
^{90}Y	Yttrium-90
MA-GG-DPK	N-methacryloylglycylglycyl-(N-ω-bis(2-pyridylmethyl)-l-lysine
DTPA	Diethylene triamine pentaacetic acid
DOTA(tBu)$_3$	2-(4,7,10-tris(2-(tert-butoxy)-2-oxoethyl)-1,4,7,10 -tetraazacyclododecan-1-yl) acetic acid
DOTA	1,4,7,10-tetraazacyclododecane-1,4,7,10-tetraacetic acid
[^{18}F]FETos	2-[^{18}F]fluoroethyl-1-toylate
p.i.	post injection
MPS	mononuclear phagocyte system
i.t.	Intratumoral
i.v.	Intravenous
MA-GG-COOH	N-methacryloylglycylglyine
%ID/g	percentage injected dose per gram
LMA	lauryl methacrylate
PK1	HPMA-GlyPheLeuGly-Dox
PK2	HPMA-galactosamine-GlyPheLeuGly-Dox
NMR	nuclear magnetic resonance

SPPS	solid phase peptide synthesis
LC-MS	liquied chromatography-mass spectrometry
RP-HPLC	reverse phase-high performance liquid chromatography
MAL	metabolic active linker
HPAC	human pancreatic adenocarcinoma
CSL	cathepsin S cleavable linker
RPM	rounds per minute
SDS-PAGE	sodium dodecyl sulfate polyacrylamide gel electrophoresis
CSC	cathepsin S cleavable copolymer
APC	antigen presenting cells
PTP	plectin-1 targeted peptide
SEC	size exclusion chromatography
UV	Untraviolet
RI	refrective index
AzMA	N-(2-(2-(2-(2-azidoethoxy)ethoxy)ethoxy)-ethyl)methacrylamide
NHS	N-hydroxysuccinimide
EDC	1-Ethyl-3-(3-dimethylaminopropyl)carbodiimide
TFA	Trifluoroacetic acid
TIS	Thioanisole
DODT	3,6-dioxa-1,8-octanedithiol
DMF	Dimethylformamide
DCM	Dichloromethane

List of Contributors

1. Chapter 2 - Dr. Sunny Ogbomo synthesized the metabolic active linkers: MAL1 and MAL2. Sue Brusnahan cultured the HPAC and macrophage cells. The biodistribution study was performed in team work with Dr. Sunny Ogbomo, Dr. Nilesh Wagh, Dr. Zhengyuan Zhou and Susan Brusnahan.
2. Chapter 3 - Dr. Sunny Ogbomo synthesized the cathepsin S cleavable linkers CSL1-3. Sue Brusnahan cultured the HPAC and macrophage cells. The biodistribution study was performed in team work with Dr. Sunny Ogbomo, Dr. Nilesh Wagh, Dr. Zhengyuan Zhou, Yinnong Jia and Susan Brusnahan. Dr. Weike Ji assisted with the western blot study. Dr. Elizabeth Kosmacek performed the SPECT/CT imaging study.
3. Dr. Fan Wei synthesized the D-PTP-DO3A. Susan Brusnahan cultured the HPAC cells. Samantha Wall performed the flow cytometry analysis. Dr. Edward Ezell guided me with the ^{19}F NMR analysis.
4. All the chapters have been given major contribution involving designing and performing experiments by Wen Shi. The project was designed and guided by Dr. Jered Garrison.
5. The work was supported by COBRE grant to Dr. Jered Garrison, NIH funding to Dr. Jered Garrison and UNMC Fellowship to Wen Shi from 2013-2015.

Chapter 1

Introduction

1.1 PANCREATIC CANCER

Pancreatic ductal adenocarcinoma (PDAC) is the fourth leading cause of cancer-related death in the US with a median survival of <6 months and a dismal 5-years survival rate of 3%–5% [1]. This severe prognosis is mainly due to the cancer's aggressive clinical behavior with early invasion and metastasis as well as its resistance to conventional and targeted chemotherapeutics, leading to an initial diagnosis at an advanced and incurable stage in more than 80% patients [2].

PDAC commonly arises in the head region of the pancreas and infiltrates into nearby tissues including lymphatics, spleen, and peritoneal cavity, and metastasizes to the liver and lungs [3]. The disease is characterized by the presence of a dense stroma consisting of abundant extracellular matrix and mainly fibroblasts and inflammatory cells, termed desmoplasia [3]. Clinical and histopathologic studies have identified three PDAC precursor lesions (Figure 1.1): pancreatic intraepithelial neoplasia (PanIN), mucinous cystic neoplasm (MCN) and intraductal papillary mucinous neoplasm (IPMN) [4, 5]. The most common and best studied type is the PanIN, which can be graded from stages I to III, with the beginning stage characterized by the presence of columnar epithelial cells with increasing architectural disorganization and cytological changes through stages II and III [4, 6, 7]. High grade PanINs will ultimately progress into PDAC [3].

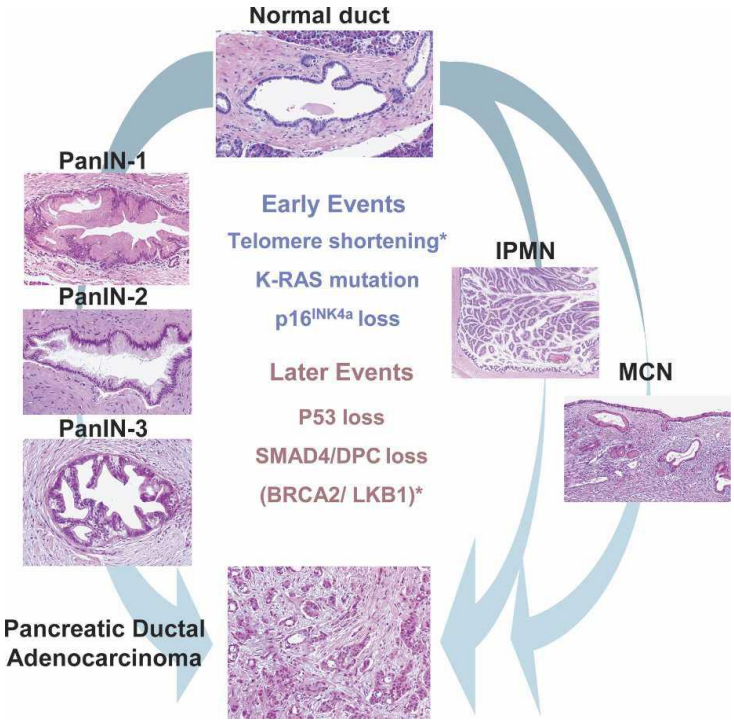

Figure 1.1: Pancreatic precursor lesions and genetic mutations involved in pancreatic adenocarcinoma progression. Adapted from Ref[3]. Pictured are three known human PDAC precursor lesions: PanIN, MCN, and IPMN. The PanIN grading scheme is shown on the left; increasing grade (1–3) reflects increasing morphology change, eventually leading to invasive adenocarcinoma. The right side shows the potential progression of MCNs and IPMNs to PDAC. The genetic alterations existing in adenocarcinomas also occur in PanIN, but to a lesser extent MCNs and IPMNs.

PDAC are highly resistant to conventional chemotherapy due to the impairment of drug delivery pathways caused by the hypovasculature within the tumor sites [8]. Besides, the surrounded stroma has been shown to induce resistance to chemotherapy and radiation therapy [9]. Gemcitabine is the standard chemotherapy for all stages of pancreatic adenocarcinoma in the last decade with the median overall survival of 6.7 months and a response rate as low as 7% [10]. Although there has been progress made in improving the various chemotherapeutic regimens and in the development of targeted therapies against pancreatic cancer, the overall survival has not been significantly improved.

1.2 CURRENT DIAGNOSTIC METHODS FOR PANCREATIC CANCER

Given the non-symptomatic nature of this disease, surgery is only a viable option for 15- 20% of PDAC patients with localized diseases [11]. Like many cancers, the earlier pancreatic cancer is detected, the more likely surgery will be successful and lead to longer patient survival. It was found that the 5-year survival of resectable PDAC is about 20%, increasing to 30% to 60% for node-negative tumors of less than 2 cm, and higher than 60% for small lesions less than 10 mm. More encouraging results come from patients who are diagnosed with high-grade dysplastic, but still noninvasive precursor lesions [12]. Large tumor size is directly related to poor prognosis. Early diagnosis of small or even pre-invasive cancers before the onset of metastasis offers the best hope for survival [13].

Unfortunately, all clinical available biomarkers and diagnostic tools fail to detect early stage PDAC and suffer from low specificity and sensitivity [14]. Blood biomarker

carbohydrate CA 19-9 is an oligosaccharide sialylated Lewis A antigen attached to mucin core proteins, and is the only available test in routine clinical use for PDAC [15]. But it is only used for PDAC patients' therapeutic management not diagnostic purposes, because only 50% of patients with small lesions (< 2 cm) presented with an increased CA19-9 value [16]. Also, this marker can be elevated in patients with other types of cancer [17] as well as in nonmalignant conditions including liver cirrhosis, cholangitis and chronic pancreatitis [18, 19]. Recent studies have identified some promising biomarkers from blood, saliva, stool and pancreatic juice [12]. But these biomarkers are still in the process of being validated in clinical trials.

Diagnostic imaging tools are highly valuable because they not only provide early detection but also enable appropriate treatment stratification (and staging) and in vivo therapeutic response monitoring. Imaging techniques currently applied for diagnosis and preoperative staging of pancreatic cancer include abdominal ultrasound (US), contrast-enhanced computed tomography(CT), magnetic resonance imaging (MRI), positron emission tomography (PET) and the minimal invasive endoscopic ultrasound (EUS) [20]. Below, we discuss the strengths and weakness of each imaging modality.

EUS allows the identification of diminutive structures with sizes ranging from 1-5 mm, including lymph nodes, bile ducts, pancreatic ducts, blood vessels, solid masses and cystic masses, so it is able to locate lymph node metastases and vascular tumor infiltration with high sensitivity [21]. However, EUS is an operator highly dependent technique and suffers from poor specificity for pancreatic cancer imaging [22]. The presence of pancreatitis like features such as cysts and solid nodules can lead to great doubt with regard to the importance of any discovered small pancreatic lesions [12].

Abdominal US is often used first to find out the reason for abdominal pain or jaundice. The sensitivity of conventional US for diagnosing PDAC is only 50–70% [23]. There are no characteristic signs for different kinds of pancreatic lesions including PDAC, chronic pancreatitis and endocrine cell tumors [20]. US might be an initial screening examination as it is a cost-effective method, but CT or MRI are still needed for further, more accurate diagnosis of malignant lesions [20].

CT is the most widely used imaging tool for the detection and staging of PDAC. Due to the abundance of fibrous stroma and hypovascularity in PDAC, non-contrast CT scans have very poor sensitivity and specificity [24]. Using contrast-enhanced CT, PDAC is poorly enhanced compared to the surrounding parenchyma in the early phase of dynamic CT but gradually enhanced with delayed images [20]. It's usually seen as a hypoattenuating area but may occasionally be seen as isoattenuating, thus resulting in misdiagnosis [24]. Although the sensitivity and specificity in diagnosis of PDAC by CT has been greatly improved recently (such as the introduction of multi-detector-row CT, MDCT), this modality still has difficulty in diagnosing PDAC at an early stage [25]. The difficulties are thought to be due to the small tumor size (<2 cm), loss of biliary dilatation, vascular involvement and mass effect, and little attenuation difference compared with normal pancreatic parenchyma [26].

MRI is commonly used to detect PDAC when a mass lesion is not detectable on CT scan as it provides better soft tissue contrast compared to non-contrast enhanced CT. However, there is no significant diagnostic advantage of MRI over contrast enhanced CT (sensitivity of 86% on CT vs. 84% on MRI) [27]. Combination of two modalities did not improve diagnostic efficacy relative to either one alone. Another problem with the use of

MRI for PDAC detection/staging is that chronic pancreatitis remained difficult to be differentiated from PDAC since both show enhanced contrast images on MRI and both may be associated with pancreatic ductal obstruction [28, 29]. The choice of MRI or CT may depend on the availability in hospitals and clinician's comfort with either modality.

PET imaging, using radiolabeled glucose analog ^{18}F-fluorodeoxyglucose (^{18}F-FDG), is a promising tool for noninvasive differentiation between benign and malignant lesions [30]. But the utility of PET in PDAC diagnosis and staging remains uncertain. Integrated PET/CT is considered superior to conventional imaging (MDCT, CT, EUS) used for tumor staging and identification of additional distant metastases (sensitivity and specificity rates were 81% versus 56% and 100% versus 95%, respectively, as reported in one study [31]). However, it has been argued that when compared to contrast enhanced MDCT, currently available data does not support that PET or PET/ CT provide any additional information for PDAC [24]. Additionally, chronic and acute pancreatitis and autoimmune pancreatitis can occasionally exhibit substantial FDG uptake and result in false positive results. Lastly, the sensitivity of ^{18}F-FDG PET in hyperglycemic patients could be lower than that in euglycemic patients because the elevated serum glucose levels suppress ^{18}F-FDG uptake in tumors by 50% due to the competitive inhibition [32].

The application of the single-photon emission computed tomography (SPECT) modality in PDAC is hampered by the lack of an effective radiotracer. Many radiotracers were reported in the literature, but these studies were limited to pre-clinical evaluation [14, 33, 34]. The $\alpha_v\beta_3$-integrin is often over-expressed in pancreatic tumor cells, whereas it is rarely expressed in normal pancreatic cells [35]. In one study, Indium-111 (^{111}In)-labeled DOTA-c(RGDfK) was evaluated in a hamster pancreatic carcinogenesis model

[33]. The c(RGDfK) is a cyclic, stable arginine-glycine-aspartic acid peptide analogue that binds with $\alpha_v\beta_3$-integrin with high affinity [36]. Using the radiolabeled peptide ^{111}In-DOTA-c(RGDfK), malignant lesions as small as 3mm in diameter could be clearly visualized in using SPECT/CT and the uptake of the radiolabeled peptide was found to be well correlated with $\alpha_v\beta_3$-integrin expression. In another study, Technetium-99m (^{99m}Tc) labeled integrin $\alpha_v\beta_6$-targeted peptide was found to effectively detect primary and metastatic lesions of $\alpha_v\beta_6$-positive pancreatic tumors [34]. Lastly, plectin-1 is a protein that is ubiquitously expressed in cells, but is normally constrained to the intracellular compartment. However, in the case of PDAC, plectin-1 becomes aberrantly expressed on the extracellular surface [14]. The peptide sequence KTLLPTP, discovered by phage display, was found to have submicromolar affinity for plectin-1 [37]. An ^{111}In-labeled-tetrametric form of plectin-1 targeting peptide exhibited high tumor uptake and visualized the primary and metastatic pancreatic tumors by SPECT/CT [14].

1.3 NANOMATERIALS FOR PANCREATIC CANCER IMAGING

The advancement in nanomedicine has sparked the development of emerging tools in cancer diagnostics and treatment [38]. Nanoparticles (1-100 nm in size), with carefully controlled chemistry, size, surface charge and other properties can delivery diagnostic and/or therapeutic agents to targeted locations in the body [39]. These nanoparticle systems include paradigms such as gold/magnetic nanoparticles, quantum dots, liposomes, polymer micelles, dendrimers, and polymer conjugates. In the case of cancer diagnosis and therapy, these nanoparticles can passively accumulate in tumors due to enhanced permeability and retention (EPR) effect [40]. The presence of larger than normal fenestrations in the tumor vasculature endothelial walls with the impairment of tumor lymphatic drainage system results in the retained accumulation of nanoparticles

[41]. Recent developments have led to the transformation from passive to active tumor targeting, which is normally achieved by covalently conjugating nanoparticles with cell-specific targeting ligands such as antibodies, small molecules or peptides [42]. Active targeting allows efficient intracellular accumulation of the anticancer therapeutic agents in specific tissues/cells which largely increase the efficacy [43]. PDAC expresses many different specific protein/receptors, making them potential biomarkers for targeted imaging and therapy [44].

A variety of nanoparticles have been investigated for pancreatic cancer imaging over the years [43]. Magnetic nanoparticles are biocompatible and have been used as contrast agents for MRI imaging for pancreatic cancer. For example, Hedgire et al. proved that using superparamagnetic iron oxide nanoparticles (SPION) as a contrast agent for MRI offered better delineation of pancreatic cancer in patients receiving preoperative imaging, which might contribute a roadmap for the surgeons [45]. Yang's group modified SPION with the urokinase amino-terminal fragment, which is a targeting ligand for the urokinase plasminogen activator receptor (uPAR) with high affinity [46]. uPAR is found to be highly expressed in pancreatic cancer cells and tumor stromal cells [47]. The modified nanoparticles produced significant MR signal changes in pancreatic tumor xenograft mice and allowed the distinction between malignant lesions and pancreatitis. Many pancreatic tumors highly express epidermal growth factor receptor (EGFR) [48]. Single chain anti-EGFR antibody (ScFvEGFR) has been conjugated to iron oxide (IO) magnetic nanoparticles, the resulting ScFvEGFR-IO nanoparticles selectively accumulated within the pancreatic tumors in an orthotopic pancreatic cancer xenograft model, as evidenced by an enhanced contrast in MRI signal in the area of the tumor [49].

A 4.8 fold MRI signal change was observed when comparing the ScFvEGFR-IO nanoparticles with the non-targeted IO nanoparticles.

Quantum dots (QD) are a class of semiconducting nanocrystals composed of inorganic cores and surrounding metal shells, with excellent optical properties [50]. They have been well studied for imaging pancreatic cancer [43]. Prasad's group attached many different targeting ligands including folic acid, cyclic arginine-glycine-aspartic acid (cRGD) and anti-mesothelin antibody, to CdTe quantum dots and successfully applied them for in vivo pancreatic cancer imaging [51-53]. Those QDs showed minimal toxicity in vivo and could target tumors with high signal-to-noise ratio, which allowed near infrared optical imaging of pancreatic tumors. ScFvEGFR conjugated quantum dots bound and internalized to EGFR positive pancreatic tumor cells and targeted efficiently to tumor in pancreatic tumor bearing mice while the non-targeted QD was almost undetectable in tumor [49]. These results suggest that QDs might be promising diagnostic agents for PDAC detection.

Liposomes have been successfully used as carriers for chemotherapeutics in clinic [54]. The development of liposome formulations has led to clinical trials investigating liposomal drug delivery systems for pancreatic cancer. Some of them have shown improved efficacy as compared to gemcitabine alone [55]. Liposomes have also been evaluated as pancreatic cancer diagnostic agents but only in animal models. Kato's group developed L-fucose-bound liposomes containing Cy 5.5 for effective near infrared optical imaging of CA19-9 expressing pancreatic tumors [56]. A multifunctional liposome platform conjugated with anti-mesothelin antibodies was loaded with SPION for MR imaging of pancreatic cancer. The in vivo imaging results showed that tumor signal

intensity dropped by 4 hour post injection (p.i.) and the decrease was much higher than free SPION without antibodies [57].

Many different polymers and polymer conjugates have been evaluated for pancreatic cancer imaging. Eser et al. developed a cathepsin-activatable, near-infrared probe based on PEG modified poly-l-lysine for pancreatic cancer imaging in a genetically mutated Kras mouse model [58]. The 35.5 kDa poly-l-lysine backbone was attached with 92 molecules of 5 kDa PEG and 11 molecules of Cy5.5. The fluorescence of the polymer conjugates was initially relatively low due to self-quenching, but could be substantially increased when cleaved by proteases. They identified increased expression of cathepsin proteases during pancreatic tumor progression. The elevated amount of cathepsins from PanIN lesions and early stage PDAC digested the accumulated conjugate in the tumor, thereby generating near-infrared fluorescence for pancreatic tumor imaging. They concluded that utilization of this technique enabled the detection and evaluation of early precursors of PDAC in vivo, holding great promise to improve early detection of PDAC. The Lammers' group prepared near infrared fluorophore labeled N-(2-Hydroxypropyl) methacrylamide (HPMA) copolymers and compared the active targeting RGD peptide conjugated HPMA copolymer with passive targeting HPMA copolymer modified with scrambled peptide DRG or without peptides in a pancreatic tumor xenograft model [59]. Interestingly they found that vascular targeting only worked in early time point at 1~2 h p.i., but passive targeting was more efficient at the long-term points (24~72 h). Work from Ghandehari's group demonstrated that pancreatic tumor targeting efficacy could be increased by utilizing hyaluronidase to break down the hyaluronic acid present in the PDAC stroma prior to the administration of ^{111}In-labeled, targeted HPMA copolymer [60].

1.4 RADIOLABELED HPMA COPOLYMERS FOR CANCER IMAGING AND RADIOTHERAPY

N-(2-Hydroxypropyl)methacrylamide or HPMA copolymers possess many distinct advantages including good biocompatibility and water solubility as well as prolonged in vivo circulation time. By means of EPR effect, these copolymers extravasate to tumor sites effectively and selectively [61]. The research on the use of HPMA copolymers as drug carriers started in the early 70s in Dr. Kopeček's laboratory [62]. To date, six HPMA conjugates have entered different stages of clinical trials, including two of them applied as theranostic agents (Table 1.1) [63]. Clinical trials have proven that HPMA conjugates were non-immunogenic and can be safely administered parenterally and exhibited anticancer activity. Given the high sensitivity of imaging modalities like SPECT and PET, radiolabeled HPMA copolymers have been successfully used to quantify the in vivo biodistribution of the copolymers and to visualize the tumor size and location for diagnostic imaging [61]. These agents can also serve as a platform to selectively deliver therapeutic doses of ionizing radiation to the tumor [64]. The application of radiolabeled HPMA copolymers for tumor imaging and radiotherapy is summarized here.

Table 1.1: HPMA-drug conjugates that have entered clinical trials. Modified from Ref[63].

Code	Compounds	Molecular Weight	Status
FCE 28068	HPMA-GFLG-doxorubicin	30,000	Phase I/II
FCE 28069	HPMA-galactosamine-GFLG-doxorubicin	25,000	Phase I/II
PNU 166945	HPMA-paclitaxel	N.A.	Phase I- stopped
PCNU 166148	HPMA-camptothecin	18,000	Phase I - stopped
AP5280	HPMA-carboplatinate analogue	25,000	Phase I/II
AP5346	HPMA-DACH platinate analogue	25,000	Phase I/II

1.4.1 Design and Structure of Radiolabeled HPMA Copolymer

The radiolabeled HPMA copolymer typically comprises at least three parts: a synthetic HPMA copolymer for prolonged circulation and tumor targeting; a polymer conjugated radionuclide chelator system to stably chelate the radioisotope, and the corresponding radionuclide for imaging or radiotherapy purpose. Different types of radionuclides utilized in HPMA copolymers, so far, with their respective characteristics and chelation systems utilized are summarized here in Table 1.2.

Table 1.2: Different radionuclides and their corresponding chelators applied in HPMA copolymers evaluated to date.

Radionuclide	Emission Type	Half-life	Emax (kev)	Chelator	Status	Ref
^{123}I	γ	13.3 h	159	tyrosine analogue	Phase 1	67,68,69,84,97
^{125}I	γ	60.1 d	35.5	tyrosine analogue	Pre-clinical	74,78
^{131}I	β^-, γ	8.04 d	β^-: 600 γ: 364	tyrosine analogue	Phase 1	69,73,75,76,94,96
^{99m}Tc	γ	6.02 h	140	DPK	Pre-clinical	70,77,90
^{111}In	γ	2.8 d	245	DTPA, DOTA	Pre-clinical	60,65,78,91
^{177}Lu	β^-, γ	6.7 d	β^-: 497 γ: 208	DOTA	Pre-clinical	66
^{90}Y	β^-	2.7 d	2280	DTPA	Pre-clinical	64,98
^{18}F	β^+	1.83 h	640	[^{18}F]FETos	Pre-clinical	71,80,81,86
^{72}As	β^+	26.0 h	3340	hydrosulfuryl	N.A.	72
^{74}As	β^+	17.8 d	1675	hydrosulfuryl	N.A.	72

There are two main approaches that can introduce the radionuclide chelators into HPMA copolymer: the co-polymerization method and the post-polymerization method. The co-polymerization method involves either free radical or controlled polymerization (e.g. the atom transfer radical polymerization (ATRP) and reversible addition-fragmentation chain transfer polymerization (RAFT)) of HPMA monomer, monomers containing the chelation system and other desired monomers. The polymerization is carried out in homogeneous solution phase and in the presence of radical initiators. The reaction is mostly initiated through heating (40 ºC to 80 ºC). Chain transfer agents can be added to better control the polydispersity and molecular weight. For example, to prepare the human epidermal growth factor receptor 2 (HER2) targeted ^{111}In-labeled HPMA copolymer, four monomers: HPMA monomer, a chelator containing monomer: N-methacryloylaminopropul-2-amino-3-(isothiurea-phenyl)propylcyclohexane-1,2-diamine-N,N-N',N',N'',N''-pentaacetic acid (APMA-CHX-A''-DTPA), the drug containing monomer N-methacryloylglycylphenyl-ananylleucylglycyl-gemcitabine and a HER2 targeted peptide conjugated monomer: N-methacryloylglycylglycyllysylcystyl-cystyltyrylserylleucine (MA-GG-KCCYSL) were dissolved together and RAFT polymerized for 24 hours using 2-cyano-2-propyl dodecyl trithiocarbonate as the chain transfer agent and 2,2'-azobis[2-(2-imidazolin-2-yl)propane] as the initiator (Figure 1.2) [65]. The copolymer was then radiolabeled with $^{111}InCl_3$ after heating at 50 ºC for 45 min in sodium acetate buffer. The radiolabeled copolymer was finally purified using size exclusion chromatography.

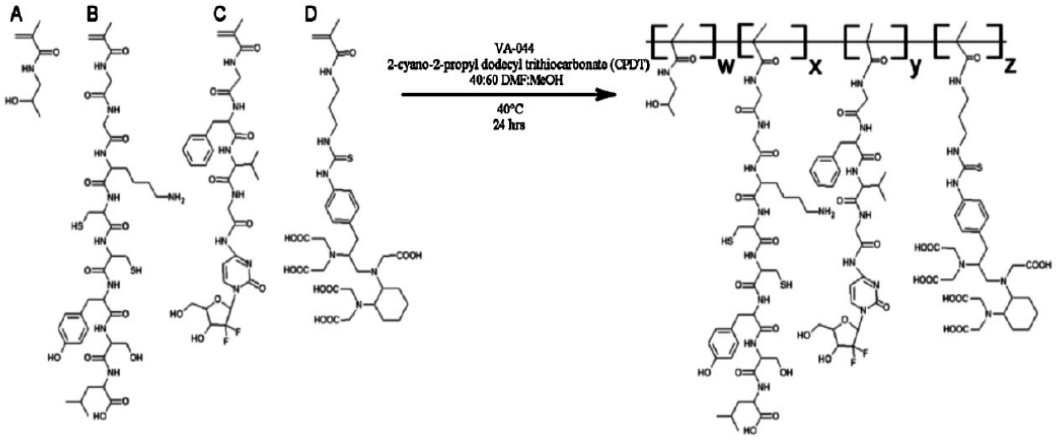

Figure 1.2: Preparation of ^{111}In-labeled HPMA copolymers by co-polymerization method. Adapted from Ref[65].

The co-polymerization method is quite straightforward. Many different functional monomers, modified with either a targeting moiety or therapeutic drugs, can be introduced at the same time with the chelation system. The content of each component in the copolymer can be controlled by adjusting the feeding ratios of each monomer. The resulting copolymer can be easily purified and characterized using size exclusion chromatography. One problem is that the preparation of many modified monomers may require expensive and time-consuming synthesis development.

The other method for the synthesis of a radiolabeled HPMA copolymer is the post-polymerization method. In this case, a copolymer precursor, containing a certain reactive functional group, is prepared after the polymerization step and subsequently conjugated to the chelation system. For example, HPMA and N-(3-aminopropyl)methacrylamide (APMA) were RAFT polymerized using 4,4'-azobis(4-cyanovaleric acid) as the initiator and 4-cyanopentanoic acid dithiobenzoate as the chain transfer agent (Figure 1.3) [66]. Activated 2-(4,7,10-tris(2-(tert-butoxy)-2-oxoethyl)-1,4,7,10-tetraazacyclododecan-1-yl) acetic acid (DOTA$(tBu)_3$) was conjugated to the primary amine functional groups from APMA. The amount of conjugated DOTA$(tBu)_3$ was determined by ninhydrin assay. The HPMA-DOTA conjugate was treated with TFA, to remove the t-butyl protecting groups before it was radiolabeled with Lutetium-177 (^{177}Lu) through heating at 90 ºC in water.

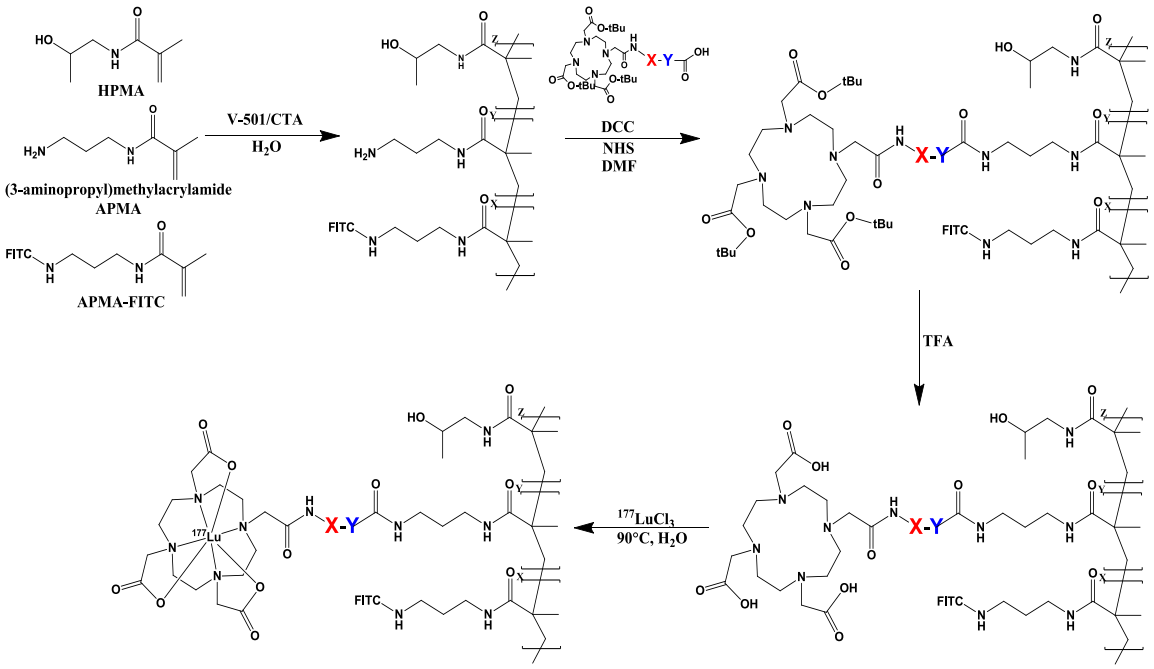

Figure 1.3: Preparation of ^{177}Lu-labeled HPMA copolymers by post-polymerization method. Adapted from Ref[66].

Post-polymerization is a relatively straightforward way to introduce the radionuclide chelator. However, the conjugation reaction efficiency can be adversely affected by the steric hindrance from randomly coiled polymer chains and the side chains of the other block components [61]. The degree of conjugation can be hard to control at times and additional characterizations are required to determine the conjugation efficiency. The characterization techniques may include colorimetric analysis, MS or NMR. The choice of co-polymerization or post-polymerization method depends on many factors, such as time, the availability of different functional monomers and the experimental purpose, and should be carefully selected in each case.

A variety of radionuclide chelators have been incorporated into HPMA copolymers. For the radioactive iodine labeled HPMA copolymer, tyrosine analogues are most commonly introduced in the modified monomer form (N-methacryloyltyrosinamide (MA-Tyr)) during the co-polymerization step [67-69]. The labeling is done under mild conditions by treatment of the copolymer with radioactive sodium iodine in the presence of an oxidizing reagent, to generate the electrophilic radio-iodine. The electrophilic species then react with the aromatic moiety of the compound to be labeled and form the radio-iodine-labeled copolymer.

For the preparation of ^{99m}Tc-labeled polymer, a monomer called N-methacryloylglycyl glycyl-(N-ω-bis(2-pyridylmethyl)-l-lysine) (MA-GG-DPK) was synthesized and introduced in the co-polymerization step [70]. N-ω-bis(2-pyridylmethyl)-l-lysine (DPK) can provide a compact tridentate coordination with ^{99m}Tc-tricarbonyl core and form very stable complexes. For most radio-metals, DTPA or DOTA analogues have been utilized [60,65, 66]. These macrocyclic chelators have good radiolabeling yield and can form stable

complexes with radio-metals. DTPA or DOTA moieties can be introduced in the co-polymerization step or by post-polymerization conjugation. However, one concern is that those macrocyclics themselves are rather bulky and mostly charged and as a result may influence the copolymer structure and consequently in vivo biological behavior [71].

For the most part, efforts in the pursuit of diagnostic HPMA copolymers have mainly focused on SPECT compatible radioisotopes. However, the last few years has seen an increase in the number of reports describing PET radionuclide incorporated into HPMA copolymers. Herth et al. prepared ^{18}F- labeled HPMA copolymers for short-term blood pool imaging [71]. They reacted 2-[^{18}F]fluoroethyl-1-toylate ([^{18}F]FETos) with the phenol group of a tyramine moiety from an HPMA copolymer after deprotonation of phenolic tyramine with a smaller amount of NaOH (Figure 1.4A). They reported radiochemical fluoroalkylation yields of ~80% for block copolymers and >50% for random polymers after a 10 min reaction at 120 °C. The synthesized ^{18}F-labeled HPMA copolymer could be purified and collected within 90 min. The same group also tried to label HPMA copolymers with the longer-living positron emitter Arsenic-72/74 ($^{72/74}$As) (Figure 1.4B) [72]. HPMA copolymers were prepared by RAFT polymerization, using the dithiobenzoic ester as the chain transfer agent. The end group in each copolymer, coming from the chain transfer agent was converted to -SH group after reduction with tris(2-carboxyethyl) phosphine treatment. $^{72/74}$As-labeling of HPMA was carried out in water at 70 ºC with increased labeling yields after longer incubation.

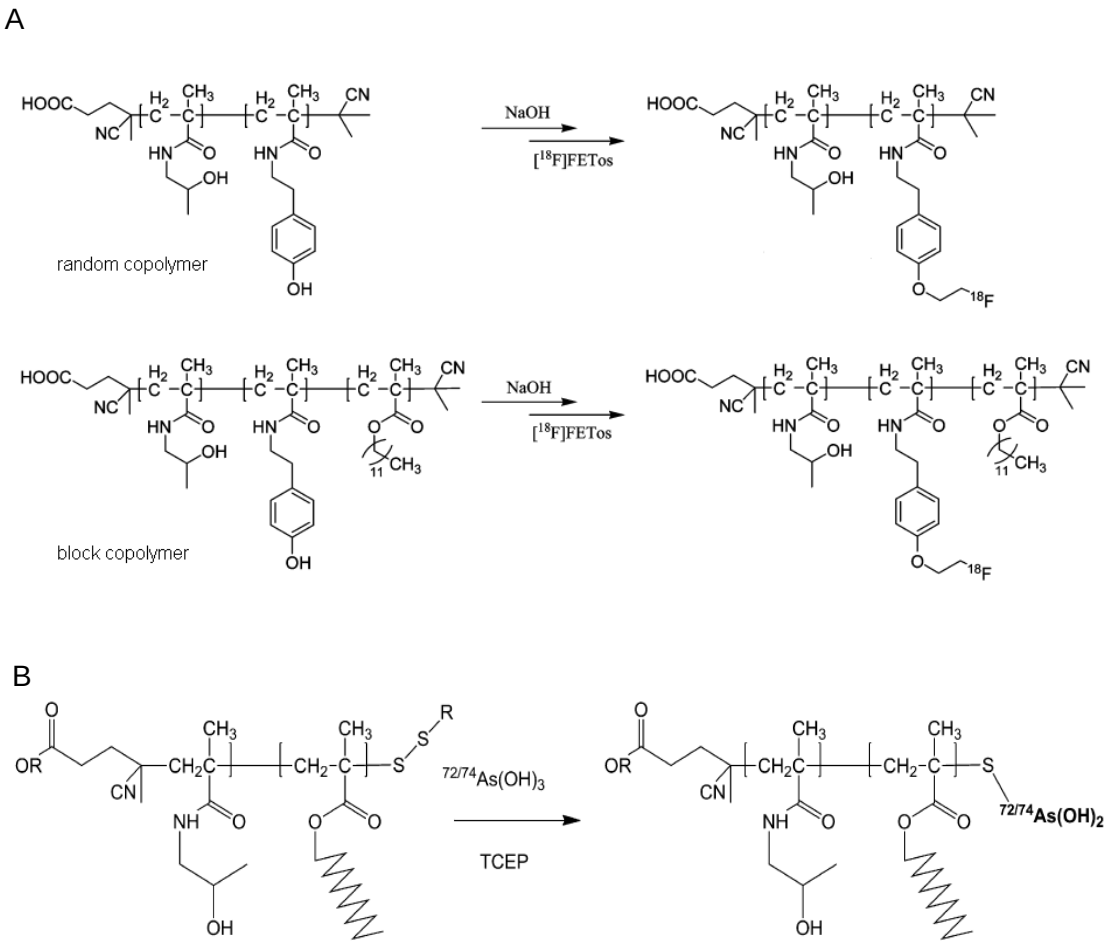

Figure 1.4: Preparations of ^{18}F-radiolabeled HPMA copolymers for PET imaging. Adapted from Ref [72]

1.4.2 Preclinical Evaluation of Radiolabeled HPMA Copolymers in Animal Models

Various radiolabeled HPMA copolymers have been evaluated in different animal models and have shown great potential as tumor imaging agents. With respect to tumor targeting mechanism, those copolymers can be briefly categorized into two types: the passive tumor-targeting HPMA copolymers and the active tumor-targeting HPMA copolymers. The following part will mainly discuss about the design and in vivo performances of different kinds of radiolabeled HPMA copolymers in animal models:

Passive tumor-targeting HPMA copolymers

Early studies have assessed the in vivo pharmacokinetics and imaging characteristic of HPMA copolymer labeled with different radioiodines (^{123}I, ^{125}I and ^{131}I) [67-69, 73]. The biodistribution of the radioactive conjugates in tumor xenograft mice were monitored using the gamma scintigraphy and also by ex vivo biodistribution measurements.[67] There was a clear relationship between the copolymer molecular weight and body clearance and tumor uptake of HPMA copolymers [73]. It was found that the urinary excretion of radioactivity was dependent on the molecular weight of the copolymer. HPMA copolymers with molecular weight below the renal threshold (~45 kDa) cleared mostly through the renal system, which lead to the kidney containing the highest radioactive content [68]. Contrastingly, high molecular weight (Mw) HPMA copolymers were predominately cleared by the mononuclear phagocyte system (MPS) and the hepatobiliary system, leading to retention in the liver and spleen. The tumor uptake displayed continuous increase with time even after 72 h and was much higher as compared to the low molecular weight HPMA copolymer.

The biodistribution of HPMA copolymers can be easily affected by the other components in the copolymer. Biotin-labeled HPMA copolymers were initially prepared to investigate the cellular localization of HPMA copolymers in normal and tumor tissues. However, it was found that biotinylation could significantly alter the biodistribution, which was assessed by ^{125}I-labeled HPMA copolymers [74].The biotinylated HPMA copolymer cleared faster from the circulation than the unmodified HPMA copolymer of comparable molecular weight and had lower accumulation in the liver, spleen and tumor. The kidney uptake was 33 times higher for the biotinylated HPMA copolymer possibly due to the presence of biotin transporters in the brush border membrane.

Lammers et al. used the scintigraphic imaging method to investigate the influence of the incorporation of various functional groups into ^{131}I-labeled HPMA copolymers on the whole-body distribution and tumor accumulation of the copolymers [75]. They prepared ten functionalized HPMA copolymers and evaluated the in vivo behaviors in AT1 tumor bearing rats. The authours found that the incorporation of carboxyl and hydrazide groups, as well as introduction of spacer, drug and peptide moieties reduced the long-circulating properties of the copolymers thereby lowering the accumulation in tumors and in all tissues except for kidney. But tumor-to-organ ratios were comparable to unmodified controls for the majority of the chemically modified copolymers. It was concluded that functionalization did not affect the tumor targeting ability of the copolymers (Figure 1.5).

	I: pHPMA 23 kDa	**II**: pHPMA 31 kDa	**III**: pHPMA 65 kDa	**IV**: 3% -COOH 34 kDa	**V**: 3% -$NHNH_2$ 29 kDa	**VI**: 8% -COOH 21 kDa	**VII**: 8% -$NHNH_2$ 19 kDa
Tumor	1	1	1	1	1	1	1
Spleen	0.4	0.4	0.5	0.4	0.3	0.4	0.3
Lung	0.6	1.0	2.4	1.0	0.7	0.6	0.5
Kidney	2.0	3.3	6.4	2.1	0.8	0.8	0.2
Liver	1.4	1.6	3.1	1.5	1.1	1.0	1.0
Testis	1.9	2.0	3.4	2.1	1.8	1.8	2.3
Heart	3.4	3.5	5.5	2.9	2.6	3.1	2.4
Skin	3.9	5.5	8.9	4.1	1.8	2.3	1.7
Ileum	6.3	5.7	7.1	5.7	3.9	4.2	3.4
Muscle	13.0	20.1	22.4	11.7	9.3	7.8	3.3

	II: pHPMA Control	**VIII**: pHPMA-GG-Dox	**IX**: pHPMA-GFLG-OH	**X**: pHPMA-GFLG-Dox	**XI**: pHPMA-GG-PHSCN	**XII**: pHPMA-GG-AHX-PHSCN	**XIII**: pHPMA-GG-PEG-PHSCN
Tumor	1	1	1	1	1	1	1
Spleen	0.4	0.5	0.4	0.6	0.3	0.1	0.2
Lung	1.0	0.9	0.8	0.8	0.8	0.6	0.9
Kidney	3.3	1.2	0.5	0.1	0.06	0.04	0.06
Liver	1.6	1.7	2.0	1.9	0.7	0.4	0.8
Testis	2.0	2.4	2.5	2.9	1.8	1.4	2.4
Heart	3.5	3.7	4.2	4.6	1.3	1.2	1.2
Skin	5.5	4.4	4.6	4.3	0.9	0.6	1.6
Ileum	5.7	5.3	4.6	4.5	2.4	1.0	3.9
Muscle	20.1	12.6	12.6	12.1	4.4	3.6	6.3

Figure 1.5: Evaluation of the tumor to organ ratio of HPMA copolymers with different functional groups at 168 h p.i. indicated that except for the pentapeptide PHSCN, other functional groups did not reduce the relative tumor targeting ability. Adapted from Ref[75].

The administration route could also affect the tumor accumulation of radiolabeled HPMA copolymers. Lammers et al. compared the effect of intratumoral (i.t.) injection versus intravenous (i.v.) injection on the biodistribution of HPMA copolymers in prostate tumor bearing rats [76]. HPMA-MA-Tyr copolymers with different molecular weight were labeled with ^{131}I in high efficiency. It was found the i.t. injected HPMA copolymers had significantly less blood radioactivity as compared to those from i.v. injection. The tumor to organ ratios from i.t. injection were 5 times higher for the 31 kDa copolymer and up to 20 times higher for the 65 kDa copolymer compared to those from i.v. injection. Based on the findings, they suggested i.t. injection of polymer-based chemotherapy as an alternative to routine administration routes.

Radioiodine has a number of disadvantages, which may limit its translational application for the HPMA copolymer based radiopharmaceuticals. ^{125}I emits low-energy gamma rays with low tissue penetration that could limit its application in human. ^{131}I has high gamma emission energy (364 keV) and ionizing radiation associated with its beta emission, so it's not generally used for diagnostic imaging. ^{123}I is more suitable than the aforementioned radionuclides for clinical imaging, but it is relatively expensive to produce [77]. Given the wide use of Technetium-99m in clinic for nuclear imaging and its ideal imaging energy, ^{99m}Tc-labeled HPMA copolymers were developed and evaluated in vivo. Ghandehari's group prepared ^{99m}Tc-labeled HPMA copolymers of various charges and molecular weights at 7, 21 and 70 kDa and determined their biodistribution in non-tumor bearing mice [77]. Neutral HPMA copolymers contained 95% HPMA and 5% MA-GG-DPK while negatively charged HPMA copolymers contained 70% HPMA, 5% MA-GG-DPK, 23% N-methacryloylglycylglyine (MA-GG-COOH) and 2% MA-Tyr. The 7 kDa negatively charged copolymer showed 8.1 ± 0.74% ID/g in the kidney at 24 h, while

higher renal activity was found for the 21 kDa and 70 kDa copolymer, which showed 33.1 ± 1.6% and 23.3 ± 4.8% ID/g, respectively. At 24 h, the 70 kDa electronegative copolymer had little accumulation in the blood (1.5 ± 0.3% ID/g), spleen (1.4 ± 0.7% ID/g), and liver (2.2 ± 0.6% ID/g) while the other two showed < 1%ID/g in all tissues. For neutral copolymers, higher molecular weight showed longer circulation time and higher tissue retention, which is consistent with radioiodine labeled HPMA copolymers. At 24 h, the neutral 7 kDa copolymer had some hepatic (5.3 ± 1.7% ID/g) and splenic retention (5.9± 1.9% ID/g). The 21 kDa copolymer showed high renal (18.3 ± 6.9%ID/g) and splenic retention (10.3 ± 1.3% ID/g). The 70 kDa copolymer showed the highest blood activity (19.2 ± 4.2% ID/g) and retention in lung (12.8 ± 3.1% ID/g), spleen (14.9 ± 4.5% ID/g), and liver (25.3 ± 2.8% ID/g). Overall, all three negatively charged copolymer were more efficiently cleared from the body than the neutral copolymers and did not, with exception to the kidneys, exhibit substantial, long-term retention in any major tissues.

More recently, HPMA copolymer labeled with different radiometals through coordination with DOTA or DTPA were evaluated in mice. Garrison's group synthesized a 343 kDa HPMA-APMA copolymer and conjugated it with DOTA$(tBu)_3$. The copolymer was successfully labeled with ^{177}Lu after deprotection with TFA. The radiolabeled HPMA copolymer was mainly eliminated by the MPS and its high molecular weight resulted in high blood and tumor radioactivity after 72 h p.i. [66].

Dr. Kopecek's group recently developed a series of backbone degradable HPMA copolymers. A 109 kDa HPMA copolymer was first RAFT synthesized, and then was extended to a 335 kDa backbone degradable HPMA conjugate through a cathepsin B cleavable linker using "click chemistry" [78]. The copolymer was radiolabeled with ^{125}I to

permit pharmacokinetic and imaging studies in mice. SPECT/CT imaging in mice bearing orthotopic ovarian tumor demonstrated biodegradability and elimination of the backbone degradable HPMA from the body. In the next study, they applied duallabeling to a 110 kDa backbone degradable HPMA copolymer to separately investigate the behavior of the carrier and payload [79]. The HPMA copolymer backbone was labeled with ^{125}I and the ^{111}In-DTPA complex was attached at the GFLG side-chain termini and served as the drug model. SPECT/CT imaging results demonstrated that payload (^{111}In) had similar blood half-life and tissue uptake as polymeric carrier (^{125}I), which indicated that the GFLG bond was stable in blood circulation. This “second generation” high-molecular weight backbone-degradable HPMA copolymer showed five- (^{111}In) to eight- (^{125}I) times higher tumor accumulation as compared to the “first-generation” backbone non-degradable low molecular weight (< 50 kDa) conjugates.

The in vivo behavior of ^{18}F-labeled HPMA copolymer has also been investigated in mice, but mainly in the early time points. Different molecular weights of either HPMA homopolymer or HPMA-ran-LMA (LMA = lauryl methacrylate) copolymer was synthesized and labeled with [^{18}F]FETos [80]. HPMA-ran-LMA copolymers could form aggregates in ~ 40nm size above their critical micelle concentration. The copolymer was less efficiently labeled as compared to the homopolymer, presumably due to the lower accessibility of phenolic groups in the interior of the polymer coils. MicroPET imaging was utilized over 2 h period of time after i.v. injection of the labeled polymers. The ex vivo biodistribution study was carried out at 2 h after i.v. injection and it was found that independently from the molecular weight, the HPMA-ran-LMA copolymer showed longer blood circulation, and the uptake of the larger Mw copolymer by the liver and spleen was much lower than that of the comparable homopolymer, which was also confirmed by the

PET imaging results. It was assumed that that the incorporation of the hydrophobic lauryl methacrylate block had significant impact on the biodistribution and helped avoid the uptake of the polymers by the MPS.

The same group also studied the effect of PEGylation on the in vivo behavior of ^{18}F labeled HPMA-b-LMA copolymer [81]. Different amounts of PEG 2000 were grafted to the polymer backbone from 0% to 11% while the ratio of polymerization with HPMA and LMA monomer was kept constant. The copolymer was labeled with ^{18}F with a relatively low yield of less than 20%. Non-invasive PET imaging over 2h and quantification by ex vivo biodistribution measurements at 2 h and 4h p.i. were performed on mammary carcinoma bearing rats. The study showed that the lower PEG content copolymer had major kidney and MPS uptake with comparatively low blood retention as well as tumor accumulation while higher PEG content caused prolonged blood circulation times and led to a tumor accumulation constantly increasing with the increased amount of PEG.

Active tumor-targeting HPMA copolymers

Distinct from passive tumor targeting HPMA copolymers, active tumor targeting HPMA copolymers have been conjugated with different targeting ligands, including small molecules, peptides and antibodies with the aim of improving tumor-targeting efficacy. Many of these targeted HPMA copolymers have been radiolabeled and evaluated by nuclear imaging studies.

The galactose receptor is highly expressed on liver hepatocytes [82]. Galactosamine, which was the first small molecule ligand conjugated to an HPMA copolymer, has good

affinity to the galactose receptor. As a consequence, HPMA-galactosamine conjugates have been investigated for liver-targeted drug delivery [83]. The galactose receptor-targeted HPMA copolymer was labeled with a variety of radioiodines (^{123}I, ^{125}I, ^{131}I) for biodistribution and gamma scintigraphy studies [69, 84]. Substantial hepatic accumulation of the galactosamine conjugated HPMA copolymer was seen as early as 20 min p.i., which confirms the liver-targeting capability of galactosamine conjugated HPMA copolymers.

Folate receptor is over-expressed on many different types of cancer cells including breast cancer, while its expression in healthy tissues and organs is limited [85]. The potential of folate receptor-targeted HPMA copolymers was evaluated in mammary tumor bearing rats [86]. HPMA copolymer of 10.5 and 52.5 kDa were functionalized with folate through copper catalyzed “click chemistry” and labeled with ^{18}F as described in section 1.4.1. In vivo biodistribution and micro-PET imaging studies revealed a 1.5 to 2 fold increase in tumor accumulation at the 2 and 4 h time-points for the folate-conjugated HPMA copolymer relative to the non-targeted HPMA copolymer control. The increased accumulation could be blocked by co-administration of native folic acid with ^{18}F-labeled folate-HPMA copolymer. This work demonstrated the effectiveness of folate-conjugated HPMA copolymers for folate receptor positive tumor-targeting.

Angiogenesis in tumor sites is critical for tumor growth and metastasis [87]. Targeting angiogenesis is an important area in tumor diagnosis and targeted therapy [88]. Tumor blood vessels highly express $\alpha_v\beta_3$ integrin receptors, which can be targeted by the RGD peptides. Numerous reports on the RGD peptides and analogues have demonstrated the in vivo efficacy of this integrin-targeted peptide [89]. A decade ago, RGD peptides

were firstly conjugated to HPMA copolymers in order to evaluate the potential of these integrin-targeted agents. ^{99m}Tc-labeled HPMA copolymer bearing a double cyclized RGD analogue (RGD4C) or a non-targeted control (RGE4C) was synthesized and evaluated in a DU-145 prostate tumor xenograft mouse model [70]. Based on this report, the HPMA-RGD4C conjugate had almost 4 times higher tumor accumulation (4.60 ± 1.80% ID/g) than the non-integrin-targeted HPMA copolymer (1.24 ± 0.15% ID/g) from the 24 h scintigraphic image results (Figure 1.6). The targeted copolymer had sustained tumor retention over a 72 h period with substantial clearance from non-target tissues. In addition, the authors also compared the biodistribution of ^{99m}Tc labeled HPMA-RGD4C conjugate with ^{99m}Tc labeled RGD4C peptide [90]. They found that the liver and spleen uptake at 24 h was higher for the radiolabeled peptide compared to polymer peptide conjugate, which might be due to reduced extravasation of the targeted polymeric conjugates in normal tissues.

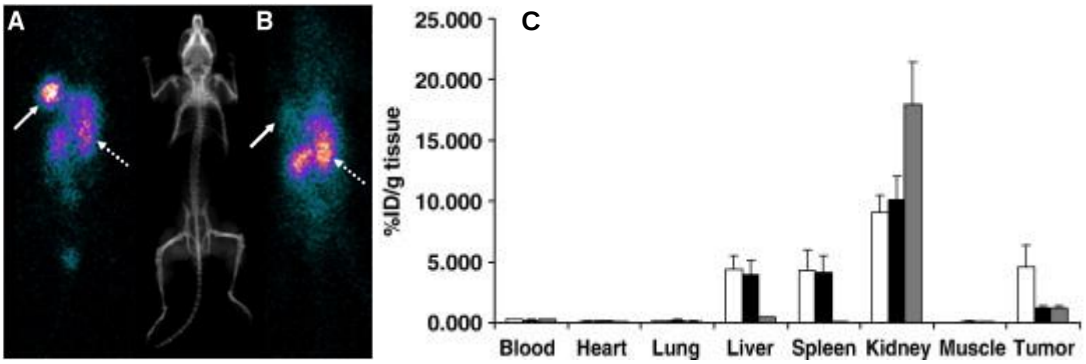

Figure 1.6: A, scintigraphic image of ^{99m}Tc-labeled HPMA-RGD4C conjugate in a DU-145 xenograft mouse model at 24 h p.i. B, scintigraphic image of ^{99m}Tc-labeled HPMA-RGE4C conjugate in a DU-145 xenograft mouse model at 24 h p.i. C, biodistribution of three different ^{99m}Tc-labeled copolymers (white: HPMA-RGD4C, black: HPMA-RGE4C and grey: HPMA homopolymer) in a DU-145 xenograft mouse model at 24 h p.i. Adapted from Ref[70].

RGD4C peptide is susceptible to degradation in vivo. To solve the stability issue associated with RGD4C, Ghandehari's group attached a stable cyclic RGD analogue, RGDfK, to the HPMA copolymer, and compared it with the RGD4C-HPMA conjugate [91]. After labeling both with ^{111}In, the in vivo efficacy of the $\alpha_v\beta_3$–targeted HPMA copolymers were evaluated in a LLC1 xenograft lung carcinoma mouse model. Both showed significant tumor accumulation after 24 h p.i. with peak accumulations at 4.9 ± 0.9% and 5.0 ± 1.2% ID/g, respectively. There was no statistical difference in tumor and non-target tissues retention between the two peptide copolymer conjugates.

Ghandehari's group developed peptide conjugated HPMA copolymers for active targeting of HER2 positive pancreatic tumors [60]. The HPMA copolymer was conjugated with the HER2 targeted peptide (KCCYSL) by aminolysis and was radiolabeled with ^{111}In using the DTPA chelator. Pancreatic tumors are characterized by the existence of dense stroma consisting of abundant hyaluronic acid, which prevents the diffusion of macromolecules. Their work demonstrated that the targeting efficacy of the HER2 targeted HPMA copolymer could be increased 2-3 fold after utilizing hyaluronidase prior to the injection of the radiolabeled copolymer. Hyaluronidase broke down the hyaluronic acid in the stroma thereby increasing the extravasation of HER2 targeted HPMA copolymers into pancreatic tumors.

Prostate tumors can over-express galectin-3 [92]. The G3-C12 peptide, with the sequence of ANTPCGPYTHDCPVKR, was discovered by phage display and has specific binding affinity galectin-3 [93]. Huang's group developed the prostate carcinoma targeting HPMA copolymer conjugated with 3 mole% the G3-C12 peptide and labeled it with ^{131}I [94]. Scintigraphic imaging was used to visualize the biodistribution of the peptide

modified copolymers and control copolymer (without peptide) in a PC-3 prostate tumor xenograft mouse model. It is important to note that both the targeted and the control HPMA have analogous molecular weights. At 2 h and 24 h p.i., the ^{131}I-labeled G3-C12 HPMA copolymer conjugate had significantly higher tumor accumulation (1.60 ± 0.08% ID/g and 1.04 ± 0.19% ID/g) as compared to the non-target HPMA copolymer (1.19 ± 0.04% ID/g and 0.36 ± 0.04% ID/g), implying the active tumor targeting effects of the G3-C12 peptide in the HPMA copolymer paradigm.

1.4.3 In Vivo application in human patients

Based on many promising preclinical findings, in 1994, HPMA-GlyPheLeuGly-Dox (PK1) became the first applied passively tumor-targeted polymeric prodrug to enter clinical trials [95] and was given by i.v. administration to 36 patients with different types of tumors [96]. As part of the clinical investigation of PK1, planar scintigraphy imaging studies using ^{131}I- and ^{123}I-labeled PK1 was utilized to quantify the in vivo biodistribution and to visualize its tumor uptake. The tumor uptake of ^{131}I-labeled PK1 allowed for clear visualization of the primary cancer in a number of patients. The scintigraphy study clearly showed the clearance of the 28 kDa radiolabeled HPMA copolymer from the body through renal filtration. ^{123}I-labeled PK1 was found to localize into the metastatic lesions of some patients. For example, a large metastasis was observed in the left shoulder region of a breast cancer patient (Figure 1.7A) [97]. Further clinical investigations were carried out on PK2, an analogue to PK1, but functionalized with galactosamine to improve the liver targeting ability. ^{123}I-labeled PK1 and PK2 were administered to some hepatocarcinoma patients and their in vivo behavior was compared [97]. Significant liver accumulation of PK2 was present even after 48 h p.i., while little accumulation was observed for PK1 at the same time point. However, the

integrated SPECT/CT images showed that the active targeting conjugate mainly accumulated in healthy liver tissues (17 ± 4% ID) instead of in hepatocarcinoma (3 ± 6% ID). This was explained by the relatively small size of liver tumors as compared to healthy livers and by the fact that hepatocarcinoma was not as well-perfused as healthy liver tissues.

A B

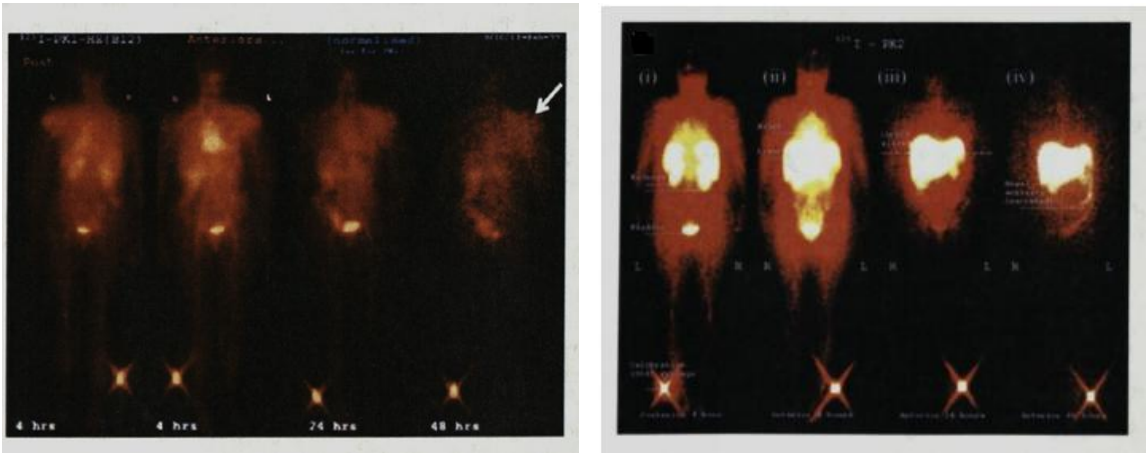

Figure 1.7: A, Gamma scintigraphic imaging of ^{123}I-labeled PK1 in a breast cancer patient with a metastatic lesion in the left shoulder region as indicated by the arrow; B, gamma scintigraphic imaging of 123I-labeled PK2 in four hepatocarcinoma patients. Adapted from Ref [97].

1.4.4 Radiotherapy using HPMA copolymers

The application of radiolabeled HPMA copolymers for tumor-targeted radiotherapy is relatively new and remains to be thoroughly explored. Mitra et al. prepared HPMA-RGD4C conjugates and labeled them with Yttrium-90 (^{90}Y) via the CHX-A''-DTPA chelator side chain [64]. ^{90}Y is a well-known therapeutic radioisotope due to its optimal beta emission (β_{max} 2.27 Mev) properties and the ability to form in vivo stable complexes with DTPA. They evaluated the radiotherapeutic efficacy of these ^{90}Y-labeled HPMA-RGD4C conjugates in a DU-145 tumor xenograft mouse model with a tumor size of around 0.3 cm^3 in volume. Biodistribution studies showed that the tumor accumulation increased significantly ($p<.01$) over time from 1.05 ± 0.03 % ID/g at 1 h to 4.32 ± 0.32% ID/g at 72 h. At the end of the therapeutic study, they observed a 7% and a 63% average decrease in tumor volume for the single dose 100- and 250-μCi ^{90}Y treatment groups, respectively, while the control tumors increased by 442% on average in volume (Figure 1.8). In addition, no acute toxicity was found in the liver and spleen samples from the treatment groups. The study showed that HPMA copolymers are effective carriers to deliver therapeutic doses of radioactivity to inhibit tumor growth. One recent study also showed that the combination treatment of ^{90}Y-labeled HPMA copolymer and PEGylated gold nanorod-mediated hyperthermia could exhibit greater reduction in tumor growth as compared to single treatment alone in a prostate tumor mouse model [98].

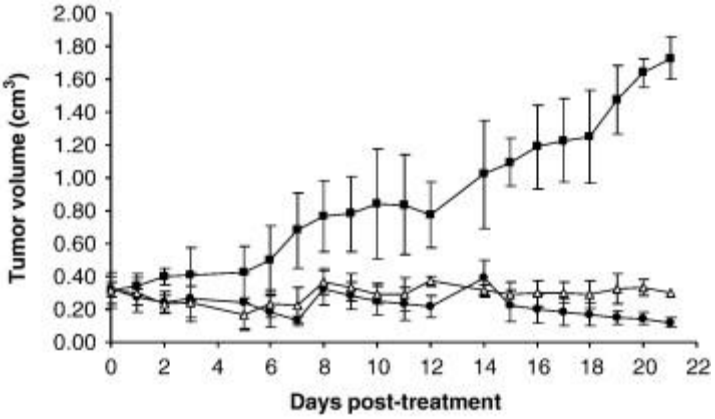

Figure 1.8: Tumor growth of DU-145 xenografts in SCID mice after different treatment: 250 µCi ^{90}Y-labeled HPMA-RGD4C conjugate (closed circle), 100 µCi ^{90}Y-labeled HPMA RGD4C conjugate (open triangle) and untreated control (closed square). Adapted from Ref[64].

1.5 SUMMARY AND CURRENT PROPOSAL

HPMA copolymers are very safe and biocompatible, and can effectively accumulate in tumor sites, which makes them a promising platform for the development of SPECT or PET tracers for pancreatic cancer imaging as well as a good carrier for targeted radiotherapy. However, one major challenge for the development of diagnostic and/or therapeutic HPMA copolymer based agents is their opsonization and sequestration by the MPS. In many cases, the sequestration of these polymers leads to substantial accumulation in the liver and spleen. From a diagnostic perspective, this MPS accumulation in non-target organs can hinder identification of resident or nearby metastatic lesions thereby decreasing the diagnostic efficiency. From the view of therapeutic applications, the non-target accumulation of the polymer drug conjugates can lead to significant toxicities which may be dose-limiting.

Our laboratory is interested in developing synthetic approaches in which HPMA copolymers can be modified to significantly reduce the MPS accumulation or increase the tumor accumulation, thereby enhancing the diagnostic and/or radiotherapeutic efficacy of these agents. Hypotheses to be tested are: 1) the incorporation of metabolic active linkers into HPMA copolymers can lead to lower liver and spleen radioactivity retention; 2) the appropriate optimization of metabolic active linkers and the molecular weight of HPMA copolymers can result in a viable platform for pancreatic tumor imaging; 3) the conjugation of certain targeting ligands (plectin-1 targeted peptide) to HPMA copolymers can enhance the pancreatic tumor accumulation of radiolabeled HPMA copolymers.

Chapter 2

^{177}Lu-Labeled HPMA Copolymers Utilizing Cathepsin B and S Cleavable Linkers: Synthesis, Characterization and Preliminary In Vivo Investigation in a Pancreatic Cancer Model

2.1 INTRODUCTION

Over the last three decades, biomedical researchers have seen the dramatic emergence of polymeric micro- and nanoparticle drug delivery technologies for the treatment of human disease [99-101]. These drug delivery systems include an array of paradigms such as: liposomes, polymer micelles, dendrimers and polymer conjugates. The development of polymeric diagnostic and therapeutic drug delivery systems offer several advantages over traditional drug delivery including the ability to control both the rate and location of drug release. However, one of the main disadvantages of these micro- and nanoparticle based systems has been opsonization and uptake by macrophages (e.g. Kupffer cells) of the mononuclear phagocyte system (MPS) [101, 102]. The hallmark of this MPS uptake is the significant accumulation of the drug delivery system in organs containing MPS cells, specifically the liver and spleen, which can lead to significant toxicity. The development of PEGylation strategies to create "stealth" micro- and nanoparticle systems has contributed to a decrease in MPS accumulation thereby increasing the longevity of the polymeric drug delivery system in the bloodstream [101]. Unfortunately, even with the development of PEGylated techniques, a substantial portion of these polymeric drug delivery systems are still being sequestered by MPS tissues.

N-(2-hydroxypropyl) methacrylamide (HPMA) copolymers have been extensively investigated as a drug delivery vehicle for a variety of chemotherapeutics [100, 103]. While most of the focus on HPMA polymer conjugates has centered on chemotherapeutics, there have been published reports by a variety of investigators regarding the development of diagnostic nuclear imaging and radiotherapeutic agents [67, 84, 96, 104-109]. To date, the majority of these radiolabeled HPMA copolymer conjugates have centered on radioisotopes of iodine (e.g. ^{131}I and ^{123}I). However, recent work by Line, Ghandehari and co-workers, has employed various radiometals (e.g. ^{99m}Tc, ^{111}In and ^{90}Y) common to clinical nuclear medicine [104, 105, 107, 108, 110]. The bulk of the HPMA copolymer conjugates investigated has focused on copolymers that were below the renal excretion threshold (i.e. ~45 kDa) in order to reduce MPS accumulation. While HPMA copolymer conjugates with molecular weights higher than the renal excretion thresholds have demonstrated significantly enhanced tumor delivery, the corresponding substantial increase in MPS tissue retention has largely made this approach undesirable for diagnostics and therapeutic agent development [103].

Cysteine cathepsins are predominantly lysosomal proteases that have been found to have diverse functions, but are primarily attributed to protein catabolism [111]. The function of cathepsin B has mainly been associated with the turnover of both intracellular and extracellular (through endocytosis) proteins in the lysosomal compartment. Tissue expression of cysteine cathepsins has been shown to be variable largely depending on the function of the protease. In some cases such as cathepsin B, the protease is expressed ubiquitously in almost every tissue [100, 112]. However, the highest levels of cathepsin B activity have been found in the liver, spleen, thyroid and kidneys for both murine and humans [113, 114]. For humans the activity of these tissues are 3 -10 fold

higher than other non-target tissues. Conversely, the expression of some cysteine cathepsins, for instance cathepsin S, is selectively expressed in only a small group of cells. Cathepsin S is thought to be an integral protease in the degradation of antigenic proteins as part of the Major Histocompatibility Complex Class II pathway in antigen presenting cells [112, 115]. As a consequence of the critical role of cathepsin S in human immune response, the expression of cathepsin S has been shown to reside primarily in immune cells [116, 117]. Cathepsin B and S are both highly expressed in tissues that are associated with MPS uptake and retention of drug delivery systems.

Protease cleavable linkers are attractive for use in drug delivery due to the typically high serum stability and specificity of the substrate-linkers [118]. In polymer based drug delivery, Kopeček and others have demonstrated the utility of protease cleavable linkers, specifically cathepsin B cleavable linkers, to increase in vivo drug delivery to tumor tissues [100, 103]. However, this technique has also been exploited to decrease retention of radioimmunoconjugates in non-target tissues (e.g. liver) without significantly affecting tumor retention thereby increasing the therapeutic index of the agent [119]. One of the research focuses of our laboratory has been the design of protease cleavable linkers for the development of diagnostic and radiotherapeutic drug delivery systems. The impetus for the development of linkers that are substrates for cathepsin B and S is the high level of expression of these proteases in MPS tissues. The goal of this research is to create metabolically active linkers (MALs) that will increase the efficacy of the diagnostic or radiotherapeutic drug delivery systems by reducing the MPS accumulation. Herein, we describe our initial efforts in the development of MALs using ^{177}Lu-radiolabeled HPMA copolymers as our model system.

2.2 MATERIALS AND METHODS

2.2.1 Solid-Phase Peptide Synthesis

The MAL1 and MAL2 peptides were synthesized on an H-Phe-2-ClTrt and H-Pro-2-ClTrt SPPS resin, respectively, using a microwave peptide synthesizer. The resin (containing 0.25 mmole of peptide anchors) was deprotected using piperidine resulting in the formation of the primary amine. The carboxylic acids of the Fmoc protected amino acids (1 mmol) were activated using COMU and conjugated to the primary amines of the growing peptide on the resin. The process of deprotection, activation and conjugation was repeated until the desired peptide was synthesized. The selective cleavage of the peptide from the 2-chlorotrityl resin anchor was achieved by reaction with 1% TFA in dry DCM and subsequent filtration. The combined crude filtrates were dried by a rotary concentrator. Purification of the peptides was performed using a semi-preparative Proteo C_{12} column with a flow rate of 5.0 mL/min. HPLC solvents consisted of H_2O containing 0.1% formic acid (solvent A) and acetonitrile containing 0.1% formic acid (solvent B). For both peptides, the initial gradient of 70 % A: 30 % B linearly decreased to 60 % A: 40 % B over a 15 minute time period. At the end of the run time for all HPLC experiments, the column was flushed with the gradient 5 % A: 95 % B and re-equilibrated to the starting gradient. The yields after purification were 0.042 mmole, 16.9% (n = 1) for MAL1 and 0.090 mmole, 37.5% (n = 1) for MAL2. Both peptides were determined to be ≥ 95% pure as characterized by LC/MS before in vitro or in vivo use.

2.2.2 Cathepsin Cleavage Assay of MALs

MAL1 and MAL2, 1.51 and 1.22 µmole, respectively, were each weighed and placed into a 1 mL centrifuge tube. Each peptide was dissolved in 100 µl of buffer solution

containing 100 mM sodium acetate, 1 mM EDTA and 5 mM DTT. Solutions of cathepsin B and S were prepared at a concentration of 25 ng/μL. The pH of the solution for dissolution of both the peptide and protease was adjusted to 5.0 and 6.0 for cathepsin B and S assays, correspondingly. In the appropriate tube, 2 and 50 μl of the cathepsin B and S, respectively, were added. The cleavage assay was allowed to proceed for 96 hours at room temperature and was evaluated every 24 hours by LC/MS. Evaluation of the peptides was performed using an analytical Proteo C_{12} column with a flow rate of 1.5 mL/min. HPLC solvents consisted of H_2O containing 0.1% formic acid (solvent A) and acetonitrile containing 0.1% formic acid (solvent B). For both peptides, the initial gradient of 70 % A: 30 % B linearly decreased to 60 % A: 40 % B over a 15 minute time period. At the end of the run time for all HPLC experiments, the column was flushed with the gradient 5 % A: 95 % B and re-equilibrated to the starting gradient. Cleavage estimates were determined by integration of the peptides and metabolite peaks from the total ion chromatogram generated by the LC/MS Waters MassLynx software.

2.2.3 Synthesis and Characterization of the HPMA Copolymer

The HPMA copolymerization was accomplished using the reversible addition-fragmentation chain transfer polymerization reaction with V-501 as the initiator and CTP as the chain transfer agent. The feed ratio of the polymerization consisted of 98.75:0.85:0.40 mole% HPMA, APMA and APMA-FITC, respectively. The polymerization was run at a 1 M total monomer concentration in aqueous acetic buffer (pH = 5.2, 0.27 M acetic acid and 0.73 M sodium acetate) with a molar ratio of total monomer: chain transfer agent: initiator of 2340:3:1. Prior to proceeding with the polymerization reaction, the glass ampule and contents were purged with argon for 20 min. Subsequently, the ampule was flame sealed and allowed to heat at 70 °C in an oil

bath for 14 hours. After cooling the HPMA copolymer was evaporated to dryness, dissolved in methanol and purified by size exclusion chromatography using an LH-20 packing material with methanol as the eluent. The conversion rate was 71% as determined by weight after purification. The weight average molecular weight and polymer dispersity of copolymers were determined by FPLC equipped with UV and RI detectors. The FPLC measurements were carried out on Superose 6 column (HR 10/30) with PBS (pH 7.3) as the eluent. The average molecular weights of the copolymers were estimated using HPMA homopolymer standards with narrow polydispersity indices.

2.2.4 Quantification of the Amine Content in the HPMA Copolymers

Quantitation of the primary amine content of the HPMA copolymer was assessed using a slightly modified ninhydrin assay reported by York and co-workers [120]. A ninhydrin solution was prepared by dissolving 5.61 mmole of ninhydrin in 25 mL ethylene glycol. A $SnCl_2$ solution was made by dissolving 0.177 mmole of $SnCl_2.2H_2O$ in 25 mL of 0.2 M citrate buffer. A ninhydrin-$SnCl_2$ solution, of the desired quantity, was prepared by mixing the two solutions together in a 1:1 volumetric ratio. For the purpose of the creation of a calibration curve, a solution of 3 mM glycine was dissolved in 10 mL DI H_2O and seven standard solutions were prepared by aliquoting amounts from 7.5 – 45 µL of this glycine solution into separate tubes. A 3 mM HPMA copolymer solution was prepared in DI H_2O. For the unmodified HPMA copolymers, MAC0, MAC1 and MAC2 the sample size used were 0.0171, 0.0176, 0.0173 and 0.010 µmole, respectively. For each HPMA copolymer solution, an aliquot of 7.5 µL was added to a sample tube. To both the standard and sample tubes, 200 µL of the ninhydrin-$SnCl_2$ solution was added. The sample and standard solutions were heated to 100 ^oC for 2 h and then allowed to cool to room temperature. The volumes of all solutions were adjusted to 3 mL using DI H_2O and

analyzed by UV spectroscopy at 570 nm. The amine content of the HPMA copolymers was determined based upon the calibration curve generated by the glycine standards. Amine content in the unmodified HPMA copolymers, MAC0, MAC1 and MAC2 was found to be 70.4, 11.5, 19.1 and 11.7 μmol/g of polymer (n = 1 for each copolymer), correspondingly. Conjugation efficiencies were calculated by determination of the difference in the amine content between the MAC and the unmodified HPMA copolymer.

2.2.5 Synthesis of the MACs

The HPMA copolymer (0.292 μmole) was dissolved in 500 μl of DMF. The amine content in 0.292 μmole of HPMA copolymer was 7.04 μmol (1 equiv). In a 10 mL round bottom flask, 20.3 (35.4 μmol, 5.0 equiv), 20.0 (16.2 μmol, 2.3 equiv) or 22.8 mg (16.2 μmol, 2.3 equiv) of MAL0, MAL1 or MAL2 was dissolved in 500 μl of DMF. The solution was cooled to 0 °C and NHS and DCC were added to the flask in the same equivalent amount as the MAL. The solution was stirred at 0 °C for 3 h. At the end of that time, the HPMA copolymer was added and stirred for another 2 h at 0 °C. Subsequently, the reaction was allowed to warm to room temperature and continued for an additional 18 hours. The precipitate generated from the reaction was filtered off and the filtrate was evaporated to dryness. The residue was dissolved in methanol followed by size exclusion chromatography using an LH-20 packing material. Evaporation of the high molecular weight fraction afforded light yellow HPMA copolymer-peptide conjugates. Based on the determined conjugation efficiencies from the ninhydrin assays, the percent recovery (n =1) of MAC0 was 77.6 (0.233 μmole), MAC1: 45.3 (0.140 μmole) and MAC2: 50.0% (0.157 μmole).

Deprotection of the orthogonal protecting groups was accomplished using standard peptide cleavage conditions. Briefly, to a 0.0875 µmole sample of the MAC0, MAC1 and MAC2 was added 4 mL of a cleavage cocktail at 0 °C consisting of a 1:1:1:37 volumetric ratio of DODT, water, TIS and TFA. For the MAC2, the cleavage cocktail used was a 1:1:1:0.75:46.25 volumetric ratios of DODT, water, TIS, thioanisole, and TFA. Initially, the solution was stirred for 15 min at 0 °C. Subsequently, the cleavage reaction was allowed to warm up to room temperature and was continued for an additional 3 h. At the end of that time, the solution was evaporated and the residue dissolved in methanol followed by size exclusion chromatography using LH-20 packing material with methanol as the eluent. The collected high molecular weight fractions were evaporated to dryness to afford the deprotected copolymer-peptide conjugates. Based on the determined conjugation efficiencies, the percent recoveries (n = 1) of MAC0, MAC1 and MAC2 were 80.2 (0.0697 µmole), 100 (0.0863 µmole) and 93.4 % (0.0808 µmole), respectively.

2.2.6 Radiolabeling of the HPMA Copolymers

The radiolabeling of the MACs was accomplished by heating the copolymer at 90 °C for 1 h in the presence of 74 MBq (2mCi) of $^{177}LuCl_3$. After cooling the resulting ^{177}Lu-radiolabeled MACs were purified by radio-SEC-HPLC. Isolation of the ^{177}Lu-MACs was accomplished using an isocratic mobile phase consisting of PBS with 0.02 mM EDTA at pH 7.4. The linear flow rate was 0.80 mL/min. UV analysis was performed at a wavelength of 494 nm. After collection of the peak-purified ^{177}Lu-radiolabeled MACs, 0.113 mmole of L-ascorbic acid was added as a radiolysis inhibitor. The purified ^{177}Lu-radioconjugate was concentrated using an Amicon Ultra-4 Centrifugal Filter and washed with 5 mL of deionized water. The purified ^{177}Lu-radiconjugates were diluted with sterile saline to 0.37 MBq (10 µCi) per 100 µL. The radiochemical purity of all radioconjugates

was re-evaluated before administration and found to be ≥ 95 % pure as determined by the radio-HPLC.

2.2.7 Cathepsin Cleavage Assay of Radiolabeled Copolymers

Briefly, 0.291 nmole of each purified ^{177}Lu-radiolabeled MACs (90~120 µCi) was incubated in a buffer with the indicated cathepsin in Eppendorf tubes at 25 ºC. The buffer solution consisted of 50 mM sodium acetate, 1 mM EDTA and 5 mM DTT, and pH was adjusted 5.0 for cathepsin B and 6.0 for cathepsin S to maximize the enzyme activity. For the MAC0, the copolymer was incubated in the presence of either cathepsin B (5 ng/µl) or cathepsin S (10 ng/µl) in 400 µl of buffer solution. MAC1 and MAC2 were incubated with cathepsin B (5 ng/µl) and cathepsin S (10 ng/µl), respectively, in 400 µl buffer. After every 24 hours, a 100 µl aliquot of the copolymer solution was analyzed by radio-SEC-HPLC to determine the relative amount of cathepsin cleavage product. The analysis utilized an isocratic gradient with a mobile phase consisting of PBS with 0.02 mM EDTA at pH 7.4. The radio-SEC-HPLC analysis was carried out utilizing a linear flow rate of 0.80 ml/min and a UV wavelength of 494 nm.

2.2.8 Human Serum Stability of Radiolabeled Copolymers

Briefly, 0.291 nmole of purified ^{177}Lu-MAC0, ^{177}Lu- MAC1 and ^{177}Lu-MAC2 was incubated with 1 mL of human AB serum at 37 °C. After 72 h, the stability was determined by centrifuge filtration using an Amicon Ultra Ultracel 10 kDa filter. A 100µl aliquot was loaded in the filter and diluted with 4 mL DI water, centrifuged and washed with an additional 4 mL DI water. The percent stability of ^{177}Lu-radiolabeled copolymers

was calculated based on the radioactivity of the copolymers remaining in the 10 kDa filter and the total radioactivity added.

2.2.9 Macrophage Differentiation and Cell Culture

Human monocytes were harvested from normal donors in the UNMC Elutriation Core Facility. Upon receipt, monocytes were immediately plated into T75 tissue culture flasks at a concentration of 20 $x10^6$ cells in 20 mL of macrophage differentiation medium DMEM containing 10% FBS, 1% Penicillin/Streptomycin, 2 mM l-glutamine, 1% sodium-pyruvate, 1% NEAA and 500 U rhM-CSF. Media was half-exchanged every 2 to 3 days for 7-10 days, at which time, visual confirmation of differentiation was made and media was changed to macrophage maintenance medium (differentiation medium without the rhM-CSF). Cells were maintained at 37 °C at 5% CO_2 in air.

The HPAC cells were cultured in our laboratory, as per ATCC protocols, in a 1:1 mixture of DMEM and Ham's F12 medium containing 14.3 mM sodium bicarbonate, 2.5 mM L-glutamine, 15 mM HEPES and 0.5 mM sodium pyruvate supplemented with 0.350 µM insulin, 0.0625 µM transferrin, 0.110 µM hydrocortisone, 1.562 nM epidermal growth factor and 5% FBS. Cells were incubated at 37 °C at 5% CO_2 in air.

2.2.10 Cathepsin B and S Activity Assays

The cathepsin B and S activity in macrophage and HPAC cell lines was determined using a commercial cathepsin B and S activity assay kit. The method is simplified as follows: 2 million macrophage and HPAC cells each were subjected to 500 µl cell lysis buffer. After 10-min incubation on ice, the cell lysate was centrifuged at 3000 rpm for 5

min. For each individual assay, 50 µl of the supernatant was transferred to a 96-well plate to which 50 µl of reaction buffer and 2 µl of either cathepsin B or S substrate was added. For the control group, another 2 µl of cathepsin B or S inhibitor was added. The reaction was allowed to proceed at 37 °C for one hour. Samples were read using a fluorometer with a 400-nm excitation filter and a 505-nm emission filter. Activities correlating with the specified cathepsin protease were determined by subtraction of the RFU measurements of the samples with and without inhibitor. Each individual assay was replicated 10 times.

2.2.11 Internalization Study of MACs by Flow Cytometry

Macrophage and HPAC cells were seeded in 6-well plates at a density of 5×10^5 cells per well and incubated in media overnight (37 °C, 5% CO_2). Cells were then incubated with three MACs (0.1 mg/mL) at 37 °C for the indicated time periods. After incubation, the media was removed. Cells were harvested and washed with PBS three times followed immediately by flow cytometry analysis. Each sample analysis involved the evaluation of 1.0×10^4 cells. The collected data was averaged and reported as the mean fluorescent intensity for each sample.

2.2.12 Biodistribution Studies

Biodistribution studies were carried out using SCID mice with HPAC xenografts. The inoculation media was prepared using a 1:1 volumetric ratio of suspended HPAC cells to Matrigel™ to obtain a final concentration of 2×10^6 HPAC cells per 100 µl. The mice received a 100 µl subcutaneous inoculation into each flank. Upon achieving sufficient tumor size, (10-20 mm in diameter) the mice were considered viable for biodistribution

studies. The mice (average weight, 25g) were injected with a 0.37 MBq (10 μCi) intravenous bolus of the purified ^{177}Lu-MAC. The mice were sacrificed and their tissues excised at 24, 48 and 72 h time points post-injection. The excised tissues were weighed and the ^{177}Lu activity measured in each tissue using a gamma counter. Aliquots of the injected dose were counted as a reference standard for the calculation of % ID/g values.

2.2.13 Statistical Analysis

Data is presented as mean ± SEM. Evaluation of significance between the three groups of data was accomplished using a non-parametric Kruskal Wallis test. If the overall *p*-value from the Kruskal Wallis test was < 0.05, pairwise comparisons were made between the three groups using a non-parametric Mann Whitney test. In all cases, the reported *p*-values are adjusted and an adjusted *p*-value ≤ 0.10 was considered statistically significant.

2.3 RESULTS

2.3.1 Design and Synthesis of the Metabolically Active Linkers (MALs)

The MALs used in synthesis of the metabolically active copolymers (MACs) are depicted in Figure 2.1. For MAL1 and MAL2, the peptide sequences are composed of three parts: the radiometal chelation system, the clearance sequence, and the metabolic sequence. Both MAL1 and MAL2 contain the same chelation system (DO3A) and clearance sequence (G-(D)S(tBu)-(D)S(tBu)), but differ in the metabolic sequence. For MAL1 the metabolic sequence (G-G-G-F) is a known substrate for the cathepsin B protease whereas the metabolic sequence for MAL2 (P-M-G-L-P) is a known substrate for cathepsin S [121, 122]. In the studies described herein, MAL0 is simply the DO3A

chelation system and is the control for our experiments. The MAL0 contains no amino acids and would not be expected to undergo any proteolytic degradation. All of the MALs were prepared with intact orthogonal protecting groups in order to carry out subsequent conjugation reactions with the HPMA copolymer. The synthesis of MAL1 and MAL2 was accomplished using SPPS. Detachment of the protected MALs from the resin support was accomplished with dilute acid (1% TFA) using 2-chlorotrityl anchor chemistry. The crude MALs were isolated and peak purified (n = 1) yielding 16.9% for MAL1 and 37.5 % for MAL2 of isolated, purified material (based on a 0.25 mmol scale synthesis). The RP-HPLC retention times and the mass spectrometric characterization of the MALs are depicted in Table 2.1.

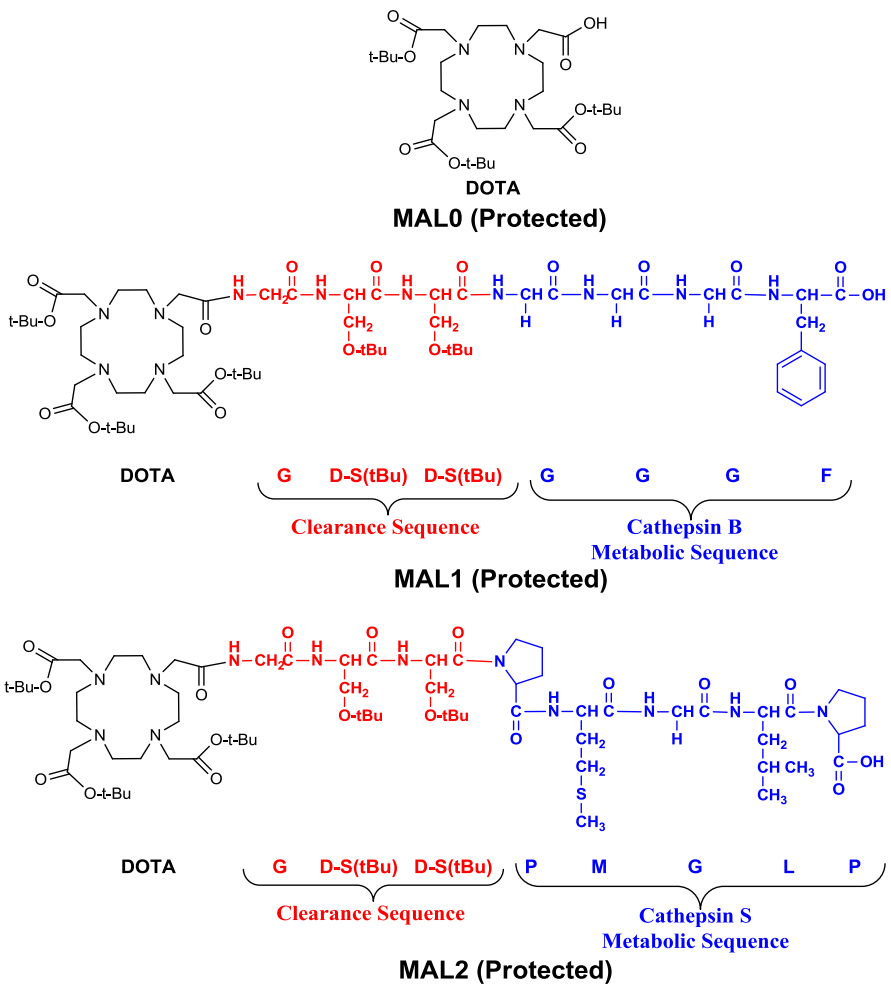

Figure 2.1: Schematic of the design of MALs.

Table 2.1: MALs characterization

MAL Peptide	Sequence	Formula	R_t (min) RP-HPLC	Mass Expected $[M+H]^+$	Mass Observed $[M+H]^+$
MAL0	$DOTA(tBu)_3$	$C_{28}H_{52}N_4O_8$	--	573.4	573.2
MAL1	$DO3A(tBu)_3$-G-(D)S(tBu)-(D)S(tBu)-G-G-G-F	$C_{59}H_{99}N_{11}O_{17}$	6.5	1234.7	1234.5
MAL2	$DO3A(tBu)_3$-G-(D)S(tBu)-(D)S(tBu)-P-M-G-L-P	$C_{67}H_{118}N_{12}O_{18}S$	9.8	1411.8	1411.5

2.3.2 In Vitro Metabolism of MALs

In order to confirm that the MAL1 and MAL2 will undergo proteolytic cleavage, the un-metalated, protected MALs were incubated in the presence of the appropriate cathepsin protease. LC/MS analyses (n = 1) of the metabolism of MAL1 and MAL2 by cathepsin B and S, correspondingly, are displayed in Figure 2.2. Under the gradient conditions employed, the MAL1 and MAL2 peptides exhibited retention times of 5.7 and 8.9 min, respectively. For MAL1 a significant metabolite peak was observed at a retention time of 4.3 min. At 24 and 48 h post incubation, LC/MS analyses revealed that 56 and 78 %, respectively, of the original MAL1 peptide had been metabolized. Evaluation of the MAL1 metabolite mass (1030.5 Da) corresponds to the site of proteolytic cleavage being between the first and second glycine residues from the C-terminus (GG┼GF). With respect to the MAL2 peptide, a metabolite was observed with a retention time of 7.0 min. Over the course of the study, the amount of MAL2 peptide metabolized increased from 11 to 80 %. The mass of the metabolite corresponded with the cleavage site being located between the glycine and leucine residues (DO3A-G-(D)S-(D)S-P-M-G┼L-P). Overall, these studies demonstrate that both MAL1 and MAL2 are proteolytically active and that the rate of metabolism of MAL2 by cathepsin S was slower relative to the cathepsin B cleavage of MAL1.

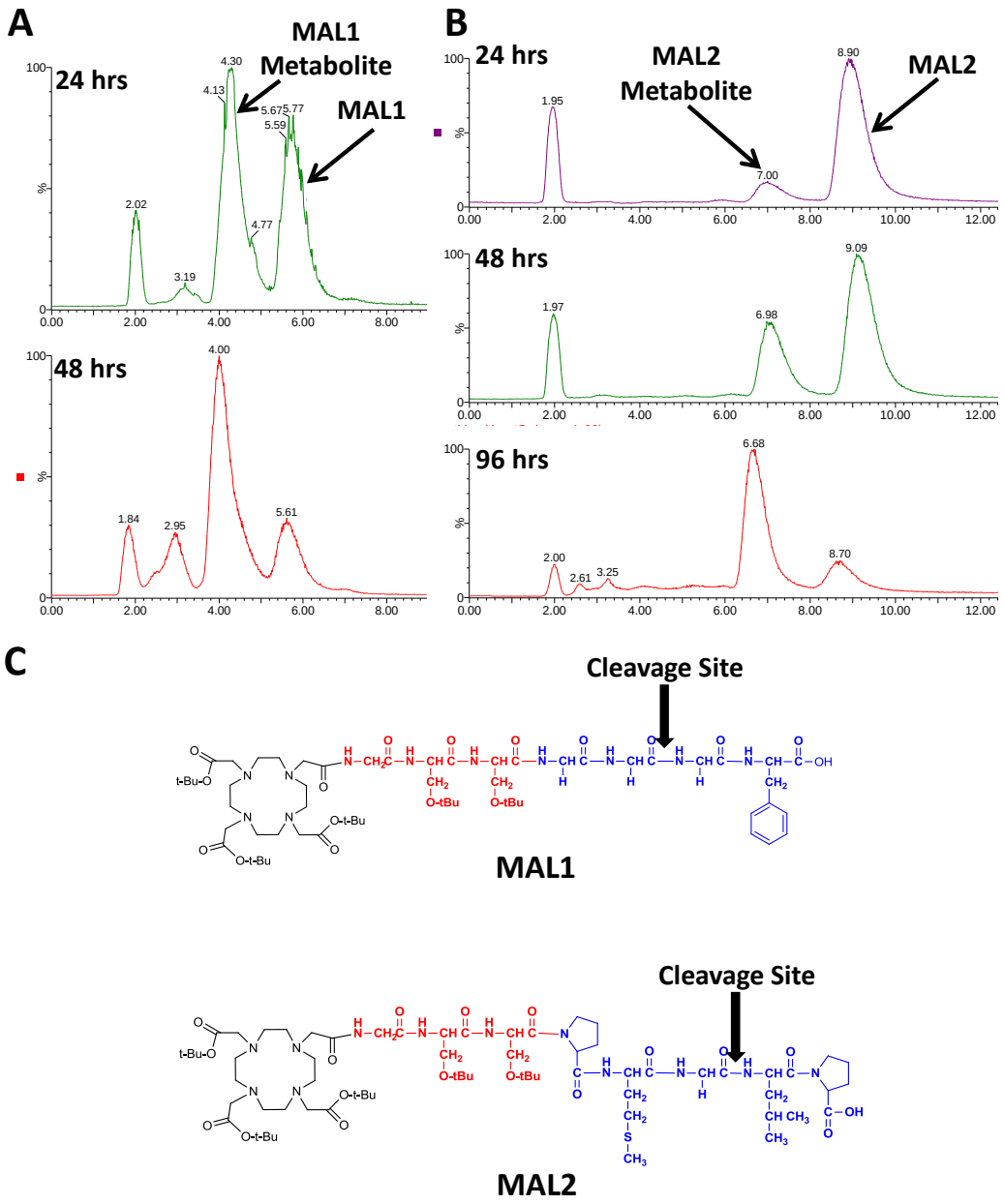

Figure 2.2: Evaluation of cathepsin B and S cleavage of MAL1 and MAL2, correspondingly. A, Total ion chromatograms of the cleavage of MAL1 by cathepsin B at 24 and 48 h post-incubation B, Total ion chromatograms of the cleavage of MAL2 by cathepsin S at 24, 48 and 72 h post-incubation C, Depicts the enzymatic cleavage sites of MAL1 and MAL2.

2.2.3 Design and Synthesis of the Metabolically Active Copolymers

The scheme for the synthesis of the MACs is depicted in Figure 2.3. The HPMA copolymer consisted of HPMA, APMA and APMA-FITC monomers which were polymerized, using reversible addition-fragmentation chain transfer (RAFT) polymerization, with a feed composition of 98.75:0.85:0.40, respectively. Assessment of the synthesized HPMA copolymer by FPLC revealed a molecular weight of 343 kDa with a polydispersity of 1.6. Evaluation by quantitative ninhydrin analysis revealed that 121% of the APMA monomer was incorporated into the HPMA copolymer which yielded a total amine content of 70.4 µmol/g (n = 1) of polymer.

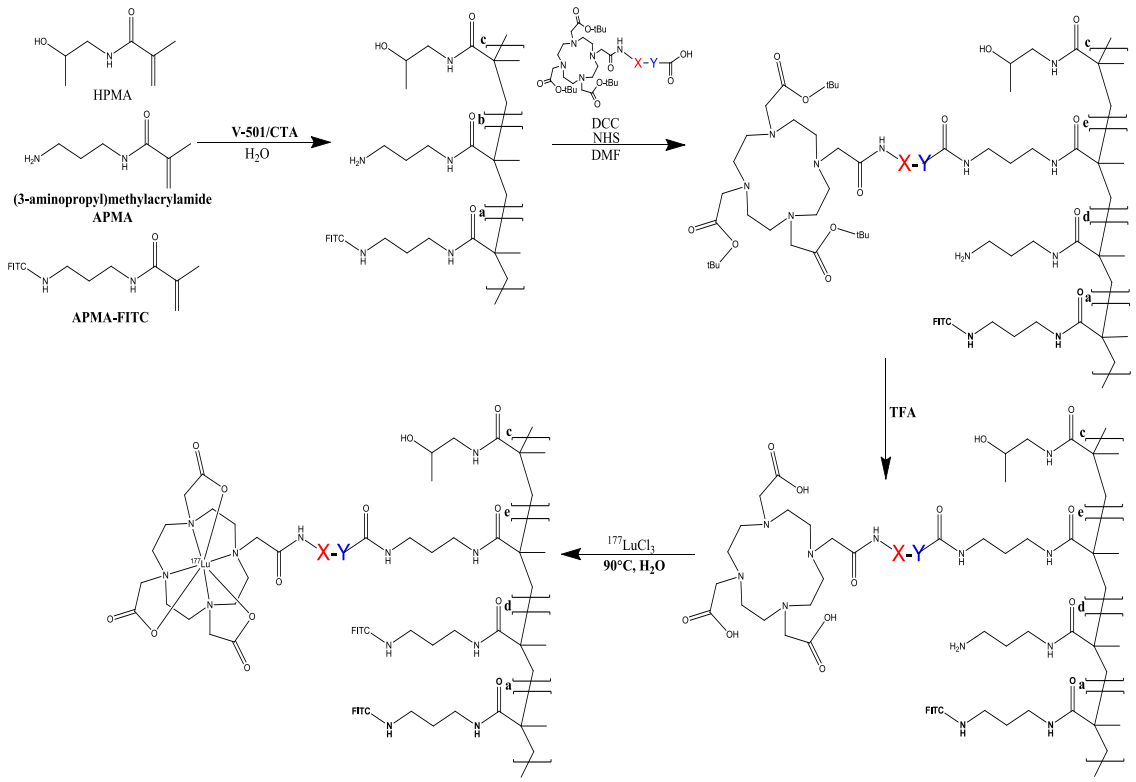

Figure 2.3: Synthetic scheme for the synthesis of the ^{177}Lu-MAC conjugates. For MAC0, MAC1, MAC2, X = Y = null, X = GSS, Y = GGGF and X = GSS, Y = PMGLP respectively.

Conjugation of the MALs to the HPMA copolymer was accomplished using standard coupling chemistry. The preparation of protected peptides allowed for chemo-selective coupling of the C-terminal carboxylic acid with the aliphatic amine of the HPMA copolymer. Once the MALs were conjugated to the HPMA copolymer, the HPMA copolymers were termed MAC0, MAC1 and MAC2 corresponding to the conjugated MAL. Deprotection of the peptide components of the MACs were carried out using a standard cleavage cocktail containing predominantly trifluoroacetic acid. The deprotection of the MACs was verified by evaluation of MAC0 before and after deprotection using NMR (supporting information). The signal for the t-butyl groups of the DO3A was eliminated after the deprotection reaction corresponding to the loss of the t-butyl groups. With this information in hand, the cleavage conditions used for MAC0 were determined to be sufficient for the deprotection of MAC1 and MAC2. After deprotection the coupling yield of the MACs were analyzed by quantitative ninhydrin analyses. Ninhydrin analysis gave an 83.6, 72.9 and 83.4 % coupling efficiency (n = 1) for MAC0, MAC1 and MAC2, respectively.

2.3.4 Synthesis, Cathepsin Cleavage and Serum Stability of ^{177}Lu-labeled-MACs

The ^{177}Lu-radiolabeled MACs were prepared using relatively mild conditions. Incubation of the MACs with $^{177}LuCl_3$ for 1 h at 90 °C gave relatively moderate to good radiochemical yields of 60 - 85 % (n = 3). Radiolabeled yields were found to be dependent, to some extent, on the HPMA copolymer concentration. A more thorough investigation of the parameters that influence the radiolabeling efficiency of MACs is on-going. The ability of the synthesized ^{177}Lu-MACs to undergo Cathepsin B and S cleavage was investigated over a 72 h period, Figure 2.4. During the course of the investigation, the non-cleavable control (^{177}Lu-MAC0) was found to be stable in the

presence of Cathepsin B and S with negligible cleavage as determined by radio-SEC-HPLC. However, ^{177}Lu-MAC1 and ^{177}Lu-MAC2 demonstrated significant cleavage as shown by the generation of the low-molecular weight radiometabolite after 72 h of incubation. The percentage of the generated radiometabolite was 8 and 26 % (n = 1) for ^{177}Lu-MAC1 and ^{177}Lu-MAC2, respectively. The stability of the ^{177}Lu-labeled-MACs in human serum was investigated by incubation at 37 °C for a 72 h period. Over the course of the study, the percentage of intact ^{177}Lu-labeled-MACs remained greater than 98%.

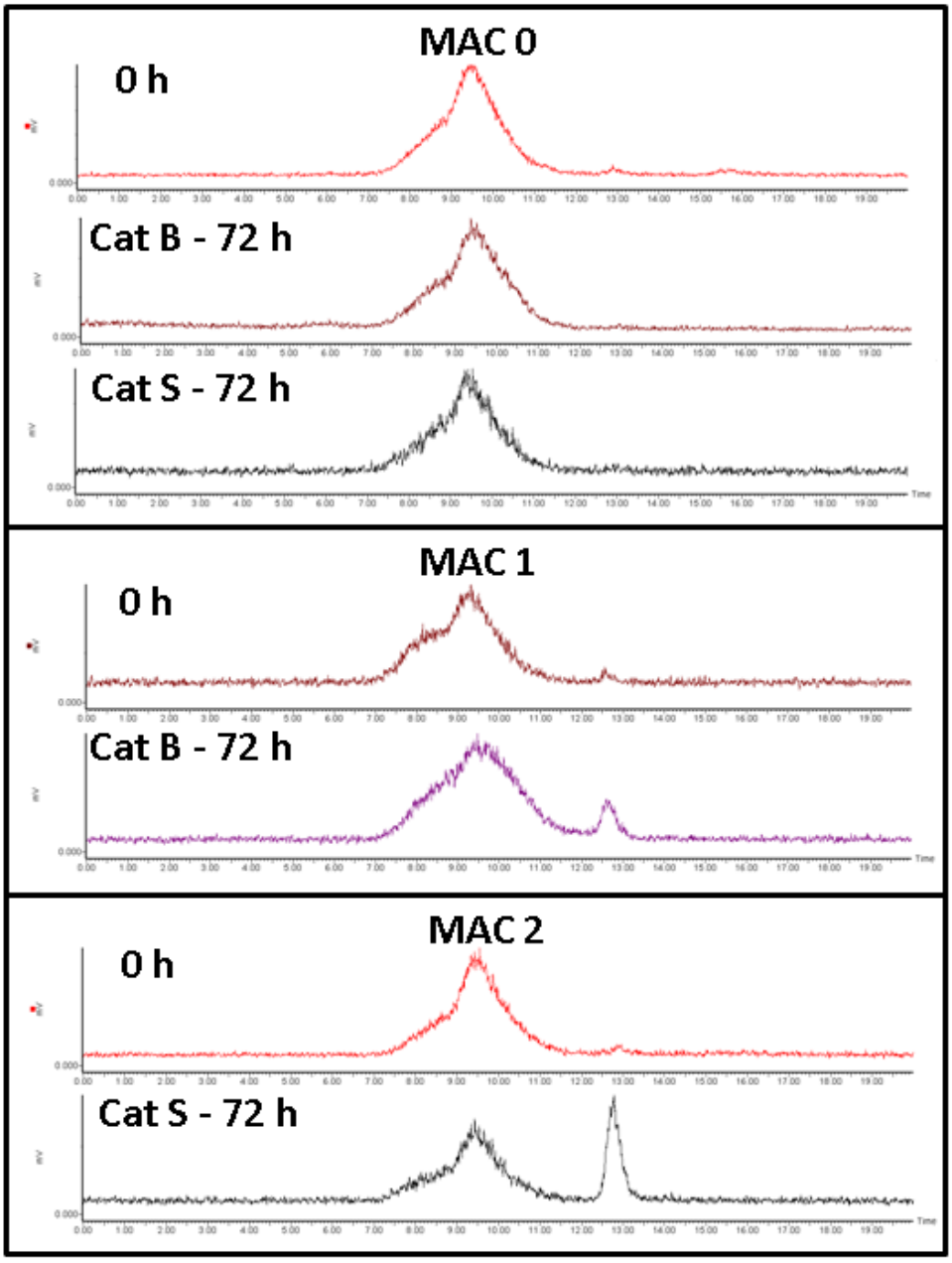

Figure 2.4: Cathepsin B and S cleavage of ^{177}Lu-MAC0, ^{177}Lu-MAC1 and ^{177}Lu-MAC2 as determined by radio-SEC-HPLC at 72 h post-incubation.

2.3.5 Cathepsin Activity and MAC Uptake in Macrophage and HPAC Cell Lines

In the investigation of the in vitro properties of the MACs, differentiated human macrophage and HPAC cancer cell lines were used as in vitro models of the MPS and pancreatic cancer. The cathepsin B and S activity in both of these cell lines were investigated by fluorometric analysis, depicted in Figure 2.5. In a cell to cell comparison, the differentiated macrophage demonstrated substantially higher activities of both cathepsin proteases relative to the HPAC cell line. The protease activity in the macrophage was 70 and 10 fold higher for cathepsin B and S, respectively, relative to the HPAC cell line.

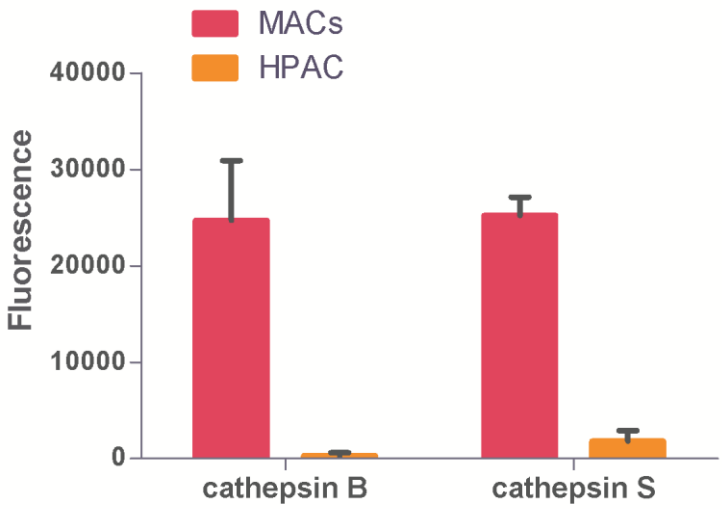

Figure 2.5: Evaluation of cathepsin B and S activity between macrophage and HPAC cell lines. Data is presented as mean ± S.D. from n=10 experiments.

The cellular uptake of the MACs in differentiated macrophage and the HPAC cell line was investigated. Utilizing flow cytometry analysis, the relative uptake of the MACs in terms of mean fluorescence units is depicted in Figure 2.6. Over the 48 h incubation time, all of the MACs investigated demonstrated steady increase in macrophage uptake. In comparison, the HPAC cell line revealed little uptake of the MACs over the time period studied.

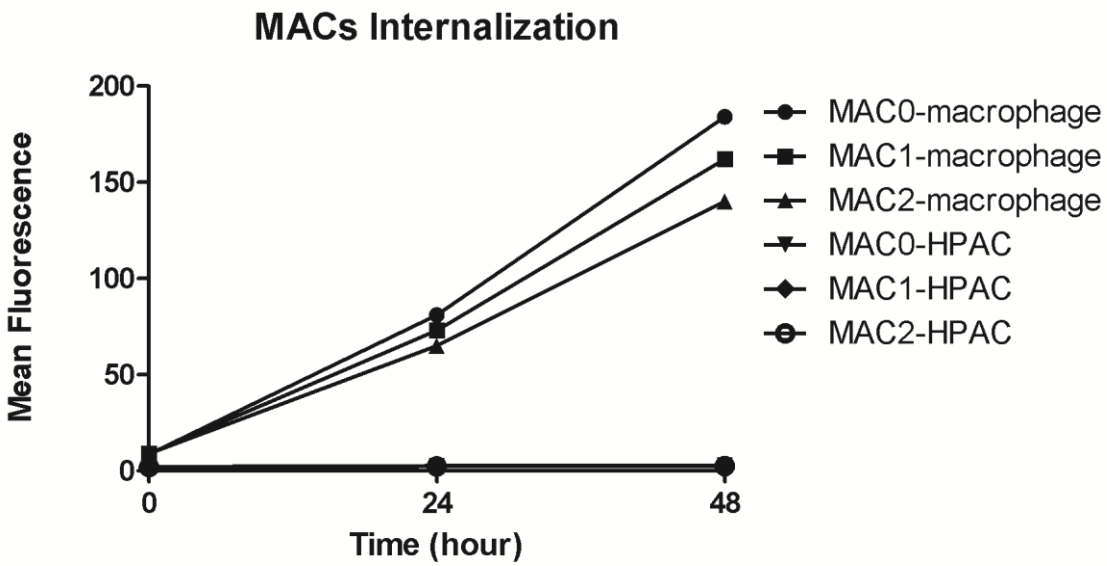

Figure 2.6: Mean fluorescence of MAC0, MAC1 and MAC2 after 0 h, 24 h and 48 h incubation in macrophages and HPAC cells measured by flow cytometry.

2.3.6 Biodistribution Studies of ^{177}Lu labeled MACs in HPAC Xenograft SCID Mice

A preliminary investigation of the in vivo tumor targeting and clearance properties of the MACs was performed in a SCID mouse model bearing HPAC tumor xenografts. The results of the biodistribution studies of the three ^{177}Lu-MACs at 24 and 72 h post-injection are given in Table 2.2. At 24 h post-injection, the blood retention of the ^{177}Lu-MAC1 and ^{177}Lu-MAC2 was, on average, lower than the control (^{177}Lu-MAC0). All of ^{177}Lu-MACs demonstrated a 2 fold decrease in blood retention by the 72 h p.i. time point. At 24 h post-injection, the liver accumulation of the ^{177}Lu-MAC1 and ^{177}Lu-MAC2 was 3.44 ± 0.82 and 5.29 ± 0.98 %ID/g, correspondingly, which was lower than the 7.27 ± 2.64 %ID/g of ^{177}Lu-MAC0 (p = 0.34). The liver retention of the ^{177}Lu-MAC0 increased to a final accumulation of 11.36 ± 1.65 %ID/g at 72 h post-injection. Conversely, the liver retention of the MACs that utilize cleavable peptides, ^{177}Lu-MAC1 and ^{177}Lu-MAC2, remain statistically the same with 3.61 ± 0.63 and 5.46 ± 0.44 %ID/g, respectively, at the 72 h time-point. At the 24 h time-point, the spleen retention of ^{177}Lu-MAC1 and ^{177}Lu-MAC2 were lower on average than the ^{177}Lu-MAC0. However, by the 72 h time-point, the ^{177}Lu-MAC0 demonstrated a substantial increase in spleen retention of 21.46 ± 4.41 %ID/g. In comparison, ^{177}Lu-MAC1 and ^{177}Lu-MAC2 exhibited a significantly lower retention of 5.63 ± 1.22 (p = 0.06) and 5.67 ± 0.75 %ID/g (p = 0.03), respectively, which corresponds to a substantial 4 fold reduction in spleen accumulation at the analogous time point. With regards to tumor retention, the control exhibited higher accumulation at all time-points investigated. At the 24h time point, the tumor uptake of 1.18 ± 0.25 and 1.64 ± 0.18 %ID/g ^{177}Lu-MAC1 and ^{177}Lu-MAC2 was substantially lower than the 4.09 ± 1.41 %ID/g of the ^{177}Lu-MAC0 (p = 0.16). By 72 h post-injection, the ^{177}Lu-MAC0 tumor accumulation increased by 61% to 6.58 ± 0.93. For ^{177}Lu-MAC1 and ^{177}Lu-MAC2, the

tumor retention increased to 2.33 ± 0.30 and 3.49 ± 0.28 %ID/g, representing an increase of 125 and 113%, correspondingly, at the 72 h time-point.

Table 2.2: Biodistribution studies of ^{177}Lu-MAC0, ^{177}Lu-MAC1 and ^{177}Lu-MAC2 at 24 and 72 h post-injection in HPAC tumor-bearing SCID mice. Data is represented as %ID/g.

	24 hours			72 hours		
Tissues	**Lu-MAC0[b]**	**Lu-MAC1[a]**	**Lu-MAC2[c]**	**Lu-MAC0 [b]**	**Lu-MAC1[b]**	**Lu-MAC2[c]**
Blood	28.50 ± 6.59	14.85 ± 1.23	17.76 ± 1.57	13.40 ± 1.71	8.54 ± 1.76	8.89 ± 0.65
Bladder	9.09 ± 3.49	1.63 ± 0.94	3.11 ± 0.82	7.15 ± 2.61	2.18 ± 0.25	3.61 ± 0.34
Small Int.	1.36 ± 0.42	0.85 ± 0.15	0.97 ± 0.12	1.25 ± 0.21	0.51 ± 0.09	0.67 ± 0.06
Large Int.	1.48 ± 0.38	0.84 ± 0.09	1.31 ± 0.17	1.25 ± 0.21	0.54 ± 0.09	1.06 ± 0.15
Stomach	1.02 ± 0.21	0.63 ± 0.07	0.80 ± 0.10	0.91 ± 0.14	0.37 ± 0.07	0.52 ± 0.04
Pancreas	2.16 ± 0.66	0.93 ± 0.22	1.35 ± 0.25	2.95 ± 0.55	1.10 ± 0.20	1.10 ± 0.13
Spleen	7.83 ± 3.32	5.09 ± 1.24	4.95 ± 0.49	21.46 ± 4.41	5.63 ± 1.22	5.67 ± 0.75
Kidney	5.22 ± 1.57	2.50 ± 0.59	3.34 ± 0.44	4.20 ± 0.58	1.93 ± 0.38	2.51 ± 0.17
Tumor	4.09 ± 1.41	1.18 ± 0.25	1.64 ± 0.18	6.58 ± 0.93	2.33 ± 0.30	3.49 ± 0.28
Liver	7.27 ± 2.64	3.44 ± 0.82	5.29 ± 0.98	11.36 ± 1.65	3.61 ± 0.63	5.46 ± 0.44
Lung	8.18 ± 2.60	3.81 ± 0.76	4.16 ± 0.37	5.56 ± 1.01	2.66 ± 0.46	3.56 ± 0.16
Heart	6.13 ± 1.75	2.37 ± 0.50	2.72 ± 0.30	5.00 ± 0.75	1.85 ± 0.38	2.26 ± 0.22
Brain	0.91 ± 0.23	0.30 ± 0.10	0.36 ± 0.04	0.57 ± 0.00	0.24 ± 0.05	0.27 ± 0.02
Bone	1.71 ± 0.51	0.85 ± 0.09	1.20 ± 0.16	3.06 ± 0.46	0.68 ± 0.12	1.02 ± 0.11
Muscle	1.36 ± 0.42	0.71 ± 0.13	0.75 ± 0.08	2.38 ± 0.55	1.37 ± 0.39	1.46 ± 0.15

The data is given in mean ± SEM. [a]N = 4, [b]N = 5, [c]N = 6.

2.4 DISCUSSION

For cancer diagnostics and therapeutics based on biopolymers such as HPMA copolymers, it is well known that increases in the molecular weight of the carrier typically results in an improvement in the enhanced permeability and retention (EPR) effect [103, 123, 124]. As a result of the increase in the EPR effect of the carrier, the drug delivery system will typically demonstrate an increased localization and retention in cancerous tissues. Conversely, an increase in the molecular weight of a biopolymer by and large causes a substantial increase in the MPS accumulation, particularly if the molecular weight of the carrier is above the renal excretion threshold. The MPS accumulation of HPMA copolymers, and other nanomedicine platforms, is a major hurdle in the development of more efficacious biopolymer systems and the translation of these systems to the clinic [125, 126].

Our approach to this challenge is to develop MALs that preferentially hydrolyze in MPS cells in order to reduce the retention, and thus radiotoxicity, in non-target tissues. In our design peptide substrates of cathepsin B and S were chosen due to the high level of expression of these proteases in MPS tissues. As depicted in Figure 3, the MAL design is composed of three components: radiometal chelation system, metabolic sequence and clearance sequence. The DO3A chelation system was chosen because it has been shown to stabilize a variety of radiometals, including ^{177}Lu, in preclinical and clinical investigations [127, 128]. The metabolic sequences are composed of known peptide substrates for the cathepsin B and S enzymes [121, 122]. It is expected that alterations of the metabolic sequence can be used to influence the rate of enzymatic cleavage and thus affect clearance of the radiometabolites from the tissues. While the chosen amino acid sequences have demonstrated selectivity for the corresponding

protease relative to other lysosomal proteases, it is important to keep in mind that other proteases may contribute to the metabolism of these sequences in vivo. In order to better control the pharmacokinetics of the radiometabolite after cleavage, D-amino acids were employed in the design of the clearance sequence, G-D(S)-D(S), to prevent, or at least significantly reduce, metabolism. By preventing metabolism the pharmacokinetic properties of the generated radiometabolite can be better controlled to influence diffusion and thus biological clearance [129].

The MALs were prepared with intact orthogonal protecting groups using standard SPPS techniques. Synthesis of the protected MALs was necessary for later chemoselective conjugation to the HPMA copolymers. Both MAL1 and MAL2, protecting groups intact, underwent incubation in the presence of the appropriate cathepsin protease. Over the course of the metabolism study, both of the MALs demonstrated conversion into a single metabolite. Both of these cleavage sites are in accordance with previous literature reports [121, 130]. From these initial investigations, the enzyme kinetics for cathepsin B for MAL1 appears to be significantly faster as compared to cathepsin S for MAL2.

Synthesis of the HPMA copolymer backbone was accomplished using the RAFT polymerization technique. The synthesized HPMA copolymer (M_w = 343 kDa, PDI = 1.6) is well above the renal threshold of 45 kDa. Conjugation of the MALs to the terminal amine of the APMA copolymer constituent was accomplished in fairly high yield as determine by ninhydrin assay. In order to ensure chemo-selectivity, MALs were prepared with intact orthogonal protection groups. The protecting groups prevented functional groups other than the desired C-terminal carboxylic acid from conjugating to the primary

amine on the HPMA copolymer. Deprotection of the MACs was accomplished, as confirmed by NMR, in 3 hours using a standard SPPS cleavage cocktail. Radiolabeling of the MACs with ^{177}Lu was achieved in good yield using standard radiolabeling conditions. Incubation of ^{177}Lu-MAC1 and ^{177}Lu-MAC2 in the presence of Cathepsin B and S, respectively, demonstrated, as expected, that a low-molecular weight radiometabolite is generated. Exposure of ^{177}Lu-MAC0 (non-cleavable control) to either of the investigated cathepsin did not show any signs of radiometabolite generation. This data shows that the generation of the radiometabolite is a proteolytic process. In additional, this data confirms that the MAL can still be cleaved despite being attached to the HPMA copolymer support. Serum stability studies of the ^{177}Lu-MACs revealed essentially no degradation (> 98% intact) suggesting that the ^{177}Lu-MACs would not susceptible to extracellular blood proteases in vivo.

In our investigations of the in vitro properties of the MACs, we modeled the phagocytic cells of the MPS and pancreatic cancer cells utilizing differentiated human macrophage and the HPAC pancreatic cancer cell line, correspondingly. Evaluation of the cathepsin B and S activity of these cell lines revealed that both cathepsin B and S activity is substantially higher, 70 and 10 fold respectively, in the macrophages relative to the HPAC cell line. Additionally, analysis of the internalization rate of the MACs in these two cell lines demonstrated that macrophages undergo steady uptake of the MACs over the course of the study, while relatively little uptake was exhibited by the HPAC cancer cell line. These data imply that the in vivo uptake and metabolism of the MACs should be strongly favored in MPS cells relative to the pancreatic cancer cells. Given this, we would expect enhanced clearance from tissues containing MPS components (i.e., liver and spleen) in vivo.

Our initial investigation into the in vivo characteristics of the ^{177}Lu-MACs was undertaken in an HPAC xenograft mouse model. All of the ^{177}Lu-MACs investigated demonstrated extended blood circulation due to the molecular weight of the HPMA copolymer being substantially higher than the renal excretion threshold [131]. Interestingly, the blood retention of ^{177}Lu-MAC1 and ^{177}Lu-MAC2 demonstrate similar longevity in the blood pool and is approximately half of the value of the ^{177}Lu-MAC0 at all reported time points. The reduced blood retention of the ^{177}Lu-MAC1 and ^{177}Lu-MAC2 relative to the control (^{177}Lu-MAC0) strongly suggest that the HPMA copolymers with MALs underwent proteolytic cleavage in the blood. However, the in vitro serum stability studies of the ^{177}Lu-MAC1 and ^{177}Lu-MAC2 revealed no significant proteolysis. These data imply that the cleavage of the ^{177}Lu-MAC1 and ^{177}Lu-MAC2 is likely due to the uptake and metabolism by cellular blood components. While long-term blood circulation of the ^{177}Lu-MACs leads to better tumor targeting, the substantial blood retention of the ^{177}Lu-MACs is detrimental to practical application of these agents for diagnostic and radiotherapeutic approaches. Utilizing these initial results, our future designs of the ^{177}Lu-MACs will seek to provide faster blood clearance to better balance the circulation/tumor targeting time and the clearance rates needed for clinical applications.

The significant blood retention of the ^{177}Lu-MACs overall led to high baseline radioactivity values observed in all analyzed tissues. When evaluating the biodistribution data, it is important to keep in mind the contribution to the tissue radioactivity given by blood residing in the tissue. It is undoubtedly true that the high blood activity of the ^{177}Lu-MACs is contributing, to some extent, to the various tissues values, particularly those tissues that normally contain large blood volumes (e.g., liver and kidney). However, as we move from the 24 to the 72 h time-point we observe substantial decreases (~2 fold)

in blood retention and, at the same time, a significant increase in both liver, spleen and tumor retention. The increase in the liver, spleen and tumor retention, while during the same period blood activity reduces, leads us to the conclusion that increases observed in the biodistribution time-points is mostly attributable to the tissue uptake and not background blood activities.

The MPS uptake of nanomedicine platforms is typified by significant accumulation of the delivery system in the liver and spleen. The liver accumulation of the ^{177}Lu-MAC0 demonstrated an increase from 7.27 ± 2.64 to 11.36 ± 1.65 %ID/g over the time course of the experiment. In comparison ^{177}Lu-MAC1 and ^{177}Lu-MAC2 demonstrated lower average accumulation in the liver at every time-point investigated. ^{177}Lu-MAC1 and ^{177}Lu-MAC1 demonstrated a 24 h post-injection liver retention of 3.44 ± 0.82 and 5.29 ± 0.98 %ID/g, but demonstrated nearly identical values at 72 h post-injection. At 72 h post-injection, ^{177}Lu-MAC1 and ^{177}Lu-MAC1 gave liver retention values that were 3.1 and 2.1 times lower than the control (p=0.024,both). With regard to spleen retention, the average spleen retention of ^{177}Lu-MAC0 increased from 7.61 ± 1.37 to 21.46 ± 4.41 %ID/g over the time-points investigated. For the ^{177}Lu-MAC1 and ^{177}Lu-MAC2, the HPMA copolymers demonstrated substantially lower spleen accumulation compared to control. This was particularly evident at the 72 h time-point with spleen values 3.8 and 3.7 times lower (5.63 ± 1.22 and 5.67 ± 0.75 %ID/g) for ^{177}Lu-MAC1 (p = 0.03) and ^{177}Lu-MAC2 (p = 0.06), respectively. The substantial reduction in liver and spleen retention observed in these studies show that the MAL design is capable of enhancing clearance from the MPS tissues.

HPAC tumor accumulation of the ^{177}Lu-MACs was achieved through passive targeting due to the EPR effect. Relative to ^{177}Lu-MAC1 and ^{177}Lu-MAC2, ^{177}Lu-MAC0 demonstrated superior tumor retention at all of the time points studied, with the highest value being 6.58 ± 0.93 %ID/g at 72 h p.i. At 72 h post-injection, ^{177}Lu-MAC1 and ^{177}Lu-MAC2 gave tumor activities of 2.33 ± 0.30%ID/g (p =0.024) and 3.49 ± 0.28 %ID/g (p =0.06), correspondingly, which were significantly lower than control. It is not clear why the tumor retention of the values of ^{177}Lu-MAC1 and ^{177}Lu-MAC2 are substantially lower than those of ^{177}Lu-MAC0. Possibly, the reduced blood retention of the ^{177}Lu-MAC1 and ^{177}Lu-MAC2 or potential metabolism and clearance in the HPAC tumor could contribute to lower overall tumor retention. Unfortunately, the current biodistribution study does not unambiguously demonstrate the in vivo specificity and mechanism of the MACs. Future studies looking into the in vitro and in vivo metabolism of the ^{177}Lu-MACs are planned and will hopefully shed more light with regard to the in vivo tumor-targeting and retention properties of these agents.

2.5 CONCLUSION

In utilizing the MAL design, we seek to take advantage of the relative differences in cathepsin B and S expression as well as the lymphatic and vasculature structure of pancreatic cancer and non-target tissues leading to a decrease in non-target retention of various nanomedicine systems. Herein, we have reported the synthesis and purification of two MALs that are known substrates of cathepsin B and S. These MALs were shown to be metabolized by cathepsin B and S into single metabolites. The MALs were conjugated to the HPMA copolymer and radiolabeled with ^{177}Lu. The synthesized ^{177}Lu-MAC1 and ^{177}Lu-MAC2 demonstrated a substantial decrease in long-term liver and spleen retention relative to the control (^{177}Lu-MAC0). However, compared to the control,

the MALs in ^{177}Lu-MAC1 and ^{177}Lu-MAC2 exhibited higher clearance from HPAC tumors. Our future work will focus on the optimization of the circulation time to achieve faster blood clearance of the MAC design to better suit clinical application. Additionally, further studies into the in vitro and in vivo behavior of the ^{177}Lu-MACs are planned to elucidate the rates of uptake and metabolism in both MPS tissues and pancreatic tumors.

Chapter 3

Cathepsin S Cleavable ^{177}Lu-labeled HPMA Copolymers for Pancreatic Cancer Imaging: Investigation of the Linker Structure-Activity Relationships

3.1 INTRODUCTION

Pancreatic ductal adenocarcinoma (PDAC) is the fourth leading cause of cancer-related deaths in the United States with a 5-year survival rate of only 6% and a median survival of approximately 6 months [132]. The poor prognosis for pancreatic cancer patients is mainly due to the asymptomatic nature of the early disease state with symptoms typically presenting only in advanced stages, where effective treatment options are severely limited [133, 134]. For the small portion of the pancreatic cancer population (< 10%) diagnosed with localized disease, surgical resection has been shown to be an effective treatment and is the current standard of care. Pre-operative staging is crucial in determining whether a patient is a viable candidate for surgical resection [24]. Inaccurate identification of patients with un-resectable tumors leads to unnecessary surgeries that can result in significant increases in patient morbidity and mortality [24]. To date, accurate staging of pancreatic cancer represents a major challenge in patient treatment.

Several noninvasive imaging techniques are currently used for the diagnosis and staging of pancreatic cancer. These modalities include contrast-enhanced computed tomography (CT), abdominal ultrasound (US), magnetic resonance imaging (MRI) and

MR cholangiopancreatography (MRCP) [24]. While these techniques have superb anatomical resolution, these imaging modalities do not have the sensitivity and specificity associated with nuclear imaging instrumentation, namely Single Photon Emission Computed Tomography (SPECT) and Positron Emission Tomography (PET) [135, 136]. Recently, the fusion of nuclear imaging with the CT modality has resulted in hybrid imaging systems, SPECT/CT and PET/CT, which have been demonstrated to more accurately detect and stage a variety of cancers [136]. Unfortunately, the potential of these hybrid imaging systems for improving pancreatic cancer staging has not been fully realized due to the lack of an effective radiotracer to target the disease [24].

The development of polymer-based diagnostics and therapeutics for human disease has been an area of intense research and has yielded several drugs that have progressed to the clinic [137]. N-(2-hydroxypropyl)-methacrylamide (HPMA) copolymer is a polymeric platform that has been extensively investigated for a variety of biomedical applications including the development of SPECT and PET tracers [64, 70, 77, 90, 91, 138-143]. HPMA copolymers are capable of targeting solid tumors either passively, through the enhanced permeability and retention (EPR) effect, and/or actively by inclusion of targeting vectors into the polymeric construct [40, 70, 77, 144]. However, one major challenge for the development of diagnostic and/or therapeutic HPMA based drugs, as well as other polymer and nanomedicine systems, is opsonization and sequestration by the mononuclear phagocyte system (MPS) [126, 145]. In many cases, the sequestration of these polymeric drugs leads to substantial accumulation in the liver and spleen. From a diagnostic perspective, this MPS accumulation in non-target organs can hinder identification of resident or nearby metastatic lesions thereby decreasing the

diagnostic effectiveness. For therapeutic applications, the non-target accumulation of these polymeric drugs can lead to significant toxicities which may be dose-limiting.

Our laboratory is interested in developing synthetic approaches in which HPMA copolymers can be modified to significantly reduce the MPS accumulation thereby enhancing the diagnostic and/or radiotherapeutic efficacy of the agent. Recently, we have described the development of cathepsin S susceptible linkers (CSLs) [146], which degrade in the presence of cathepsin S, a lysosomal protease that is selectively and highly expressed in MPS tissues [117, 147, 148]. From our initial investigation, we found that CSLs significantly reduced long-term retention of ^{177}Lu-labeled HPMA copolymers in tissues associated with the MPS (i.e., liver and spleen). However, the high molecular weight HPMA copolymer (343 kDa) utilized in the study gave blood circulation times that were not ideal for diagnostic or therapeutic use. Herein, we report our continued investigation of the CSL design by evaluating the structure-activity impact of linking groups of varying size on the in vitro and in vivo efficacy of HPMA copolymer based radiopharmaceuticals. In conjunction with these studies, we utilize a lower molecular weight HPMA (109 kDa) copolymer with a blood circulation time that is more suitable for diagnostic and/or radiotherapeutic applications.

3.2 MATERIALS AND METHODS

3.2.1 Synthesis and Characterization of the HPMA Copolymer

The HPMA copolymerization was accomplished using the reversible addition-fragmentation chain transfer (RAFT) polymerization reaction with V-501 as the initiator and CTP as the chain transfer agent. The feed ratio of the polymerization consisted of 98.75:0.85:0.40 mole% HPMA, APMA and APMA-FITC, respectively. Polymerization

was run at a 1 M total monomer concentration in 1 M acetate buffer (pH = 5.2) with a molar ratio of total monomer: chain transfer agent: initiator of 1200:3:1. Prior to proceeding with the polymerization reaction, the glass ampoule and contents were purged with argon for 20 min. Subsequently, the ampoule was flame sealed and allowed to heat at 70 ºC in an oil bath for 14 h. After cooling the HPMA copolymer was evaporated to dryness, dissolved in methanol and purified by size exclusion chromatography using an LH-20 packing material with methanol as the eluent. The conversion rate was 42.3 % as determined by mass measurement after purification. The weight average molecular weight and polydispersity of the copolymers were determined by FPLC equipped with UV and RI detectors. The average molecular weights of the copolymers were estimated using HPMA copolymer standards with narrow polydispersity indices. Quantification of the primary amine content of the HPMA copolymer was assessed using a ninhydrin assay [146].

3.2.2 Solid Phase Peptide Synthesis

For the synthesis of the CSLs with linking groups (CSL2 and CSL3), the resin was manually pre-loaded. Briefly, to a fritted reaction vessel, 2-ClTrl-Cl resin (3 g, 3.60 mmol), 1 equiv of the linker group (Fmoc-5-Ava-OH or Fmoc-NH-$(PEG)_2$-COOH) and 4 equiv of DIEA in dry DMF (30 mL) was added. The reaction mixture was stirred for 2 h, filtered and washed sequentially with: (1) 3 X 100 mL of a solution consisting DCM/MeOH/DIEA (17:2:1); (2) 3 X 100 mL of DCM (3) 2 X 100 mL of DMF and (4) 2 X 100 mL of DCM. The resin was dried in vacuum over KOH. For estimating residue loading, the Fmoc group from a small sample of the resin was cleaved with 2% DBU in DMF and the concentration of liberated dibenzofulvene was measured by UV spectroscopy (304 nm). Using known standards of Fmoc-Gly-OH as a reference, the

residue loading was estimated from the equation: mmole/g = (Abs_{sample}-Abs_{ref}) *16.4/mg of resin [149]. Estimation of the level of residue attachment indicated substitution of 0.60 and 0.65 mmol/g for the Fmoc-5-Ava-trityl and Fmoc-NH-$(PEG)_2$-trityl resin, respectively.

The CSLs were synthesized using automated solid phase peptide synthesis. Briefly, the resin (containing 0.25 mmole of peptide anchors) was deprotected using piperidine resulting in the formation of the primary amine. The carboxylic acids of the Fmoc protected amino acids (1 mmol) were activated using COMU and conjugated to the primary amines of the growing peptide on the resin. The process of deprotection, activation and conjugation was repeated until the desired peptide was synthesized. The selective cleavage of the peptide from the 2-chlorotrityl resin anchor was achieved by reaction with 1% TFA in dry DCM and subsequent filtration. The combined crude filtrates were dried by a rotary concentrator. Purification of the peptides was performed using a semi-preparative Proteo C_{12} column with a flow rate of 5.0 mL/min. HPLC solvents consisted of H_2O containing 0.1% formic acid (solvent A) and acetonitrile containing 0.1% formic acid (solvent B). For all peptides, the initial gradient of 70% A: 30% B linearly decreased to 60% A: 40% B over a 15 min time period. At the end of the run time for all HPLC experiments, the column was flushed with the gradient 5% A: 95% B and re-equilibrated to the starting gradient. The yields after purification were 0.1326 g (37.5%) for CSL1; 0.166 g (44%) for CSL2 and 0.109 g (27.1%) for CSL3. The peptides were confirmed to be ≥ 95% purity as characterized by LC/MS before in vitro/ in vivo use.

3.2.3 Synthesis of Cathepsin S Cleavable Copolymers (CSCs)

The CSCs were prepared by condensation of the HPMA copolymer and the CSLs as previously described. Briefly, in a 10 mL round bottom flask, 16.5 (28.9 μmol, 5.0 equiv), 16.5 (11.6 μmol, 2.0 equiv), 17.4 (11.6 μmol, 2.0 equiv) or 18.6 mg (11.6 μmol, 2.0 equiv) of CSL0, CSL1, CSL2 or CSL3 was dissolved in 600 μL of DMF. The solution was cooled to 0 °C and 2.4 equivalents of NHS and DCC, relative to the CSL, were added to the flask. The solution was stirred at 0 °C for 3 h. At the end of that time, the HPMA copolymer was added and stirred for another 2 h at 0 °C. Subsequently, the reaction was allowed to warm to room temperature and continued overnight. The precipitate generated from the reaction was filtered off and the filtrate was evaporated to dryness. The residue was dissolved in methanol, isolated by size exclusion chromatography using an LH-20 packing material and evaporated to dryness. The attached protected peptides of the resulting CSCs were deprotected using standard peptide cleavage conditions. In the case of CSC0, the copolymer was added to 4 mL of a cleavage cocktail consisting of a 1:1:1:37 volumetric ratio of DODT, water, TIS and TFA. This solution was kept at 0 °C and stirred for 2 h. For CSC1-3, the cleavage cocktail contained a 1:1:1:0.75:46.25 volumetric ratio of DODT, water, TIS, thioanisole, and TFA. After deprotection, the mixture was evaporated to dryness and the polymers were finally purified by size exclusion chromatography using an LH-20 packing material and methanol as the eluent. The conjugation yield for CSC0 was determined by the ninhydrin assay. For CSC1-3, the conjugation yield was determined using amino acid analysis conducted by the UNMC Protein Structure Core Facility.

3.2.4 Radiolabeling of the CSCs

The radiolabeling of the CSCs was accomplished by heating 200 μg of the CSC at 90 °C for 1 h in the presence of 37 MBq (~1mCi) of $^{177}LuCl_3$. After cooling, the resulting

^{177}Lu-radiolabeled CSC was purified by radio-SEC-HPLC. Purification of the ^{177}Lu-CSCs was accomplished using a Biosep-SEC-S2000 column with an isocratic mobile phase consisting of PBS with 0.02 M EDTA at pH 7.2. The linear flow rate was 0.80 mL/min. UV analysis was performed at a wavelength of 494 nm. After collection of the peak-purified ^{177}Lu-CSC, approximately 10 mg of L-ascorbic acid was added to inhibit radiolysis. The purified ^{177}Lu-CSC was concentrated using an Amicon Ultra-4 centrifugal filter (10 kDa) and washed with 2 X 4 mL of deionized water. The radiochemical purity of all radio-conjugates was re-evaluated prior to in vitro/ in vivo use and found to be ≥ 95 % pure as determined by the radio-HPLC.

3.2.5 Cathepsin Cleavage Assay of Radiolabeled Copolymers

Human cathepsin S (20 ng/µL) in 100 µL of buffer solution (50 mM sodium acetate, 1 mM EDTA and 10 mM DTT, pH 6.0) was incubated with 100 µg of each purified ^{177}Lu-CSC0-3 at 25 ºC. After 12 h, a 50 µL aliquot of each copolymer solution was analyzed by radio-SEC-HPLC to determine the relative amount of cathepsin S cleavage product. The analysis utilized an isocratic gradient at a linear flow rate of 0.80 mL/min with a mobile phase consisting of PBS with 0.02 M EDTA at pH 7.2. The UV analysis of the HPLC eluent was carried out at a wavelength of 494 nm.

3.2.6 Human Serum Stability of Radiolabeled Copolymers

Briefly, 10 µg of purified ^{177}Lu-CSC was incubated with 1 mL of human AB serum at 37 °C. After 144 h, the stability was determined by centrifuge filtration using an Amicon Ultra-4 10 kDa filter. A 100µL aliquot was loaded in the filter and diluted to 4 mL using DI water. The loaded sample was centrifuged and washed with 4 mL of DI water. The

percent of intact ^{177}Lu-CSC was calculated by dividing the remaining radioactivity in the 10 kDa filter to the total radioactivity added.

3.2.7 Cell Culture

The HPAC cells were cultured in our laboratory, as per ATCC protocols, in DMEM/Ham's F12 medium containing 5% FBS, 1.562 nM EGF, 14.3 mM sodium bicarbonate, 2.5 mM L-glutamine, 15 mM HEPES and 0.5 mM sodium pyruvate supplemented with 0.350 µM insulin, 0.0625 µM transferrin and 0.110 µM hydrocortisone. Cells were incubated at 37 °C with 5% CO_2 in air.

Human monocytes were provided by the UNMC Elutriation Core Facility. Monocytes were plated into T75 tissue culture flasks at a concentration of 20 x10^6 cells in 20 mL of macrophage differentiation medium: DMEM containing 10% FBS, 1% NEAA, 500 U rhM-CSF, 1% Penicillin/Streptomycin, 2 mM l-glutamine and 1% sodium-pyruvate. Media was half-exchanged every 2 to 3 days for 7-10 days, at which time, visual confirmation of differentiation led to media replacement with the macrophage maintenance medium (differentiation media without the rhM-CSF). Cells were maintained in a 37 °C humidified atmosphere with 5% CO_2.

3.2.8 Confocal Microscopy

Macrophage cells and HPAC cells were seeded onto 4-well chambered coverglass units with 1 × 10^4 and 5 × 10^4 cells, respectively. FITC-labeled polymer conjugates were diluted in blank media to 100 µg/mL concentration. The cells were then incubated with the polymer for 24 h in a 37 °C humidified atmosphere with 5% CO_2. Half an hour before

the end of this incubation, LysoTracker Red DND-99 and Hoechst 33342 were added in the media to stain the lysosomal compartment and the nuclei. Following incubation, the media was aspirated, and the cells were washed with PBS to remove free polymers that were not internalized prior to confocal imaging.

3.2.9 Immunoblot Analysis

Whole cell HPAC and differentiated macrophage lysate as well as mice HPAC tumor homogenate were prepared using RIPA buffer and a cocktail of proteases inhibitors. The lysates and homogenate were centrifuged at 13,000 RPM at 4 ºC for 20 min. The supernatants containing 50 µg total proteins were mixed with sample buffer and then separated by 10% SDS-PAGE, followed by transfer to PVDF membrane. After blocking in 5% nonfat milk, 0.1% Tween-20, and Tris-buffered saline at room temperature for 1 h, membranes were probed with primary antibodies in blocking solution for 1 h at room temperature, followed by extensive washing in TBS. Rabbit anti-goat and goat anti-mouse secondary antibodies were used for the detection of immunoreactive proteins by chemiluminescence.

3.2.10 Biodistribution Studies

Biodistribution studies were carried out using age-matched normal CF-1 and HPAC tumor bearing SCID mice. For biodistribution studies involving HPAC xenograft mice, the mice were inoculated in each flank with 100 µL of a 1:1 ratio of suspended HPAC **c**ells and Matrigel™ to obtain a final concentration of 5 x 10^6 HPAC cells per 100 µL. Upon achieving sufficient tumor size, (10-15 mm in diameter) the mice were considered viable for biodistribution studies. The CF-1 mice and HPAC xenograft mice were injected with a

0.37 MBq (10 μCi) intravenous bolus of the purified ^{177}Lu-CSCs. The mice were sacrificed and their tissues excised at 4, 24, 72 and 144 h time points post-injection (p.i.). The blood and excised tissues were weighed, the ^{177}Lu radioactivity measured using a gamma counter, and the percentage injected dose (%ID) and the percentage injected dose per gram (%ID/g) calculated for each tissue.

3.2.11 SPECT/CT Imaging Studies

Xenograft mice were intravenously injected with 400~600 μCi of CSCs in 100 μL saline and then anesthetized with 5% isoflurane delivered in 0.5 mL/min oxygen. Image acquisition with a 5-pinhole (1.0 mm/pinhole) collimator was acquired at 4, 24, 72 and 144 h time-points p.i. Five hundred and twelve CT projections for each image were acquired and reconstructed using Triumph X-O 4.1 at a matrix size of 512×512×512 with a 0.15-mm voxel dimension. Sixty four SPECT projections for each image were acquired using a Triumph SPECT with a 20% window at 208 keV for ^{177}Lu and reconstructed using Triumph SPECT Reconstruction Application 1.0.8.0 at a matrix size of 64×64×64 with a 1.14 mm voxel dimension. Co-registration of anatomical CT images and functional SPECT was performed using 3D image visualization and analysis software VIVID based on Amira 4.1. A median filter was applied to all SPECT images.

3.2.12 Statistics

Statistical analyses were done using a two-tailed unpaired Student's t-test (2 groups) or one way ANOVA (> 2 groups) with Bonferroni post-tests, a $p < 0.05$ indicating statistically significant differences.

3.3 RESULTS AND DISCUSSION

3.3.1 Design and Synthesis of Cathepsin S Cleavable Linkers (CSLs)

Herein, we report the evaluation of a series of CSLs incorporated into a ^{177}Lu-labeled HMPA copolymer construct. The objective of our approach is to utilize the CSLs to enhance the diagnostic/therapeutic potential of HPMA copolymer based drugs by improving the clearance properties of these agents from MPS associated tissues, in particular the liver and spleen. The CSLs, depicted in Figure 3.1, are composed of four components: 1) the DOTA moiety that is responsible for chelation of the diagnostic/ therapeutic radiometal; 2) the P-M-G-L-P substrate (**Y**) which cleaves in the presence of cathepsin S [146, 150]; 3) a clearance sequence (**X**), in this case G-(D)S-D(S), that can be modified to influence the clearance rate of the resulting radiometabolite; and finally 4) the linker group (**Z**) that is used to optimize the distance of the cathepsin S substrate from the polymer backbone. The distance of the cathepsin S substrate from the HPMA copolymer backbone is expected to be a factor, due to steric inhibition, that influences the cleavage rate of the cathepsin S substrate. In this study we investigate the impact of linking groups of various lengths (0, 6 and 13 atoms) on the in vitro cleavage rate and in vivo performance of CSLs incorporated into ^{177}Lu-labeled HPMA copolymers.

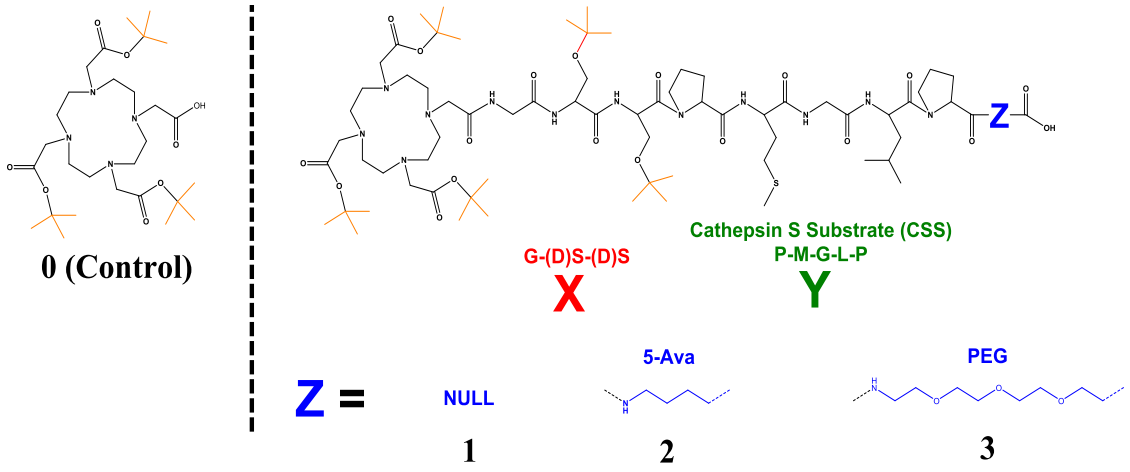

Figure 3.1: Schematic design of CSLs with intact orthogonal protection.

As shown in Figure 3.1, we chose to investigate CSL1-3 containing a null, a six atom hydrocarbon (5-Ava) and a 13 atom polyethylene glycol (PEG) linking group, respectively. In the case of CSL3, a PEG linker was chosen in place of a 13 atom hydrocarbon chain in order to reduce the potential for hydrophobic, intramolecular associations that would have likely limited separation of the cathepsin S substrate and the HPMA copolymer backbone [151, 152]. The control for our study, CSL**0**, is simply the DOTA chelation system absent of any peptide components. The CSL1-3 were synthesized with intact orthogonal protection using automated solid-phase peptide synthesis. The synthesis of the CSLs with orthogonal protection results in the generation of a single carboxylic acid functionality at the C-terminus which will later be used for conjugation to the HPMA copolymer. Purification of the crude synthetic peptides by HPLC gave yields of 37.5, 44.0 and 27.1 for CSL1-3, respectively. The HPLC and mass spectrometric data of the CSLs are given in Table 3.1.

Table 3.1: Characterization of CSLs.

CSL Peptides	Sequences	Formula	Mass Expected $[M+H]^+$	Mass Observed $[M+H]^+$
CSL0	$DOTA(tBu)_3$	$C_{28}H_{52}N_4O_8$	573.4	573.2
CSL1	$DO3A(tBu)_3$-G-(D)S(tBu)-(D)S(tBu)-P-M-G-L-P	$C_{67}H_{118}N_{12}O_{18}S$	1411.8	1411.5
CSL2	$DO3A(tBu)_3$-G-(D)S(tBu)-(D)S(tBu)-P-M-G-L-P-5-Ava	$C_{72}H_{127}N_{13}O_{19}S$	1510.9	1510.6
CSL3	$DO3A(tBu)_3$-G-(D)S(tBu)-(D)S(tBu)-P-M-G-L-P-PEG3	$C_{76}H_{135}N_{13}O_{22}S$	1615.0	1614.7

3.3.2 Synthesis and Characterization of Cathepsin S Cleavable Copolymers (CSCs)

The scheme for synthesis of the CSCs is depicted in Figure 3.2. The HPMA copolymer consisting of HPMA, APMA and APMA-FITC monomers were prepared by RAFT polymerization. The estimated molecular weight of the synthesized HPMA copolymer was 109 kDa with a polydispersity of 1.3 as determined by FPLC analysis. Ninhydrin assay revealed a total amine concentration of 57.2 µmol/g (n=1), which corresponds, based on the feed content, to 97% incorporation of the APMA monomer. On average, this yields approximately six APMA moieties per polymer backbone. Conjugation of CSLs to HPMA copolymers was accomplished using EDC/NHS amidation chemistry. The orthogonal protection of the CSLs allowed for the chemo-selective conjugation of the C-terminal carboxylic acid to the APMA moiety on the HPMA copolymer. Conjugation of the DOTA chelation system to the HPMA copolymer (CSC0) gave a DOTA content of 31.3 µmol/g polymer (n=1), corresponding to a 54% conjugation yield, as evaluated by ninhydrin assay. Amino acid analysis of the conjugation of CSL1-3 to the HPMA copolymer gave a peptide content of 15.0, 13.4 and 12.7 µmol/g polymer (n=3), which corresponds to 26.0, 23.4 and 22.2 % for CSC1-3, respectively. The orthogonal protecting groups were removed with a cleavage cocktail (92.5% TFA) to give the deprotected CSCs. Size exclusion chromatography was used to purify the CSCs prior to radiolabeling.

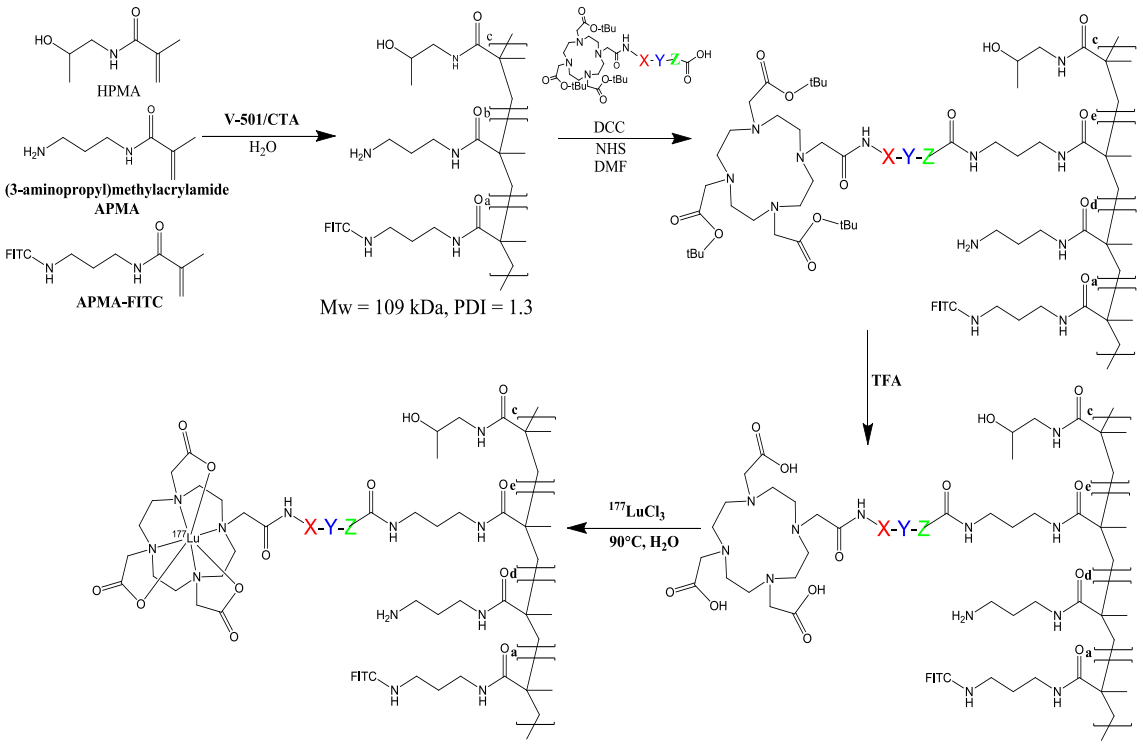

Figure 3.2: Schemes for the synthesis of the ^{177}Lu-CSC conjugates. For CSC0, CSC1, CSC2 and CSC3, X = Y = Z = null; X = GSS, Y = PMGLP; X = GSS, Y = PMGLP Z = 5-Ava and X = GSS, Y = PMGLP Z = PEG3, respectively.

3.3.3 Synthesis of ^{177}Lu-labeled CSCs

The ^{177}Lu-labeled CSCs were prepared by heating $^{177}LuCl_3$ in the presence of CSCs at 90°C for 1 h. The radiochemical yields for CSC0-4, as determined by radio-SEC-HPLC, were on average (n=3) 77%, 90%, 43% and 81%, respectively. Correspondingly, the achievable specific activities were 142.45, 166.50, 79.55 and 149.85 MBq/mg.

3.3.4 Serum Stability and Cleavage Studies of ^{177}Lu-Labeled CSCs

The stability of the ^{177}Lu-CSCs in human serum was investigated over the course of 144 h at 37°C. At the end of this incubation period, 98% of the ^{177}Lu-CSCs remained intact thus suggesting that the ^{177}Lu-CSCs would be stable to serum proteases in vivo while in circulation. It is important to note that this stability study does not reflect potential uptake and metabolism by cellular components of the blood (e.g., circulating monocytes), which likely impacts the stability of the ^{177}Lu-CSCs in circulation. The in vitro susceptibility of the ^{177}Lu-CSCs to cathepsin S cleavage was investigated by incubating the radiolabeled copolymers at 37°C for 12 h in the presence of cathepsin S. Analysis of aliquots of the reaction medium by radio-SEC-HPLC, Figure 3.3, revealed that ^{177}Lu-CSC1-3 underwent proteolytic cleavage when challenged with cathepsin S. The non-cleavable control CSC0, not shown, was found to be stable in the presence of cathepsin S over 72 h. All of the intact ^{177}Lu-CSCs demonstrated a retention time of approximately 10.5 min on the SEC column. Upon cleavage, the generated radiometabolite resulted in a substantially higher retention time of 12.4 min, which corresponds to the expected reduction in molecular weight. We have previously demonstrated that the cleavage site for the CSLs are between the glycine and leucine residues (P-M-G┼L-P) of the substrate sequence [146]. Over the 12 h incubation period, the ^{177}Lu-CSC1-3 demonstrated an average (n=2-3) of 8.4, 10.1 and 25.9 % cleavage, correspondingly.

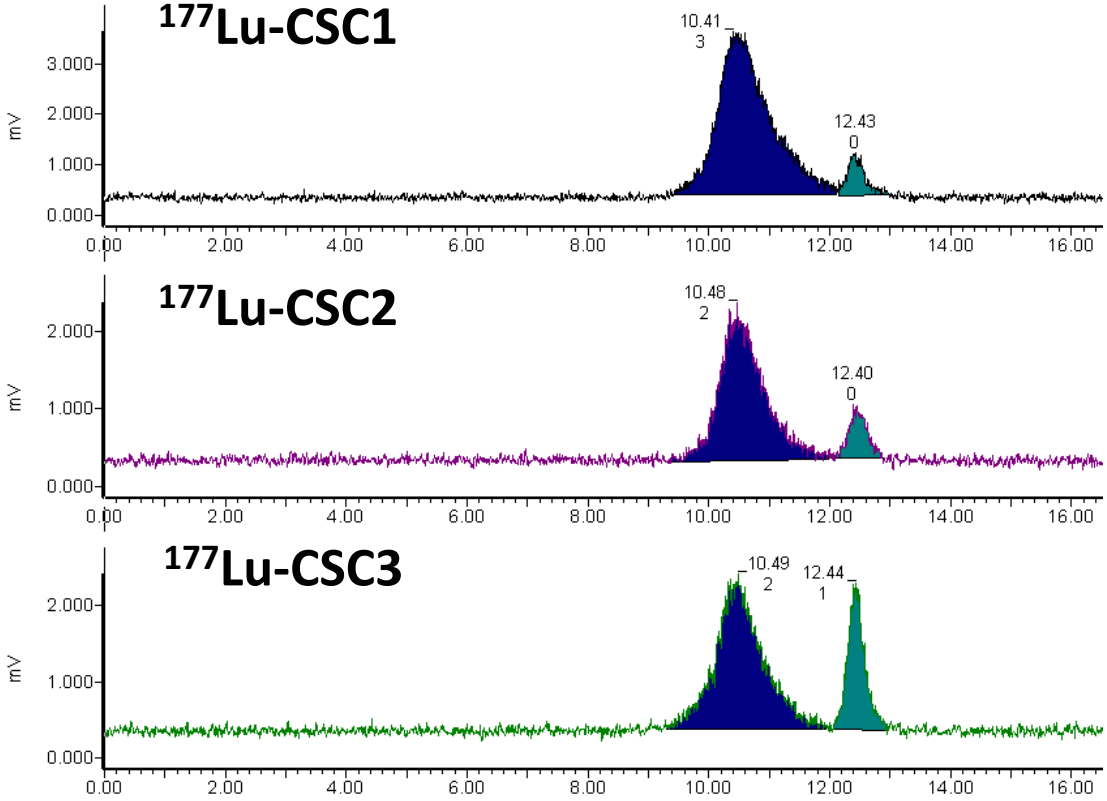

Figure 3.3: Chromatograms of CSC1-3 after a 12 h incubation with cathepsin S.

As stated previously, the proximity of the metabolic sequence to the HPMA copolymer backbone is expected to influence the cleavage rate of the CSCs. Our basis for the introduction of linking groups of various lengths (Z) into the CSLs was to investigate the structure-activity relationship, with respect to cathepsin S activity, of the CSLs when integrated into the HPMA copolymers. From the above data, some insight can be gleaned regarding the structure-activity relationship of the HPMA copolymer incorporated CSLs. The inclusion of the smaller linking group, 5-Ava, into the CSL (^{177}Lu-CSC2) gave no statistically significant increase in cleavage relative to the null analog (^{177}Lu-CSC1). In the case of ^{177}Lu-CSC3, the introduction of the longer PEG linking group gave much higher rates of cathepsin S cleavage. These data suggest that the length of the linking group is capable of influencing the cathepsin S cleavage activity likely through a reduction of steric hindrance.

3.3.5 Cathepsin S Expression in HPACs and Macrophages

It is well known that the MPS is primarily responsible for the non-target accumulation of nanomedicine platforms, particularly in the liver and spleen [153]. The MPS is composed of phagocytic cells (e.g., macrophages and monocytes) that sequester drug delivery systems which typically results in loss of diagnostic/therapeutic effectiveness and potential toxicity. These phagocytic cells are also known as antigen presenting cells (APCs) due to their function in adaptive immunity where these cells process pathogenic material and present antigen fragments on the cellular surface. Cathepsin S is a predominantly lysosomal proteolytic enzyme that has been shown to be highly regulated, relative to other cathepsins (e.g., cathepsin B), and predominately expressed in APCs [154]. The substantial expression of cathepsin S in APCs is thought to be due to its unique role in the catabolism of pathogenic proteins [155-157]. Our design seeks to take

advantage of the cathepsin S expression/activity in APCs to preferentially enhance clearance from non-target tissues [134, 146].

In this study, we utilize the HPAC human pancreatic cancer cell line as our in vitro and in vivo model of pancreatic cancer. Human monocytes have been differentiated to macrophages to serve as our model of tissue-resident macrophages. In order to determine cathepsin S expression, immunoblotting was performed on both cell types. As shown in Figure 3.4, cathepsin S is highly expressed in differentiated macrophages with negligible detectable expression in the HPAC cells. Overall, this corresponds well with our previous observations that the cathepsin S protease activity is much higher (tenfold) in differentiated macrophages versus the HPAC cell line [146]. Evaluation of the cathepsin S expression in HPAC tumor homogenates revealed increased levels of cathepsin S relative to cultured cells. This relative increase in expression may be a consequence of the dissimilarity of the in vivo tumor microenvironment versus the in vitro cultured milieu. However, it seems likely that the escalation in cathepsin S signal may, at least partially, be attributable to tumor-associated macrophages (TAM), which exist in almost all solid tumors [158].

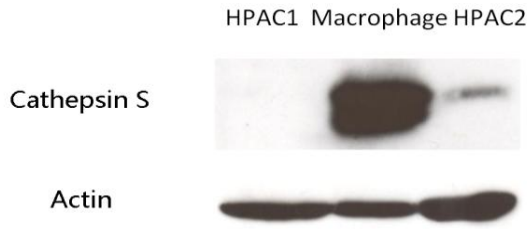

Figure 3.4: Western Blot analysis of cathepsin S expressions in cultured HPACs (HPAC1), differentiated macrophages, and HPACs from corresponding in vivo tumor-derived cells (HPAC2).

The intracellular trafficking of FITC-labeled copolymers in both the differentiated macrophages and the HPAC cell line was investigated using confocal microscopy, Figure 3.5. In these studies, the CSC0 was utilized as our model HPMA copolymer. Lysotracker® Red and Hoechst fluorescent markers were used to delineate the lysosome and nucleus compartments, respectively. After 24 h incubation with CSC0, the differentiated macrophages (Figure 3.5A) demonstrated substantially higher levels of cellular accumulation relative to the HPAC cell line (Figure 3.5B). This is in accordance with our previously reported flow cytometric studies working with a higher molecular weight HPMA copolymer [146]. As can be seen in the overlay, the CSC0 accumulation in the macrophages is co-localized with the Lysotracker® Red marker. The accumulation of HPMA copolymers in lysosomal compartments is in agreement with previous literature reports [159, 160]. By accumulating in the macrophage lysosomes, the CSCs are co-localized with the highest sub-cellular concentrations of cathepsin S. The selective uptake of the CSCs in macrophages and the accumulation of the copolymer in the lysosomal compartments are expected to substantially and selectively increase the CSC cleavage kinetics in macrophages and other APC cell types. The proteolytic degradation of the CSCs will result in the formation of low molecular weight radiometabolites which are anticipated to clear more rapidly from the APC cells residing in non-target tissues and ultimately result in higher clearance.

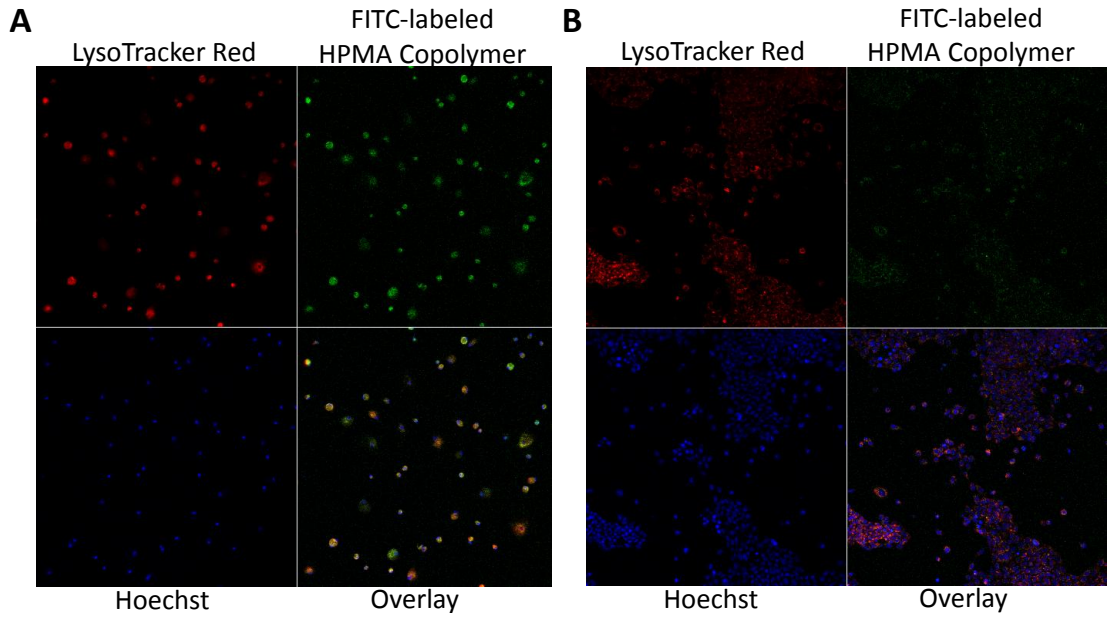

Figure 3.5: After 24 h incubation, FITC-labeled HPMA copolymer showed intense accumulation in lysosomes of macrophages (A) (B).

3.3.6 Biodistribution Studies of ^{177}Lu-CSCs

The biodistribution properties of the ^{177}Lu-CSCs were investigated at 4, 24, 72 and 144 h post-administration in both a normal CF-1 (Table 3.2) and HPAC xenograft mouse models. With exception of the blood clearance rate (elaborated on below), the ^{177}Lu-CSCs demonstrated similar biodistribution trends in both animal models. The data obtained from the biodistribution studies of the ^{177}Lu-CSCs in a HPAC xenograft mouse model are given in Table 3.3. The calculated tumor-to-non-target ratios for selective tissues are given in Table 3.4. At the 4 h p.i. time point, the ^{177}Lu-CSCs revealed excretion values that ranged from 23.82 ± 3.23 - 34.57 ± 2.41 %ID. Those HPMA copolymers with the cathepsin S cleavable linkers (^{177}Lu-CSC1-3) demonstrated significantly higher levels of radioactivity excretion relative to the non-cleavable control (^{177}Lu-CSC0) by the 24 h time point ($p < 0.05$). At the 144 h time point, 83.29 ± 1.24 - 87.93 ± 1.49 %ID of the ^{177}Lu-CSC1-3 had been eliminated from the body in comparison to only 55.65 ± 2.26 %ID of ^{177}Lu-CSC0 ($p < 0.0001$). The overall elimination of radioactivity from the mouse corresponded well to the blood retention profiles of the ^{177}Lu-CSCs. At 4 h p.i., all four ^{177}Lu-CSCs demonstrated blood retention profiles that were statistically identical. By the 24 h time-point, ^{177}Lu-CSC1 and ^{177}Lu-CSC2 demonstrated significantly lower blood retention ($p < 0.05$) relative to the control. The blood retention of ^{177}Lu-CSC1-3 at 72 and 144 h post-administration were all substantially lower ($p < 0.001$), 2.2 - 2.9 and 3.0 - 4.4 fold lower, respectively, in comparison to ^{177}Lu-CSC0. Comparison of the blood clearance profile of the ^{177}Lu-CSCs in both the CF-1 and HPAC xenograft model revealed that the CF-1 model demonstrated a relative two-fold lower retention for all ^{177}Lu-CSCs at all time points investigated. This suggests that the alterations made to the SCID model (i.e., absence of functional T and B lymphocytes) may be impacting the blood clearance of the ^{177}Lu-CSCs. However,

when the blood clearance profiles are taken into account, the overall trends of the ^{177}Lu-CSCs, with respect to uptake, retention and clearance, in solid tissues remain consistent among the two models.

Table 3.2: Biodistribution of ^{177}Lu-labeled CSCs in CF-1 mice. N=5 at each time-point. Data are represented as mean ± SD %ID/g.

	^{177}Lu-0	^{177}Lu-1	^{177}Lu-2	^{177}Lu-3	^{177}Lu-0	^{177}Lu-1	^{177}Lu-2	^{177}Lu-3
	4 h p.i.				**24h p.i.**			
blood	13.61 ± 2.35	12.03 ± 1.58	13.85 ± 3.13	13.72 ± 2.82	6.17 ± 1.20	3.82 ± 0.65	2.77 ± 0.49	4.57 ± 0.56
heart	3.40 ± 1.01	3.54 ± 0.50	5.57 ± 1.18	4.33 ± 1.14	2.10 ± 0.22	1.65 ± 0.16	1.50 ± 0.62	1.97 ± 0.12
lung	4.47 ± 1.39	3.84 ± 0.50	3.93 ± 0.77	3.97 ± 0.92	2.08 ± 0.28	1.90 ± 0.25	1.07 ± 0.19	1.89 ± 0.35
liver	2.92 ± 0.55	2.47 ± 0.15	2.73 ± 0.37	3.16 ± 0.66	2.56 ± 0.31	1.79 ± 0.29	1.74 ± 0.25	2.15 ± 0.19
pancreas	1.74 ± 0.33	1.96 ± 0.59	2.72 ± 1.29	2.39 ± 0.34	1.08 ± 0.10	1.10 ± 0.08	1.26 ± 0.43	1.26 ± 0.20
stomach	1.62± 1.06	1.33 ± 0.33	1.05 ± 0.23	1.46 ± 0.66	0.66 ± 0.11	0.97 ± 0.19	0.53 ± 0.21	0.49 ± 0.07
spleen	2.55 ± 0.43	2.11 ± 0.29	1.66 ± 0.29	2.65 ± 0.71	2.33 ± 0.26	1.26 ± 0.19	1.14 ± 0.21	1.92 ± 0.65
small int.	2.26 ± 0.53	2.01 ± 0.42	2.46 ± 0.44	2.61 ± 0.65	1.22 ± 0.25	1.21 ± 0.32	0.80 ± 0.10	1.29 ± 0.07
large int.	3.30 ± 1.34	3.11 ± 0.48	1.94 ± 0.26	2.62 ± 1.17	1.46 ± 0.45	1.43 ± 0.35	0.99 ± 0.07	1.04 ± 0.19
kidney	3.77 ± 0.87	3.88 ± 0.97	3.68 ± 0.42	3.67 ± 0.93	2.06 ± 0.33	1.93 ± 0.12	1.59 ± 0.39	2.03 ± 0.11
muscle	0.79 ± 0.23	0.76 ± 0.15	1.14 ± 0.37	0.98 ± 0.38	0.56 ± 0.06	0.62 ± 0.11	1.17 ± 0.49	0.63 ± 0.11
bone	1.22 ± 0.29	1.09 ± 0.06	1.97 ± 0.68	1.37 ± 0.44	0.68 ± 0.09	0.73 ± 0.08	0.89 ± 0.25	0.71 ± 0.07
brain	0.40 ± 0.14	0.35 ± 0.08	0.47 ± 0.17	0.59 ± 0.05	0.18 ± 0.03	0.19 ± 0.02	0.12 ± 0.04	0.21 ± 0.05
Excretion	21.56 ± 11.0	28.36 ± 3.31	37.02 ± 6.24	23.12 ± 5.59	56.15 ± 15.65	55.37 ± 2.89	59.03 ± 5.28	53.78 ± 1.90
	72 h p.i.				**144 h p.i.**			
blood	3.42 ± 0.78	1.18 ± 0.16	0.47 ± 0.09	1.13 ± 0.19	1.40 ± 0.30	0.38 ± 0.10	0.07 ± 0.04	0.26 ± 0.05
heart	1.80 ± 0.17	1.00 ± 0.08	0.80 ± 0.19	0.97 ± 0.20	1.65 ± 0.37	0.55 ± 0.04	0.42 ± 0.07	0.61 ± 0.08
lung	1.75 ± 0.36	0.78 ± 0.20	0.50 ± 0.10	0.79 ± 0.19	1.20 ± 0.18	0.25 ± 0.06	0.20 ± 0.06	0.33 ± 0.05
liver	3.49 ± 0.75	1.82 ± 0.36	0.91 ± 0.10	1.46 ± 0.08	3.45 ± 0.38	0.82 ± 0.06	0.54 ± 0.03	1.06 ± 0.08
pancreas	1.44 ± 0.47	0.82 ± 0.23	0.78 ± 0.34	0.73 ± 0.12	1.35 ± 0.53	0.53 ± 0.09	0.37 ± 0.11	0.45 ± 0.08
stomach	0.58 ± 0.16	0.46 ± 0.14	0.26 ± 0.07	0.36 ± 0.13	0.41 ± 0.17	0.11 ± 0.03	0.08 ± 0.03	0.15 ± 0.05
spleen	4.31 ± 1.47	1.85 ± 0.71	0.78 ± 0.28	1.45 ± 0.09	6.70 ± 3.46	0.82 ± 0.34	0.67 ± 0.41	1.05 ± 0.12
small int.	0.85 ± 0.19	0.54 ± 0.10	0.32 ± 0.06	0.47 ± 0.08	0.50 ± 0.07	0.23 ± 0.03	0.18 ± 0.03	0.22 ± 0.05
large int.	1.42 ± 0.27	1.22 ± 0.37	0.54 ± 0.04	0.64 ± 0.20	0.91 ± 0.14	0.35 ± 0.03	0.19 ± 0.02	0.32 ± 0.09
kidney	1.76 ± 0.31	1.04 ± 0.17	0.77 ± 0.14	1.01 ± 0.15	1.17 ± 0.24	0.49 ± 0.08	0.42 ± 0.04	0.61 ± 0.21
muscle	0.59 ± 0.08	0.42 ± 0.10	0.49 ± 0.13	0.44 ± 0.10	0.57 ± 0.15	0.19 ± 0.03	0.27 ± 0.07	0.22 ± 0.02
bone	1.03 ± 0.21	0.49 ± 0.13	0.54 ± 0.08	0.58 ± 0.18	0.72 ± 0.37	0.37 ± 0.11	0.26 ± 0.05	0.32 ± 0.12
brain	0.18 ± 0.03	0.06 ± 0.02	0.03 ± 0.01	0.07 ± 0.04	0.11 ± 0.02	0.03 ± 0.02	0.01 ± 0.01	0.02 ± 0.01
Excretion	56.94 ± 4.15	74.62 ± 1.48	81.62 ± 2.14	74.14 ± 3.35	61.71 ± 3.94	86.65 ± 0.71	89.11 ± 0.41	84.24 ± 0.60

Table 3.3: Biodistribution of ^{177}Lu-labeled CSCs in HPAC tumor bearing mice. N=5 at each time-point. Data are represented as mean ± SD %ID/g.

Tissue	^{177}Lu-0	^{177}Lu-1	^{177}Lu-2	^{177}Lu-3	^{177}Lu-0	^{177}Lu-1	^{177}Lu-2	^{177}Lu-3
	4 h p.i.				**24 h p.i.**			
Blood	21.02 ± 6.09	17.62 ± 2.87	16.42 ± 2.87	20.47 ± 2.19	11.34 ± 2.24	5.80 ± 0.62	6.87 ± 1.15	9.22 ± 1.78
Heart	6.33 ± 2.04	5.05 ± 0.97	4.64 ± 1.30	5.12 ± 1.81	3.77 ± 0.35	2.44 ± 0.19	2.65 ± 1.10	3.00 ± 0.82
Lung	6.68 ± 1.09	5.32 ± 1.26	5.73 ± 1.48	6.44 ± 2.22	3.87 ± 1.18	2.83 ± 0.40	2.78 ± 0.58	4.02 ± 0.87
Liver	4.97 ± 0.74	4.20 ± 0.64	4.27 ± 0.38	5.13 ± 0.64	4.74 ± 0.65	3.33 ± 0.05	4.21 ± 0.32	4.88 ± 0.90
Pancreas	2.92 ± 0.57	2.48 ± 0.12	2.50 ± 0.66	2.98 ± 0.76	3.09 ± 1.07	2.05 ± 0.76	1.96 ± 0.47	1.65 ± 0.57
Stomach	1.04 ± 0.29	1.15 ± 0.27	1.00 ± 0.27	1.15 ± 0.28	0.93 ± 0.35	0.76 ± 0.18	0.72 ± 0.29	0.73 ± 0.27
Spleen	3.35 ± 0.56	2.88 ± 0.83	4.04 ± 1.56	3.55 ± 0.61	7.79 ± 1.47	3.24 ± 1.29	4.53 ± 2.21	4.93 ± 0.66
Small Int.	1.96 ± 0.34	2.06 ± 0.74	1.56 ± 0.29	1.66 ± 0.52	1.03 ± 0.13	0.68 ± 0.11	0.69 ± 0.13	0.96 ± 0.22
Large Int.	1.88 ± 0.20	3.84 ± 3.42	2.33 ± 0.59	1.93 ± 0.43	1.25 ± 0.37	1.24 ± 0.16	1.50 ± 0.26	1.67 ± 0.33
Kidney	5.28 ± 1.25	5.08 ± 1.06	3.81 ± 0.76	4.63 ± 0.88	3.01 ± 1.01	2.38 ± 0.44	2.58 ± 0.20	3.03 ± 0.72
Muscle	1.21 ± 0.24	1.22 ± 0.24	1.58 ± 0.95	1.22 ± 0.31	1.89 ± 1.14	1.26 ± 0.70	1.07 ± 0.31	1.37 ± 0.42
Bone	1.52 ± 0.21	1.68 ± 0.21	1.65 ± 0.37	1.59 ± 0.21	1.42 ± 0.34	1.39 ± 0.19	1.14 ± 0.20	1.17 ± 0.21
Brain	0.68 ± 0.09	0.70 ± 0.10	0.48 ± 0.08	0.56 ± 0.10	0.46 ± 0.08	0.29 ± 0.10	0.28 ± 0.04	0.25 ± 0.04
Tumors	3.67 ± 0.72	3.29 ± 0.64	2.57 ± 0.39	3.04 ± 1.01	3.66 ± 0.62	3.70 ± 0.52	2.71 ± 0.34	3.98 ± 2.16
Excretion	23.82 ± 3.23	25.40 ± 3.08	34.57 ± 2.41	25.85 ± 4.68	40.22 ± 4.70	56.54 ± 1.75	56.44 ± 4.30	48.90 ± 1.10
	72 h p.i.				**144 h p.i.**			
Blood	5.15 ± 0.86	1.85 ± 0.35	1.75 ± 0.47	2.36 ± 0.47	2.35 ± 0.43	0.53 ± 0.19	0.68 ± 0.25	0.78 ± 0.30
Heart	3.60 ± 1.06	2.05 ± 0.43	1.22 ± 0.16	1.49 ± 0.39	2.79 ± 1.38	1.24 ± 0.36	0.88 ± 0.20	1.06 ± 0.34
Lung	3.24 ± 0.43	1.33 ± 0.20	1.21 ± 0.36	1.44 ± 0.22	1.89 ± 0.33	0.74 ± 0.22	0.50 ± 0.26	0.81 ± 0.19
Liver	5.29 ± 1.17	2.46 ± 0.30	2.83 ± 0.56	2.96 ± 0.47	5.13 ± 0.64	1.40 ± 0.33	1. 16 ± 0.19	1.48 ± 0.34
Pancreas	3.10 ± 1.70	1.02 ± 0.43	0.92 ± 0.13	0.84 ± 0.30	1.71 ± 0.56	0.75 ± 0.62	0. 41 ± 0.21	0.88 ± 0.25
Stomach	0.82 ± 0.33	0.52 ± 0.23	0.32 ± 0.07	0.29 ± 0.10	0.48 ± 0.24	0.17 ± 0.06	0.14 ± 0.07	0.24 ± 0.04
Spleen	8.22 ± 2.63	2.72 ± 0.72	3.00 ± 1.78	2.70 ± 0.69	8.27 ± 1.91	3.25 ± 0.86	3. 43 ± 1.46	3.68 ± 1.18
Small Int.	0.59 ± 0.15	0.57 ± 0.12	0.45 ± 0.05	0.62 ± 0.15	0.55 ± 0.19	0.12 ± 0.04	0.18 ± 0.07	0.29 ± 0.04
Large	1.15 ± 0.12	0.58 ± 0.09	0.63 ± 0.11	0.90 ± 0.53	0.92 ± 0.30	0.29 ± 0.04	0.31 ± 0.10	0.33 ± 0.15
Kidney	2.40 ± 0.70	1.45 ± 0.30	1.45 ± 0.36	1.44 ± 0.18	1.95 ± 0.36	0.83 ± 0.20	0.91 ± 0.18	1.03 ± 0.07
Muscle	1.57 ± 0.59	0.85 ± 0.48	0.81 ± 0.32	1.10 ± 0.29	1.21 ± 0.39	0.41 ± 0.21	0.46 ± 0.24	0.64 ± 0.16
Bone	1.88 ± 0.82	1.45 ± 0.68	0.49 ± 0.21	0.78 ± 0.14	1.30 ± 0.42	0.48 ± 0.27	0.48 ± 0.33	0.83 ± 0.24
Brain	0.30 ± 0.04	0.32 ± 0.35	0.07 ± 0.05	0.08 ± 0.02	0.20 ± 0.07	0.06 ± 0.04	0.07 ± 0.09	0.09 ± 0.09
Tumors	5.00 ± 1.40	3.28 ± 0.74	2.38 ± 0.59	2.81 ± 0.52	3.21 ± 0.68	2.61 ± 0.93	1.49 ± 0.31	1.68 ± 0.43
Excretion	51.84 ± 2.65	72.12 ± 1.28	75.70 ± 1.35	68.96 ± 3.13	55.65 ± 2.26	83.29 ± 1.24	87.93 ± 1.49	84.10 ±0.82

Table 3.4: Tumor to non-target organ ratios of ^{177}Lu- labeled CSCs in HPAC tumor bearing mice. N=5 at each time-point. Data are represented as mean ± SD.

T/NT Ratios	^{177}Lu-0	^{177}Lu-1	^{177}Lu-2	^{177}Lu-3	^{177}Lu-0	^{177}Lu-1	^{177}Lu-2	^{177}Lu-3
	4 h p.i.				**24 h p.i.**			
Blood	0.19 ± 0.10	0.19 ± 0.02	0.16 ± 0.03	0.15 ± 0.06	0.33 ± 0.05	0.65 ± 0.12	0.41 ± 0.09	0.44 ± 0.17
Liver	0.74 ± 0.12	0.79 ± 0.08	0.60 ± 0.06	0.61 ± 0.22	0.79 ± 0.18	1.11 ± 0.16	0.65 ± 0.08	0.81 ± 0.31
Spleen	1.13 ± 0.35	1.23 ± 0.42	0.73 ± 0.32	0.86 ± 0.22	0.49 ± 0.12	1.26 ± 0.44	0.70 ± 0.32	0.80 ± 0.32
Kidney	0.72 ± 0.19	0.68 ± 0.19	0.69 ± 0.14	0.66 ± 0.17	1.32 ± 0.43	1.59 ± 0.28	1.06 ± 0.16	1.39 ± 0.84
	72 h p.i.				**144 h p.i.**			
Blood	0.98 ± 0.17	1.83 ± 0.39	1.46 ± 0.53	1.25 ± 0.41	1.41 ± 0.45	5.49 ± 2.32	2.47 ± 1.09	2.36 ± 0.87
Liver	0.96 ± 0.18	1.35 ± 0.26	0.84 ± 0.15	0.96 ± 0.12	0.63 ± 0.13	1.92 ± 0.68	1.31 ± 0.28	1.14 ± 0.17
Spleen	0.66 ± 0.22	1.28 ± 0.38	0.90 ± 0.28	1.08 ± 0.26	0.40 ± 0.08	0.82 ± 0.27	0.47 ± 0.11	0.48 ± 0.15
Kidney	2.14 ± 0.39	2.34 ± 0.55	1.67 ± 0.32	1.97 ± 0.36	1.69 ± 0.45	3.31 ± 1.65	1.67 ± 0.32	1.63 ± 0.35

As with most nanomedicine platforms, the ^{177}Lu-CSCs exhibited liver and spleen retention as a result of MPS driven sequestration [161]. The liver and spleen uptake of the non-cleavable control, ^{177}Lu-CSC0, plateaued by 24 h post-injection with retention values of 4.74 ± 0.65 and 7.79 ± 1.47 %ID/g, respectively. The retention of ^{177}Lu-CSC0 associated radioactivity in the liver and spleen remained essentially constant throughout the remaining time points investigated. As a result of the incorporation of the CSLs, the ^{177}Lu-CSC1-3 demonstrated substantially lower levels of long-term retention in comparison to the control. Significant differences ($p < 0.05$) in the spleen retention of the ^{177}Lu-CSC1-3 versus the ^{177}Lu-CSC0 were observed by 24 h post-administration. By 72 h p.i., both spleen and liver retentions of the ^{177}Lu-CSC1-3 were considerably lower ($p < 0.01$) than control. At our terminal time-point, the liver and spleen retentions of the ^{177}Lu-CSC1-3 were 3.5 - 4.4 and 2.2 - 2.5 fold lower, correspondingly, than the ^{177}Lu-CSC0.

The increased excretion and lower blood, liver and spleen retention profiles of ^{177}Lu-CSC1-3 are undoubtedly linked to the incorporation of the cathepsin S cleavable linker into the HPMA copolymer. The lower liver and spleen retention is likely due primarily to the processing of ^{177}Lu-CSC1-3 by tissue-resident macrophages (e.g., Kupffer cells of the liver) thus resulting in low-molecular weight radiometabolites that are more readily cleared [145, 161]. With respect to blood retention, the ^{177}Lu-CSC1-3 are being cleared from circulation significantly faster than the non-cleavable control. The inclusion of the CSLs into the HPMA copolymers is possibly leading to a markedly higher opsonization and sequestration by the MPS. Such responses have been observed with functionalization of other drug delivery systems, but this seems unlikely given the limited functionalization (< 1 mole%) of the HPMA copolymers used in these experiments [161]. Alternatively, and to us more likely, is the possibility that the ^{177}Lu-CSCs are being

internalized and processed by cellular components of the blood. The human serum studies that were performed suggest that the ^{177}Lu-CSCs are stable in the presence of extracellular serum proteases. However, many drug delivery platforms are known to be taken up by circulating blood monocytes, an APC known to express cathepsin S [162-164]. If this is the case, the ^{177}Lu-CSCs would be expected to be taken up and processed by phagocytic cells in the blood, presumably circulating monocytes. Metabolism of the CSLs by these APCs would lead to the generation of radiometabolites which would likely favor clearance from the processing cell as well as the circulation relative to the non-cleavable ^{177}Lu-CSC0.

The ^{177}Lu-CSCs exhibited substantial accumulation in the HPAC xenograft tumors through the EPR effect [124, 165]. ^{177}Lu-CSC0 demonstrated the highest tumor retention with a peak accumulation of 5.00 ± 1.40 %ID/g at 72 h post-administration. For the ^{177}Lu-CSC1-3, maximal tumor retention for each copolymer was observed by the 24 h time point with values of 3.70 ± 0.52, 2.71 ± 0.34 and 3.98 ± 2.16 %ID/g, respectively. By the 144 h time-point, the tumor retention of ^{177}Lu-CSC1 (2.61 ± 0.93 %ID/g) was statistically identical to the non-cleavable control (3.21 ± 0.68 %ID/g), but was higher than ^{177}Lu-CSC2 ($p < 0.05$) and ^{177}Lu-CSC3 ($p<0.05$) (1.49 ± 0.31 and 1.68 ± 0.43 %ID/g, correspondingly).

The tumor to non-target ratios for selected tissues at 4, 24, 72 and 144 h p.i. are given in Table 3.3. For ^{177}Lu-CSC1, the HPAC tumor retention and non-target clearance properties yielded superior tumor-to-non-target ratios by 24 h p.i. relative to the other ^{177}Lu-CSCs, including the control. The superiority of ^{177}Lu-CSC1, relative to the other copolymers, improved longitudinally with maximal divergence in tumor to non-target

ratios being observed at the 144 h time-point. At this time-point, the tumor-to-liver, spleen and kidney ratios of ^{177}Lu-CSC1 are on average 3.0 ($p<0.01$), 2.1 ($p<0.05$) and 2.0 ($p=0.067$) higher, respectively, than the control.

Evaluation of the biodistribution data for the CSL containing HPMA copolymers reveals some interesting trends with regard to the structure-activity profiles of the ^{177}Lu-CSC1-3 in HPAC tumor and non-target tissues. As described earlier, in vitro assays revealed that the addition of the PEG linker (^{177}Lu-CSC3), the longest (13 atoms) linker, significantly enhanced the cathepsin S cleavage rate relative to ^{177}Lu-CSC1 or ^{177}Lu-CSC2. Given this, one would anticipate that ^{177}Lu-CSC3 would have exhibited the fastest clearance rates from MPS associated non-target tissues. However, in vivo biodistribution studies revealed that the ^{177}Lu-CSC1, null (0 atom) linker, exhibited overall the fastest clearance of radioactivity from the blood, liver and spleen among the CSL containing HPMA copolymers. In fact, at 24 h p.i., the clearance of ^{177}Lu-CSC1 from MPS associated non-target tissues is statistically better ($p < 0.05$) than ^{177}Lu-CSC3. Though, by 72 h and beyond, the clearance of radioactivity in the blood, liver and spleen is statistically identical for all three copolymers. Interestingly, this trend is somewhat reversed with regard to HPAC tumor retention. At 144 h p.i., ^{177}Lu-CSC1 exhibits substantially higher tumor retention relative to both ^{177}Lu-CSC2 and ^{177}Lu-CSC3. At this point, the factors driving these observations remain unclear. Likely, the clearance kinetics of the ^{177}Lu-CSCs relies primarily on a combination of the cleavage kinetics and the vascular and lymphatic efficiencies of the tissue. The inequalities between the non-target, normal tissues and the HPAC tumors with regard to the abundance of cathepsin S expressing APCs and the vasculature and lymphatic systems are likely the driving influences behind these observations. Currently, we are pursuing studies that will

hopefully yield a better understanding of the in vivo cathepsin S cleavage kinetics and clearance mechanisms of the ^{177}Lu-CSCs.

3.3.7 Small Animal SPECT/CT Imaging Studies

For the development of nuclear imaging agents based on nanomedicine platforms, the clinical success of antibody based agents (e.g., ProstaScint® and OncoScint®) can serve as an example, due to the similar pharmacokinetic profiles of the two systems [166, 167]. Similar to many nanomedicine platforms, monoclonal antibodies are large macromolecules that typically don't achieve optimal tumor-to-non-target ratios until days after injection. As a consequence, image acquisitions for clinical imaging agents based on monoclonal antibodies are typically obtained between 2 and 5 days post-injection [166, 168]. For the investigated ^{177}Lu-CSCs, the biodistribution studies suggest that this same time frame would be suitable, if not optimal, for diagnostic imaging.

In order to better evaluate the imaging potential of the ^{177}Lu-CSCs, micro-SPECT/CT studies were performed for ^{177}Lu–CSC0, ^{177}Lu–CSC1 and ^{177}Lu–CSC3 in mice bearing bilateral flank HPAC xenografts. ^{177}Lu –CSC2 was not chosen for μSPECT/CT analysis due to the similarity in its biodistribution profile with ^{177}Lu –CSC3. Whole body images, depicted in Figure 3.6, were collected at 4, 24 and 72 h post-administration. At 4 h p.i., visual inspection of the normalized images revealed substantial accumulation in the abdominal cavity as well as the bladder for all three copolymers. The bladder activity at such an early time-point suggests that the clearance of activity is likely from the copolymer fraction that is below the renal excretion threshold [131]. Visualization of the flank HPAC tumors was limited at 4 h p.i., but became clearly evident by the 24 h time-

point. At 24 h p.i., decreases in the abdominal activity, which includes the liver, were noted for the three copolymers. By the 72 h time-point, all of the investigated ^{177}Lu–CSCs demonstrated considerable uptake/retention in the HPAC tumors. In addition, ^{177}Lu–CSC1 and ^{177}Lu–CSC3 demonstrated superior abdominal clearance relative to the non-cleavable control (^{177}Lu-CSC0). Overall, the SPECT/CT images agree well with the data obtained from the biodistribution study. The substantial retention of ^{177}Lu–CSC1 in the HPAC tumors coupled with the enhanced clearance of activity from the abdominal region suggest that the CSL1 is the most promising linker to move forward with in the development of diagnostic and radiotherapeutic HPMA copolymers.

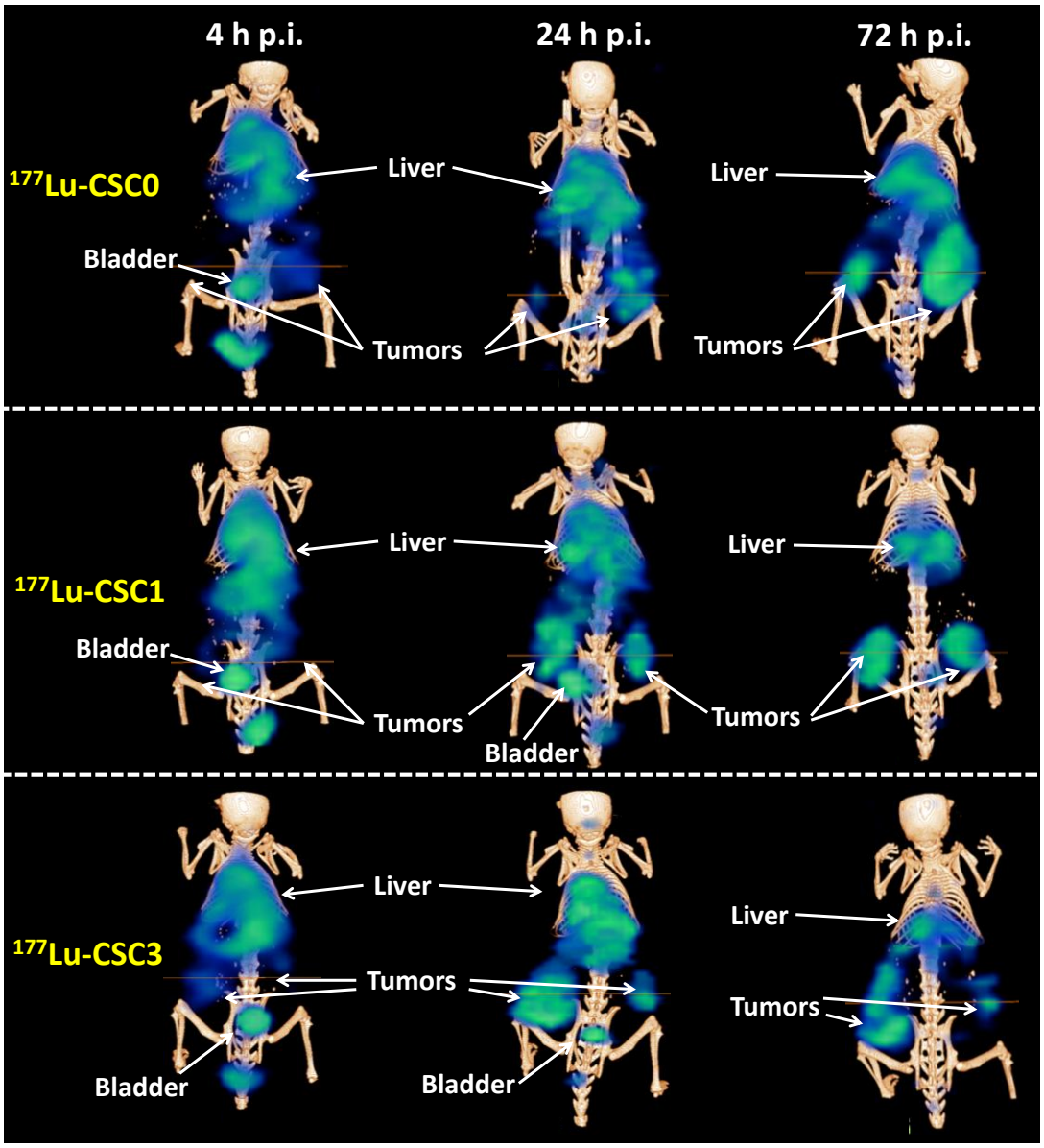

Figure 3.6: Micro-SPECT/CT imaging studies of CSC0, CSC1and CSC3 in HPAC xenograft mice.

3.4 CONCLUSION

In summary, our laboratory is pursuing the development of CSLs that cleave in the presences of cathepsin S, to reduce the non-target accumulation of diagnostic/ radiotherapeutic HPMA copolymers in MPS tissues. To this end, we have evaluated a series of CSLs incorporated into a ^{177}Lu-labeled HMPA copolymer construct with the purpose of understanding the structure activity relationship with regard to the length of the linking groups. In vitro cleavage assays revealed that the longest linking group (13 atoms) demonstrated the highest cathepsin S cleavage kinetics. Additionally, confocal microscopy confirmed the selective uptake of HPMA copolymers in differentiated macrophages and trafficking to the lysosomal cellular compartments. Contrary to in vitro observations, in vivo biodistribution studies revealed that the linking group length in the CSL design did not substantially impact the non-target clearance. However, in the case of HPAC tumor retention, the CSC1 demonstrated significantly higher levels of retention relative to the other CSCs. This gave CSC1 superior tumor-to-non-target ratios as confirmed by longitudinal SPECT/CT imaging studies. Taken together, our results suggest that the dissimilarities in the metabolism and clearance kinetics of the CSL incorporated HPMA copolymers are tissue specific. Our future work will focus on gaining an understanding of the tissue-specific underpinnings influencing CSL metabolism and clearance. Lastly, these results demonstrate that the CSLs can substantially improve the non-target clearance of HPMA copolymers, and likely other nanomedicine platforms, leading to an enhancement in the tumor-to-non-target ratios and ultimately clinical potential.

Chapter 4

Comparison of ^{177}Lu-Labeled Plectin-1 Targeted Peptide (PTP) and PTP-HPMA conjugates for Pancreatic Tumor Targeting

4.1 INTRODUCTION

World-wide, radiotherapy (e.g., external beam, brachytherapy and targeted radionuclide radiotherapy) plays a primary role in the standard of care for many cancer types [169-171]. While the majority of today's clinical radiotherapy centers around external beam, systemic radiotherapy using radionuclide containing carriers that selectively target tumors, through active or passive mechanisms, offer significant advantages and clinical potential [169, 172, 173]. Given that the metastatic spread of cancer, and not the primary tumor, is the main cause of most cancer related deaths; perhaps the greatest advantage of targeted radionuclide therapy (TRT) is the potential to systemically target and eliminate small metastatic lesions that are unobserved clinically due to their size and/or location. Based on this potential, the development of TRT has been an active field of research with reports of radionuclide carriers that range from low molecular weight compounds (e.g., small molecules and peptides) to large macromolecule platforms (e.g., antibodies and nanomedicines) [174-178].

Plectin-1 (Plec1) is a large protein (500kDa) that plays a crucial role in the cytoskeleton in mammalian cells [179]. It is able to bind and crosslink microtubules, actin microfilaments, and intermediate filaments in the cytoplasm. In addition, Plec1 serves as an anchor point between the cytoskeleton and the organelles, nucleus and intracellular

membrane. In normal cells, Plec1 is localized within the cell and as a consequence cannot be targeted using traditional cell-surface targeting approaches. However, for pancreatic ductal adenocarcinoma (PDAC), Plec1 becomes over-expressed on the extracellular surface of the cell thus making it a potential molecular target [37, 180]. Based on a report by Kelly and co-workers, Plec1 is expressed on the extracellular surface of 100% of PDAC samples (n=42), 60% of late-stage, pre-invasive pancreatic intraepithelial neoplasia (PanIN) III samples (n = 15) and 4% of PanIN II samples (n = 26) [180]. Furthermore, normal pancreas (n = 4), chronic pancreatitis (n = 15) and PanIN I (n = 14) samples were negative for Plec1 extracellular surface expression. Given these studies, it appears Plec1 over-expression and extracellular surface localization begins during the pre-invasive PanIN III stage and further increases as the disease progresses into the invasive stage. As a consequence, Plec1 appears to be a potentially valuable molecular target for both diagnostic and therapeutic applications for PDAC.

Recently, a seven amino acid peptide (KTLLPTP) that exhibits submicromolar binding affinity to Plec1 has been reported [37]. As a result of the attractive properties of Plec1, we are interested in developing Plec1-targeted platforms, based on the above peptide targeting vector, for PDAC TRT. Currently, we develop radiopharmaceuticals for oncologic purposes that range in size from small receptor-targeted peptides to nanomedicine platforms [181, 182]. It is well known that the size and molecular weight of targeted radiopharmaceuticals plays a significant role in their in vitro and in vivo biological performance/profile [129, 183]. As our first investigation into the development of Plec1-targeted agents, we were interested in comparing and contrasting the biological profiles of two starkly different Plec1-targeted carriers, specifically one based on a small peptide and one utilizing an N-(2-hydroxypropyl)methacrylamide (HPMA) polymeric

system. To that end, we have synthesized and characterized the two Plec1-targeted agents outlined above. Herein, we describe the in vitro and in vivo properties of these agents using the HPAC human pancreatic cancer cell line.

4.2 MATERIALS AND METHODS

4.2.1 Peptide Synthesis

The plectin-1 targeted peptide (PTP) analogue 1 (KTLLPTPGGG-NH_2 or PTP-NH_2) was synthesized on the rink amide resin using an automated solid phase peptide synthesizer. The resin (0.1 mmole of peptide anchors) was deprotected using 20% piperidine in DMF resulting in the formation of the primary amine. The carboxylic acids of the Fmoc protected amino acids (1 mmol) were activated using COMU and conjugated to the primary amines of the growing peptide on the resin. The resulting peptide was orthogonally deprotected and cleaved from the resin by shaking in a cleavage cocktail consisting of TIS: H_2O: DODT: TFA = 2: 2: 2: 94 for 2 h. The cleaved peptide was subsequently precipitated and washed with ice cold methyl-tert-butyl ether (40 ml×3). Crude peptide was purified using the semi-preparative C12 column with a flow rate of 5.0 mL/min. All HPLC experiments used solvents consisting of H_2O containing 0.1% formic acid (solvent A) and acetonitrile containing 0.1% formic acid (solvent B). The initial gradient of 90% A: 10% B linearly decreased to 70% A: 30% B in 15 minutes. At the end of the run time for all HPLC experiments, the column was flushed with gradient 5% A: 95% B and re-equilibrated to the starting gradient.

The PTP analogue 2 (DO3A-PTP) was conjugated with a DOTA at the N terminal position, and was synthesized on rink amide resin using the peptide synthesizer. The

resin (0.1 mmole) was deprotected using 20% piperidine in DMF resulting in the formation of the primary amine. The carboxylic acids of the Fmoc protected amino acids (1 mmol) were activated by COMU and conjugated to the primary amines of the growing peptide on the resin. DOTA$(tBu)_3$ was added to the N terminus at the final step during the peptide synthesis. The resulting DOTA peptide conjugate was deprotected and cleaved from the resin by stirring in a cleavage cocktail consisting of TIS: H_2O: DODT: TFA = 2: 2: 2: 94 for 2 hours. The cleaved conjugate was precipitated and washed with ice cold methyl-tert-butyl ether (40 ml×3). Crude conjugate was purified using the semi-preparative C12 column with a flow rate of 5.0 mL/min. The initial gradient of 90% A: 10% B linearly decreased to 85% A: 15% B in 15 minutes.

PTP analogues 3 and 4 were synthesized in orthogonally protected forms on the 2-chlorotrityl-Gly-resin using an automated solid phase peptide synthesizer. The resin (0.1 mmole of peptide anchors) was deprotected with 20% piperidine resulting in the formation of the primary amine. The carboxylic acids of the Fmoc protected amino acids (1 mmol) were activated using COMU and conjugated to the primary amines of the growing peptide on the resin. All the protected groups and N terminal Fmoc group were kept intact in the synthesized peptides. The selective cleavage of the protected peptides from the 2-chlorotrityl resin anchor was achieved by reaction with 1% TFA in dry DCM and subsequent filtration. The cleaved peptides were subsequently precipitated and washed thrice using ice cold methyl-tert-butyl ether (40 ml×3). Purification of the peptides was performed using the semi-preparative C12 column with a flow rate of 5.0 mL/min. For peptide 3, the initial gradient of 30% A: 70% B linearly decreased to 5% A: 95% B in 15 minutes. For peptide 4, 40% A: 60% B was linearly decreased to 10 % A: 90 % B in 15 minutes.

The ethylenediamine-DOTA(t-Bu)$_3$ was prepared by first reacting DOTA(t-Bu)$_3$ (1 mmole) with DCC (1.3 mmole) and NHS (1.3 mmole) overnight in 1/1(v/v) ethyl acetate /dioxane solution. The mixture was then washed with 5% sodium bicarbonate, followed by water and brine. The organic layer was dried over $MgSO_4$. The filtrate was concentrated in vacuo, followed by addition of N-Boc ethylenediamine (1.2 mmole). The mixture was stirred overnight. The N-Boc ethylenediamine-DOTA(t-Bu)$_3$ product was peak purified on HPLC using the C12 column with a flow rate of 5.0 mL/min. The initial gradient of 70% A: 30% B linearly decreased to 60% A: 40% B over 15 minutes. The purified N-Boc-ethylenediamine-DOTA(t-Bu)$_3$ 0.52 gram (0.74 mmole) was dissolved in 3 mL of tBuOAc, and 44 µL of 18 M H_2SO4 (1.5 equiv) was added to the solution. The mixture was stirred overnight. The solution was then neutralized with saturated sodium bicarbonate and extracted with ethyl acetate (20 mL×3). The organic layer was dried with MgSO4. The solution was evaporated to dryness and yielded light yellow oil as the desired compound. The yield was 66.5% with MS found: 615.4 ($[M+H]^+$).

The L and D forms of PTP with the C terminal conjugated with a DOTA chelator (peptide 5 or PTP-DO3A and peptide 6 or D-PTP-DO3A) were prepared by reacting the protected peptides 3 and 4 with ethylenediamine-DOTA(t-Bu)$_3$. In general, 3 mg of purified peptide 3 or 4 (2.2 µmole) was reacted with 1.4 mg of ethylenediamine-DOTA(t-Bu)$_3$ in the presence of 2 equiv of EDC and DIPEA in DMF overnight. The crude product was dried in vacuo and treated with a cleavage cocktail consisting of TIS: H_2O: DODT: TFA = 2: 2: 2: 94 for 2 h. The cleaved peptides were precipitated and washed thrice using ice cold methyl-tert-butyl ether (40 mL×3) and then dried in vacuo. After that, 20% piperidine in DMF was used to remove the N-terminal Fmoc group. DMF was removed in vacuo after 20 min deprotection. The final peptides were peak purified by LC-MS on the

C12 column with a flow rate of 5.0 mL/min. The initial gradient of 95% A: 5% B linearly decreased to 70% A: 30% B in 15 minutes.

To prepare the PTP analogues used for “click chemistry”, an Fmoc-D-Lysine-OH containing 5-hexynoic acid at the ε-amine site was synthesized first. To the 5-hexynoic acid (5 mmole) dissolved in DCM was added NHS (6 mmole), EDC.HCl (6 mmole) and triethylamine (6 mmole). The reaction was allowed to proceed at room temperature overnight. The crude product was washed with H_2O and extracted with DCM. The organic layer was dried in vacuo and the crude product was separated by flash chromatography (ethyl acetate/hexane = 1/3). The purified product (2 mmole) was dissolved in DMF, and reacted with Fmoc-D-Lysine-OH.HCl (2 mmole) and triethylamine (2.5 mmole). The mixture was stirred at room temperature overnight. After reaction, the mixture was dried in vacuo and subjected to flash chromatography (MeOH/DCM = 1/9) and the 5-hexynoyl-Fmoc-D-Lysine-OH was obtained in light yellow oil with a 41.6% yield. ^{1}H NMR (DMSO): δ 1.35~1.39 (m, 2H, C*H*$_2$CH$_2$C≡CH), 1.36~1.39 (m, 2H, CH$_2$C*H*$_2$CH$_2$CH$_2$), 1.64~1.67 (m, 4H, C*H*$_2$CH$_2$C*H*$_2$CH$_2$NH), 2.13~2.15 (t, 4H, C*H2*CH$_2$C*H*$_2$ C≡CH), 2.75 (s, 1H, CH$_2$CH$_2$ C≡C*H*), 3.03 (m, 2H, CH$_2$CH$_2$*CH*$_2$NH), 3.90 (m, 1H, C*H*CH$_2$OCO), 4.2 (d, 3H, C*H*$_2$OCO and NHC*H*(CH2)COOH), 7.2~7.6 (m, 8H, benzene), 7.8 (s, 2H, CON*H*). ^{13}C NMR (DMSO): δ 17.6, 23.2, 24.5, 28.9, 30.6, 34.3, 38.4, 46.8, 53.9, 65.8, 71.6, 84.2, 120.2, 127.2, 127.8, 129.6, 140.9, 144.0, 156.3, 171.4, 174.1.

The L and D forms of PTP analogues 7 and 8 were synthesized on a Sieber Amide resin using a solid phase peptide synthesizer. The resin (0.1 mmole of peptide anchors) was deprotected using 20% piperidine resulting in the formation of the primary amine. The carboxylic acids of the Fmoc protected amino acids (1 mmol) were activated using

COMU and conjugated to the primary amines of the growing peptide on the resin. The N terminal Fmoc group was also kept intact in the synthesized peptides. The selective cleavage of the protected peptides from the Sieber Amide resin was achieved by reaction with 1% TFA in dry DCM and subsequent filtration. The cleaved peptides were subsequently precipitated in ice cold water (40 ml). Purification of the peptides was performed using the C12 column with a flow rate of 5.0 mL/min. For both peptides, the initial gradient of 40% A: 60% B linearly decreased to 10% A: 90% B over a 15 minute time period.

The iFluor-647-labeled PTP was prepared through “click chemistry”. The PTP analogue 9 was synthesized on a rink amide resin using a solid phase peptide synthesizer. The resin (0.05 mmole of peptide anchors) was deprotected using 20% piperidine resulting in the formation of the primary amine. The carboxylic acids of the Fmoc protected amino acids (0.5 mmol) were activated using COMU and then conjugated to the primary amines of the growing peptide on the resin. The resulting peptide was orthogonally deprotected and cleaved from the resin by shaking in a cleavage cocktail consisting of TIS: H_2O: DODT: TFA = 2: 2: 2: 94 for 2 h. The cleaved peptides were subsequently precipitated and washed thrice using ice cold methyl-tert-butyl ether (40 ml×3). Purification of the peptide was performed using the C12 column with a flow rate of 5.0 mL/min. The initial gradient of 90% A: 10% B linearly decreased to 80% A: 20% B over a 15 minute time period.

For the preparation of peptide 10, 1 mg of purified peptide 9 (0.86 μmole) was first dissolved with 1 mg of iFluro-647 (0.92 μmole) in MeOH. After that, 0.2 μmole TBTA dissolved in 30 μL DMSO was added to a solution of 0.1 μmole CuSO4 in 100 μL

MeOH/H_2O (v/v, 1/1). Next, 0.5 µmole of L-ascorbic acid dissolved in 100 µL MeOH/H_2O (v/v, 1/1) was slowly added to $CuSO_4$/ TBTA mixture to produce the Cu(I) ion as the catalyst. The catalyst solution was then mixed with peptide 9 and iFluro-647 solution in an ampoule. The ampoule was flame sealed and stirred for 48 h. The iFluro-647-labeled plectin-1 targeted peptide 10 was finally peak purified by LC-MS on the C12 column with a flow rate of 5.0 mL/min. The initial gradient of 90% A: 10% B linearly decreased to 60% A: 40% B over 15 minutes.

4.2.2 Radiolabeling of the Peptides

Each 25 µg sample of peptides 2, 5 and 6 were dissolved in ammonium acetate buffer (0.5 M, 100 µL, pH 5.5). $^{177}LuCl_3$ (1 mCi) was added to the vial containing the conjugate, and the solution was heated for 60 min at 90 °C and allowed to cool to room temperature. To facilitate the separation of radiolabeled peptides from unlabeled peptides on the column, 2-3 mg $CuSO_4$ were added and incubated for 5 min at 90 °C to increase the hydrophobicity of unlabeled conjugates. The resulting radio-conjugate was peak purified using RP-HPLC on a C12 250 × 4.6 mm column and was concentrated using a C18 extraction disk followed by elution with 300 µL ethanol/sterile saline solution (v/v, 3:2) to deliver the radio-conjugate in high purity. The radiolabeled peptides were purified by RP-HPLC with 95% H_2O: 5% acetonitrile linearly decreasing to 70% H_2O: 30% acetonitrile in 15 minutes.

4.2.3 Cell Culture

The HPAC cells were cultured at 37 °C at 5% CO2 in air, as per ATCC protocols, in DMEM/ Ham's F12 medium containing 5% FBS, 1.562 nM EGF, 14.3 mM sodium

bicarbonate, 2.5 mM L-glutamine, 15 mM HEPES and 0.5 mM sodium pyruvate supplemented with 0.35 µM insulin, 0.0625 µM transferrin and 0.11 µM hydrocortisone.

4.2.4 Internalization and Efflux of Radiolabeled Peptides

Internalization studies were performed using HPAC cells in 12 well plates. HPAC cells (~1×10^5) were seeded in each well in DMEM/Ham's F12 media and incubated overnight. The next day, about 100,000 cpm of ^{177}Lu-labeled peptides was added to each well, and cells were incubated for up to 3 h at 37°C. During the incubation, at time-points 15, 45, 90 and 180 min, cells were washed three times with media to remove the free radiolabeled peptide. Surface-bound radioactivity was removed by washing the cells twice with an ice cold acid wash (50 mM glycine-HCl/0.1 M NaCl buffer, pH 2.8). The amount of non-acid washable radioactivity in each well was measured after lysing the cells with 10% NaOH solution.

For efflux studies, HPAC cells (~1×10^5) were incubated in 12 well plates overnight. On the day of the experiment, HPAC cells were first incubated for 2 h at 37°C in the presence of ~100,000 cpm of the ^{177}Lu labeled peptide to reach the plateau amount of cell associated radioactivity. Upon completion of the incubation, cells were washed three times with medium to remove the unbound peptide. Then, fresh medium was put in each well as the reservoir for efflux. After 0, 1, 2 and 4 h, the medium for each time point was harvested for quantitative analysis of ligand efflux. Surface-bound radioactivity was removed by washing the cells twice with an ice cold acid wash (50 mM glycine-HCl/0.1 M NaCl buffer, pH 2.8). The cells were then lysed using a 10 % NaOH solution, and the remaining cell associated radioactivity was quantified. The radioactivity in the effluxed

and cell associated fractions was determined by a gamma counter. The effluxed fraction is expressed as a percentage of the total amount of radioactivity, which is the sum of the effluxed and the remaining fraction in the cell.

4.2.5 In vitro Competitive Binding Study of PTP Analogues

For in vitro binding studies, the half maximal inhibitory concentration (IC_{50}) for the PTP-NH_2 conjugate was determined on the HPAC cell line. In these studies, ^{177}Lu-PTP-DO3A served as the control and PTP-NH_2 as the cold ligand for comparing the relative effectiveness of the conjugates. Briefly, HPAC cells (~5×10^4) were seeded in each well of a 24-well plate and allowed to adhere overnight. The cells were then incubated at 37 °C for 1 h in the presence of radiolabeled ^{177}Lu-PTP-DO3A (~100,000 cpm) and various concentrations (10^{-9}~10^{-4} M) of the PTP-NH_2. At the end of the incubation, the media was removed and cells were washed with cold PBS three times. The cell-associated radioactivity was measured by a gamma counter and the IC_{50} value was determined by nonlinear regression using the one-binding site model of GraphPad Prism 5 (U.S.). The IC_{50} values for peptide 2 and 6 were determined using the same protocol.

4.2.6 Confocal Microscopy

HPAC cells were seeded onto 4-well chambered coverglass units with 5×10^4 cells. The iFluor-647 labeled peptide 10 was dissolved in blank media to 5 μM concentration. The cells were then incubated with the peptide for 4 h in a 37 ºC humidified atmosphere with 5% CO_2. Half an hour before ending the incubation, LysoTracker Red DND-99 and Hoechst 33342 were added in the media to stain the lysosomal compartment and the nuclei respectively. Following incubation, the media was aspirated, and the cells were

washed with PBS to remove free peptides that were not associated with cells prior to microscopic imaging.

4.2.7 Biodistribution of the Radiolabeled PTP Analogue

Biodistribution studies were carried out using age-matched HPAC tumor bearing SCID mice. The animals were inoculated in each flank with 100 µL of a 1:1 ratio of suspended HPAC cells and Matrigel™ to obtain a final concentration of 5 x 10^6 HPAC cells per 100 µL. Upon achieving sufficient tumor size (10-15 mm in diameter), the mice were used for biodistribution studies. The HPAC xenograft mice were injected with a 10 µCi (0.37 MBq) intravenous bolus of the purified ^{177}Lu-PTP-DO3A. The mice were sacrificed and the tissues excised at 1 and 4 h time-points p.i. The blood and excised tissues were weighed, the ^{177}Lu radioactivity was measured using a gamma counter, and the percentage injected dose per gram (%ID/g) was calculated for each tissue.

4.2.8 Metabolic Stability in Human Serum

The stability of peptide 5, PTP-DO3A and ^{177}Lu-PTP-DO3A in human serum was determined. Briefly, 10 µg of PTP-DO3A or 200 µCi (7.4 MBq) of ^{177}Lu-PTP-DO3A was added to 100 µL of human serum and incubated at 37 °C for 15 minutes. After the incubation, 100 µL of an ethanol/ acetonitrile (v/v, 1:1) was added to the serum and the whole mixture was vortexed to help precipitate the serum proteins. The resulting mixture was centrifuged at 12000 x g for 10 min. The supernatant was collected and purged with N_2 gas for 20 minutes to remove the ethanol and acetonitrile. The resulting sample was dissolved in 100 µL water and injected into LC/MS or radio-HPLC for analysis. The

gradient used was 95% H_2O: 5% acetonitrile linearly decreasing to 70% H2O: 30% acetonitrile in 15 minutes.

4.2.9 Synthesis and Characterization of "Click" Reactive HPMA Copolymer

The "click" reactive monomer: N-(2-(2-(2-(2-azidoethoxy)ethoxy)ethoxy)ethyl) methacrylamide (AzMA) was synthesized. First, 1 gram of methacrylic acid (11.63 mmole) was reacted with 1.38 gram of NHS (12 mmole) and 2.3 gram of EDC.HCl (12 mmole) in DCM overnight, the resulting mixture was washed with water, and extracted with ethyl acetate. The organic layer was dried in vacuo. The dried product was monitored over 90% pure on LC-MS so directly used without purification. The dried product (1 gram) was dissolved in DMF followed by addition of 1.2 gram of 11-Azido-3, 6, 9-trioxaundecan-1-amine (5.5 mmole) and triethylamine (11 mmole). The mixture was stirred overnight, then washed with water, and extracted with DCM twice. The organic layer was dried and subjected to silica gel flash chromatography (ethyl acetate/DCM = 9/1) and yielded 0.6 gram of pure monomer-AzMA (40% yield). ^{1}H NMR ($CDCl_3$): δ 1.90 (s, 3H, CH_2=CCH_3), 3.32 (t, 2H, CONHCH_2CH_2), 3.45 (t, 2H, CH_2CH_2-N_3), 3.50~3.70 (t, 12H, CH_2OCH2), 5.67 and 5.28 (s, 2H, CH_2=CCH_3). ^{13}C NMR ($CDCl_3$): δ 18.7, 39.5, 50.8, 70.2, 70.2, 70.2, 70.6, 70.6, 70.7, 119.9, 139.9, 168.8.

The HPMA copolymerization was accomplished using the reversible addition-fragmentation chain transfer polymerization reaction with AIBN as the initiator and CTP as the chain transfer agent. The feed ratio of the polymerization consisted of 78: 19. 6: 2.2: 0.20 mole% HPMA, AzMA, APMA and APMA-FITC, respectively. The polymerization was run at a 1 M total monomer concentration in a dioxane: H_2O (v/v, 2/1)

mixture with a molar ratio of total monomer: chain transfer agent: initiator of 100: 1: 1. Prior to proceeding with the polymerization reaction, the glass ampoule and contents were purged with nitrogen for 20 minutes. Subsequently, the ampoule was flame sealed and allowed to heat at 50 ºC in an oil bath for 48 h. After cooling, the HPMA copolymer was evaporated to dryness, dissolved in methanol and purified by size exclusion chromatography (SEC) using an LH-20 packing material with methanol as the eluent. The conversion rate was 81% as determined by weight after purification. The weight average molecular weight and polymer dispersity of copolymers were determined by the TDA 305 equipped with UV, RI and static light scattering detectors. The static light scattering was calibrated with a PolyCALTM PEO-24K standard. The SEC was carried out on an Asahipak GF-510 HQ column with 40% acetonitrile in PBS as the eluent. The average molecular weights of the copolymers were estimated by OmniSEC 5.1 software.

4.2.10 Synthesis and Characterization of PTP-HPMA Conjugates

The L and D form of PTP analogues - peptide 7 and 8 and were conjugated to HPMA copolymer by copper catalyzed “click chemistry”. Briefly, 100 μmole TBTA dissolved in 30 μL DMSO was first added to 54 μmole $CuSO_4$ in 100 μL (v/v, 1/1) MeOH/H2O. Then 250 μmole L-ascorbic acid in 100 μL of (v/v, 1/1) MeOH/H_2O was slowly added to $CuSO_4$/TBTA mixture to produce the Cu(I) ion as the catalyst. Next, 2 μmole “click” reactive HPMA copolymer dissolved in 100 μL MeOH was mixed with 54 μmole of peptide 7 or 8 (1.2 mole equivalent of azide group in the copolymer) in an ampoule. The reduced Cu+ solution was added slowly to the HPMA and peptide mixture. The ampoule was flame sealed and stirred at 40 ºC over 48 h. After reaction, the mixture was subjected a LH-20 size exclusion chromatography for purification. The polymer peptide conjugates were collected and dialyzed against EtOH/H_2O (v/v, 3/1) for 48 h. The

dialyzed products were dried and reacted with DCC activated DOTA(tBu)$_3$ (2 equiv) in DMF. The final HPMA conjugates were precipitated in cold ether to remove free DOTA. The conjugation efficiency was determined by ninhydrin assay as reported. The conjugates were then deprotected with 20% piperidine in DMF and precipitated in cold ether again. The conjugates were finally treated with a peptide cleavage cocktail. The final polymer peptide conjugates were precipitated again in cold ether and lyophilized for storage.

4.2.11 Internalization Study of PTP-HPMA Conjugates by Flow Cytometry

HPAC cells were seeded in 12-well plates at a density of 1×10^5 cells per well and incubated in media overnight (37 °C, 5% CO_2). Cells were then incubated with two different peptide polymer conjugates (0.2 mg/mL) at 37 °C for the indicated time periods. After incubation, the media was removed. Cells were washed with PBS three times, then harvested and fixed followed by flow cytometry analysis. Each sample analysis involved an evaluation of ~1.0×10^4 cells. The collected data was averaged and reported as the mean fluorescent intensity for each sample.

4.2.12 Radiolabeling and in vitro Evaluation of ^{177}Lu Labeled PTP-HPMA Conjugates

The radiolabeling of the conjugates was accomplished by heating the peptide polymer conjugate (200 µg) dissolved in water at 90 ºC for 1 h in the presence of 14.8 MBq (400 µCi) of $^{177}LuCl_3$. After cooling, the ^{177}Lu-labeled HPMA conjugates were purified by size exclusion chromatography using an LH-20 packing material in methanol. All the purified ^{177}Lu-labeled HPMA conjugates were concentrated using an Amicon Ultra-4 Centrifugal Filter and washed twice with 5 mL of de-ionized water. For

internalization study, HPAC cells were seeded in 12-well plates at a density of 1×10^5 cells per well overnight (37 °C, 5% CO2). Cells were then incubated with different ^{177}Lu-labeled HPMA conjugates (~ 100,000 cpm in each well) at 37 °C for 6 and 24 h. After incubation, the media was removed. Cells were washed with PBS three times, and then lysed with 10% NaOH solution. The internalized amount of radioactivity was measured by the gamma counter. For competitive binding study, HPAC cells (~5×10^4) were seeded in each of 24-well plate overnight and incubated at 37 °C for 1 hour in the presence of ^{177}Lu-PTP-DOTA (~100,000 cpm, 100 µl), with or without 200 µg HPMA-PTP conjugate. At the end of the incubation, the incubation media was removed and cells were washed with media. The cell-associated radioactivity was measured by a gamma counter.

4.3 RESULTS

4.3.1 Design and Synthesis of PTP Analogues

A series of plectin-1 targeted peptide (PTP) analogues were synthesized by solid phase peptide synthesis and characterized by LC/MS. The peptide sequences and mass spectrometric analysis were summarized in Table 4.1. The plectin-1 targeted peptide sequence was initially identified by phase display and consisted of a seven amino acid sequence - KTLLPTP. It has been shown that the C terminal of this peptide could be modified with other compounds without causing the loss of binding affinity to Plec1. In order to investigate whether the N terminal of this peptide is essential for plectin-1 binding, we prepared a PTP analogue with modification at the N terminal. Peptide 2 or DO3A-PTP was synthesized with the N terminal conjugated with a DOTA molecule by adding DOTA in the last step during solid phase peptide synthesis. A GGG linker was inserted between the targeting sequence and the DOTA (Figure 4.1). In order to prepare a C terminal DOTA modified peptide, orthogonally protected peptide 3, consisting of ten

amino acids: KTLLPTPGGG, was synthesized on the 2-chlorotrityl-Gly resin. Peptide 4 had the same peptide sequence and molecular structure with peptide 3 and was prepared following the same strategy with 3 except that all the amino acids used in 4 were the corresponding D forms other than glycine. By evaluating the binding affinity of D-PTP towards plectin-1, we can determine whether the cell-association/binding of the PTP is target-specific or due to any contribution from non-specific binding.

The ethylenediamine(EDA)-DOTA(t-Bu)$_3$ was synthesized and used to modify the C terminal of peptide 3 and 4 with a DOTA molecule. N-Boc-ethylenediamine was firstly reacted with DCC activated DOTA(tBu)$_3$, followed by treatment with dilute H_2SO_4 in tBuOAc solution in order to selectively remove the N-Boc protecting groups. The EDA-DOTA(t-Bu)$_3$ was then conjugated to the C terminal carboxylic acid of peptide 3 and 4 via EDC and NHS coupling. The crude products were not purified but directly subjected to TFA and piperidine treatment to remove the protecting groups. The final desired peptide 5 (PTP-DO3A) and 6 (D-PTP-DO3A) were purified by LC/MS based on the presumed molecular weight in a relatively poor yield. The poor yield might be due to our one-pot conjugation and deprotection method. We might achieve a better yield if we had purified desired products after each reaction.

Table 4.1: MS characterization of plectin-1 targeted peptide analogues. All the D form amino acids were abbreviated in lower case letters. (a, the exact molecular formula of iFluor-647 was unknown. b, corresponding to $[M+2H^+]/2$)

Peptide No.	Sequences	Formula	Mass Observed $[M+H]^+$	RP-HPLC retention time / min	Yield (%)
1	KTLLPTPGGG-NH_2	$C_{42}H_{74}N_{12}O_{12}$	939.33	8.03	34.1
2	DO3A-GGGKTLLPTPG-NH_2	$C_{60}H_{103}N_{17}O_{20}$	1382.39	13.77	43.4
3	Fmoc-KTLLPTPGGG-OH	$C_{70}H_{107}N_{11}O_{17}$	1374.61	6.88	31.5
4	Fmoc-ktllptpGGG-OH	$C_{70}H_{107}N_{11}O_{17}$	1374.61	9.67	30.5
5	KTLLPTPGGG-EDA-DO3A	$C_{60}H_{105}N_{17}O_{19}$	1368.72	9.37	13.3
6	ktllptpGGG-EDA-DO3A	$C_{60}H_{105}N_{17}O_{19}$	1368.61	9.31	15.1
7	Fmoc-KTLLPTPGGG-p(4-F)-k(5-hexynoate)	$C_{91}H_{134}FN_{15}O_{19}$	1761.78	10.77	30.7
8	Fmoc-ktllptpGGG-p(4-F)-k(5-hexynoate)	$C_{91}H_{134}FN_{15}O_{19}$	1761.82	10.21	32.1
9	KTLLPTPGGG-k(5-hexynoate)	$C_{54}H_{92}N_{14}O_{14}$	1161.44	10.93	29.5
10	KTLLPTPGGG-k(5-hexynoate)-iFluor-647	N/A[a]	1120.43[b]	11.88	30.1

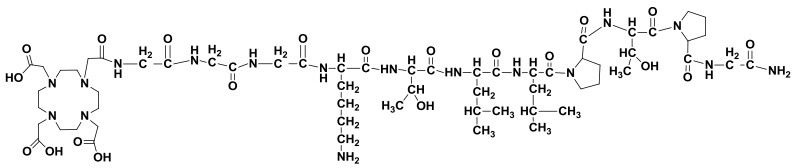

Structure of Peptide 2, DO3A-PTP

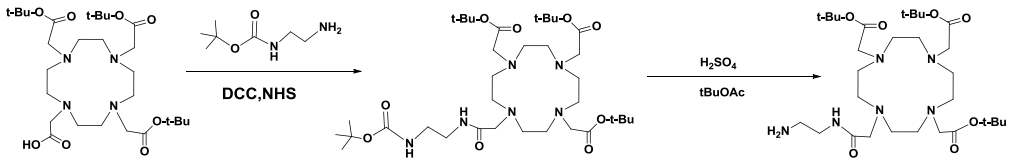

Synthesis of ethylenediamine-DOTA$(tBu)_3$

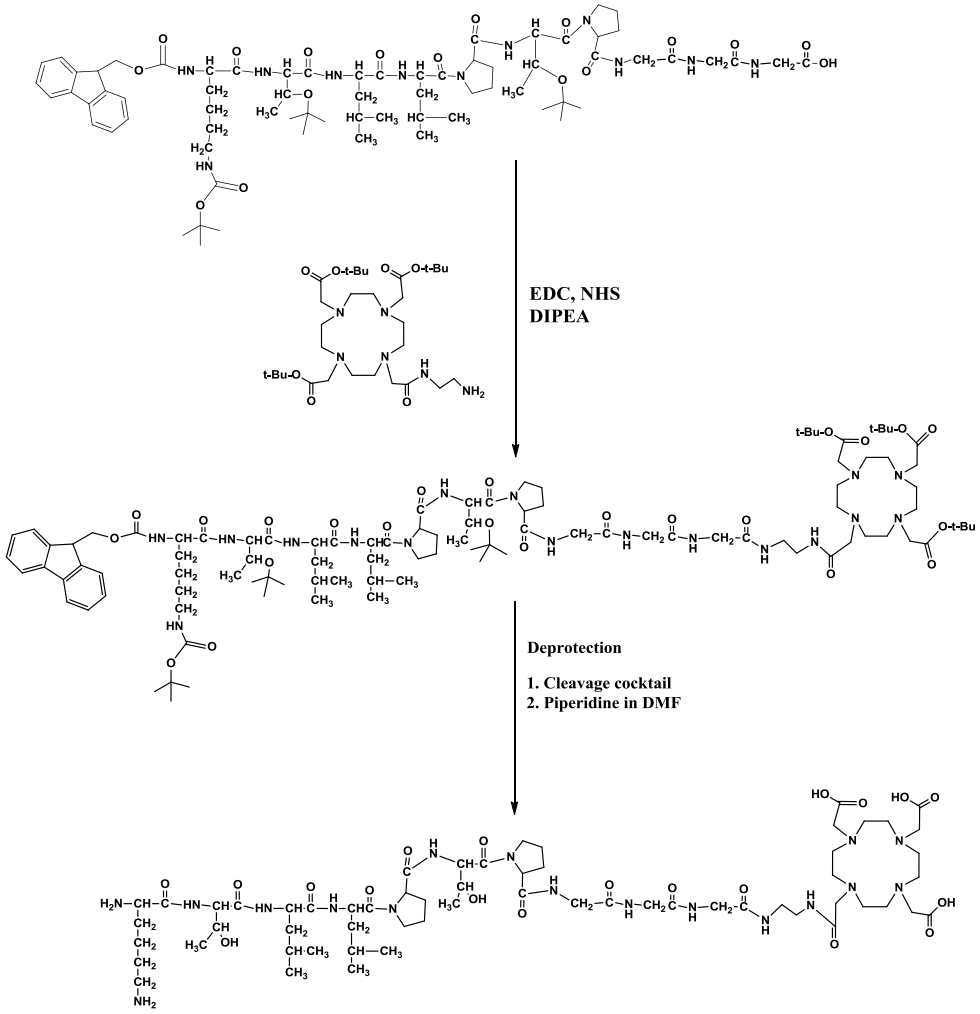

Synthesis of PTP-DO3A

Figure 4.1: Structure of DO3A-PTP conjugate and synthesis for PTP-DO3A conjugate.

We next prepared an amino acid derivative that can be used in peptide synthesis to introduce the alkyne functional group into PTP analogues. Those PTP analogues bearing alkyne groups can be conjugated to azide functionalized compounds through “click chemistry”. The ε-amine of Fmoc-D-lysine was conjugated with a 5-hexnoic acid within two steps (Figure 4.2). The resulting product: 5-hexynoate-Fmoc-D-lysine was then used for the synthesis of peptides 7-10. Peptides 7 and 8 were synthesized in orthogonally protected form on the Sieber Amide resin. An amino acid derivative 4-^{19}F D-phenylalanine was inserted between the GGG linker and the 5-hexynoate-D-lysine and functionalized as a “tag”. Thereby, the amount of peptide conjugated to the copolymer could be easily determined by ^{19}F NMR. Except for glycine, 4-^{19}F D-phenylalanine and 5-hexynoate-D-lysine, all the other amino acids in peptide 7 was in L forms while all the other amino acids in peptide 8 was in D forms. Peptide 8 was used in the following section to prepare a polymer peptide conjugate as a control. Peptide 9 was a PTP analogue with a GGG linker after the targeting sequence, followed by the 5-hexynoate-D-lysine at the C terminal position. Peptide 9 was used to conjugate with a near infrared fluorophore by “click chemistry”.

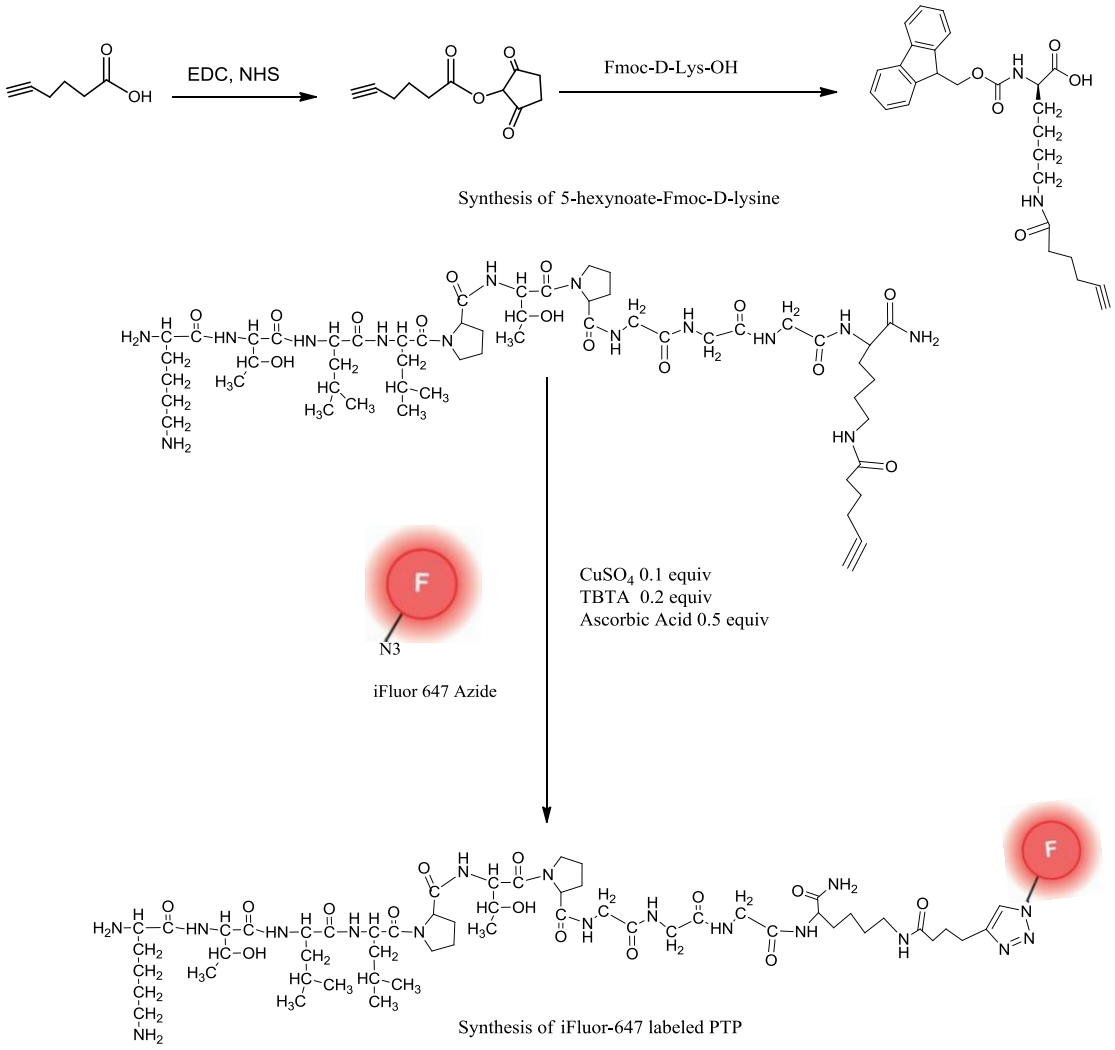

Figure 4.2: Synthesis of 5-hexynoate-Fmoc-D-lysine and iFluor-647-labeled PTP.

The fluorophore labeled PTP analogue 10 was synthesized by copper (I) catalyzed "click chemistry" and was used to investigate the cellular localization of PTP on pancreatic tumor cells. The Cu(I) ion was in-situ generated after reducing $CuSO_4$ with ascorbic acid. TBTA could protect Cu(I) from oxidation and disproportionation, while enhance its catalytic activity. The fluorophore we used is iFluor-647, which has an azide functional group in it with similar excitation/emission spectra as Cy 5.5 but the exact molecular structure was unknown. However, the molecular weight was known to be 1079.1. The desired peptide peak was identified in LC/MS based on the calculated molecular weight and peptide 10 was purified by RP-HPLC. The "click" reaction yield was about 30%, which should be increased by optimizing the reaction conditions. Even though we didn't characterize the excitation/emission property of the collected peptide, the conjugate showed a deep blue color in solution, which confirmed the successful conjugation of the fluorophore to the peptide.

4.3.2 Competitive Binding, Internalization, Efflux Studies of ^{177}Lu PTP Analogues

The binding affinity, internalization and efflux of plectin-1 targeted peptide analogues were investigated on HPAC cell lines. All the peptides were successfully labeled with ^{177}Lu at > 90% efficiency. The non-radiolabeled peptides were labeled with Cu(II) by adding excess amount of $CuSO_4.5H_2O$ (2 mg) to the labeling mixture, which results in better separation from the ^{177}Lu labeled peptide in HPLC. The synthesized cold ligand, KTLLPTPGGG-NH_2(PTP-NH_2) could compete with ^{177}Lu-PTP-DO3A towards plectin-1 binding on HPAC, with a IC_{50} at 1.6 ± 0.2 μM (Figure 4.3 A), which is very close to the reported tetrametric PTP analogue [14]. The ^{177}Lu-labeled PTP-DO3A exhibited very efficient targeting ability in vitro, with a initial 24.49 ± 3.94% of cell associated radioactivity in 15 min, and increased to 46.77 ± 1.36% after 3 h incubation. The acid

washable portion was very low, but increased from 1.64 ± 0.53% at 15 min to 3.72 ± 0.37% at 3 h (Figure 4.3 B). Neither the DO3A-PTP nor the D-PTP-DO3A showed any significant binding toward plectin-1, with IC_{50} > 200 μM. Neither exhibited any uptake to pancreatic cancer cells, which implys that N terminal of KTLLPTP is more essential for plectin-1 binding and cell-association/binding of the PTP is target-specific but not due to any contribution from non-specific binding. In our experiments, we also found that ^{177}Lu-PTP-DO3A did not exhibit any binding toward plectin-1 when we performed the competitive binding assay at 4 ºC, the reason is still unknown. The IC_{50} value was obtained at 37 ºC instead of 4 ºC. The efflux study was initiated after 1 h incubation of ^{177}Lu-PTP-DO3A with HPACs. The 1 h incubation time was chosen because based on the internalization study, the uptake level reached the plateau as soon as in 45 min. The effluxed amount of cell associated activity increased from 8.47 ± 0.50% at 1 h to 29.63 ± 0.91% at 4 h (Figure 4.3 C).

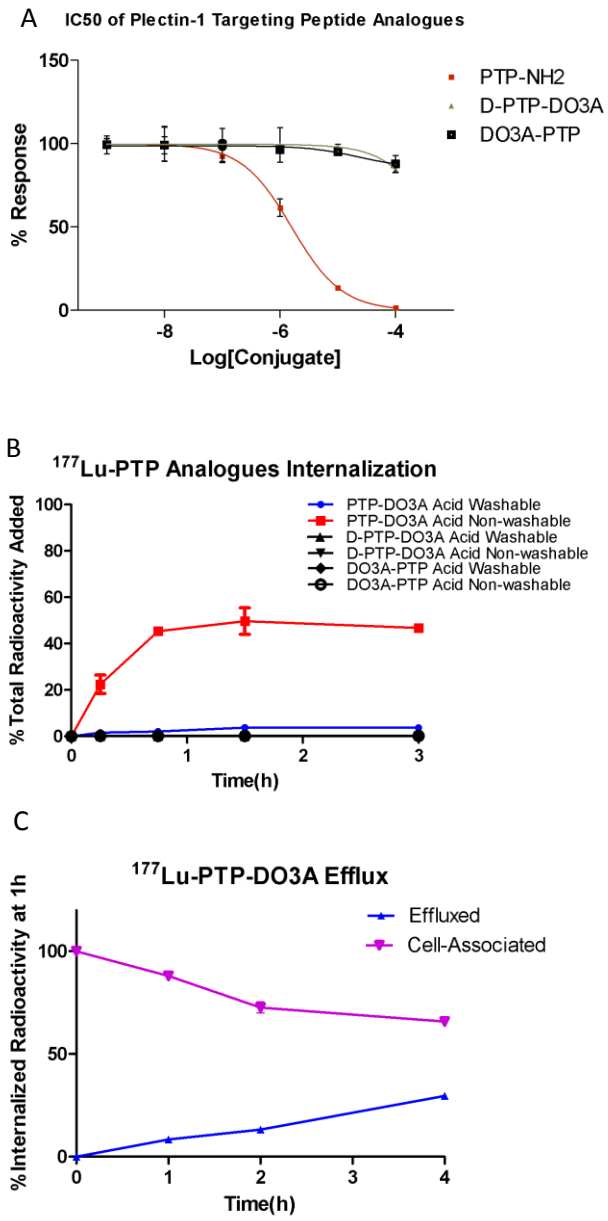

Figure 4.3: Competitive binding, internalization/efflux studies of ^{177}Lu-labeled PTP analogues in HPAC cells. A, the N terminal modified analogue DO3A-PTP showed more than 100 times lower binding ability towards plectin-1 as compared to the C-terminal modified analogue PTP-DO3A. B and C, the ^{177}Lu-PTP-DO3A exhibited the highest uptake and sustained efflux in the study period.

4.3.3 Confocal Microscopy Study of iFluor-647 labeled PTP analogue

The cellular localization of plectin-1 targeted peptide on HPAC human pancreatic cancer cell was determined using the iFluor-647-labeled peptide with confocal microscopy. Single and triple cell staining studies were performed. In the triple staining study, the lysosome compartments were labeled with the Lysotracker (red) and the nuclei were stained with Hoeschst 33342 (blue). After 4 h incubation, the majority of the peptide was found on the HPAC cell membrane (Figure 4 A, red and 4 B, pink) instead of inside the lysosome compartment (Figure 4 B, red). Even though the internalization study showed that most cell-associated radioactivity was acid non-washable, the peptides were not internalized after 3~4 h.

A B

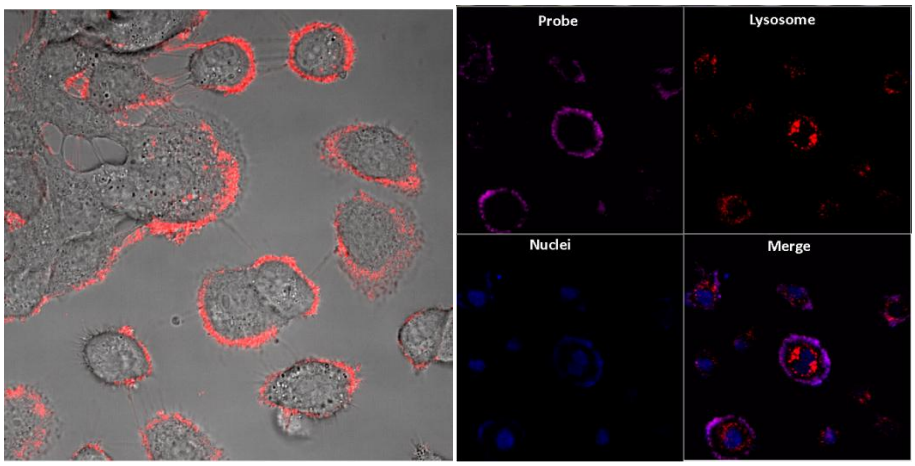

Figure 4.4: Cell trafficking of iFluor-647-labeled PTP in HPAC cells under confocal microscopy. A, overlay of bright field image and near infrared image of the localization of iFluor-647-labeled PTP in HPAC; B, iFluor-647-labeled PTP staining (pink), lysosome staining (red) and nuclei staining (blue) of HPAC cells and the merge picture.

4.3.4 Biodistribution Study of ^{177}Lu-labeled PTP Analogue

The in vivo targeting efficacy for pancreatic tumor was evaluated in an HPAC xenograft mice model by intravenous injection of ^{177}Lu-PTP-DO3A. The radioactivity was eliminated quickly, mainly throughout the renal system. At 1 h p.i., even though the absolute value was low, tumor sites still had the second highest radioactivity level (ID%/g of tumor vs spleen, $p = 0.70$) among all tissues (Table 4.2 and Figure 4.5). The tumor to muscle ratio was 3.45 ± 1.66. At 4 h p.i., the radioactivity was absent in all tissues except the kidney (2.50 ± 0.30 % ID/g).

Table 4.2: Biodistribution (ID%/g) of ^{177}Lu-PTP-DO3A in HPAC xenograft mice at 1 and 4 h p.i. N=3 at each time-point.

Tissue	1 hour	4 hour
blood	0.46 ± 0.05	0.09 ± 0.10
heart	0.26 ± 0.08	0.04 ± 0.06
lung	0.38 ± 0.04	0.05 ± 0.06
liver	0.37 ± 0.18	0.19 ± 0.05
pancreas	0.16 ± 0.06	0.05 ± 0.06
stomach	0.08 ± 0.01	0.01 ± 0.02
spleen	0.89 ± 0.67	0.06 ± 0.07
small int.	0.47 ± 0.36	0.04 ± 0.01
large int.	0.31 ± 0.14	0.20 ± 0.01
kidney	4.33 ± 1.59	2.50 ± 0.30
tumor	0.72 ± 0.28	0.08 ± 0.03
muscle	0.32 ± 0.33	0.01 ± 0.01
bone	0.28 ± 0.40	0.06 ± 0.08
brain	0.04 ± 0.02	0.01 ± 0.01

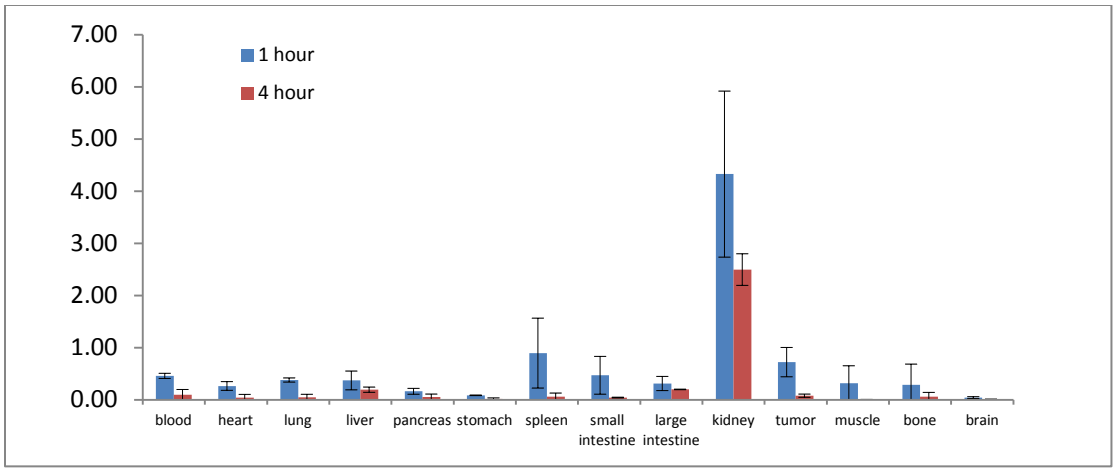

Figure 4.5: Biodistribution (ID%/g) of ^{177}Lu-PTP-DO3A in HPAC xenograft mice at 1 and 4 h p.i. N=3 at each time-point. Tumor sites had the second highest accumulation at 1 h but were quickly decreased at 4 h.

4.3.5 Metabolic Stability of Plectin-1 Targeted Peptide

The low tumor uptake in vivo was considered due to the instability of the ^{177}Lu-PTP-DO3A in the blood. In vitro serum stability study was performed to investigate the stability and metabolite of the radiolabeled and non-radiolabeled plectin-1 targeted peptides. The ^{177}Lu-PTP-DO3A was degraded very fast in serum, generating one major metabolite and two other metabolites after 15 min incubation with human serum (Figure 4.6 A&B). The LC-MS analysis was used to investigate the metabolites of non labeled PTP-DO3A in human serum. We found that the major metabolite was the product from the N-terminal D-lysine residual cleavage (peak 4, calculated 620.84 / found 620.81). Two other metabolites were identified where cleavage sites were between the ^{3}L--^{4}L residual (peak 1, calculated 513.77 / found 513.75) and ^{2}T--^{3}L residual (peak 2, calculated 570.31 / found 570.29) (Figure 4.6 C&D).

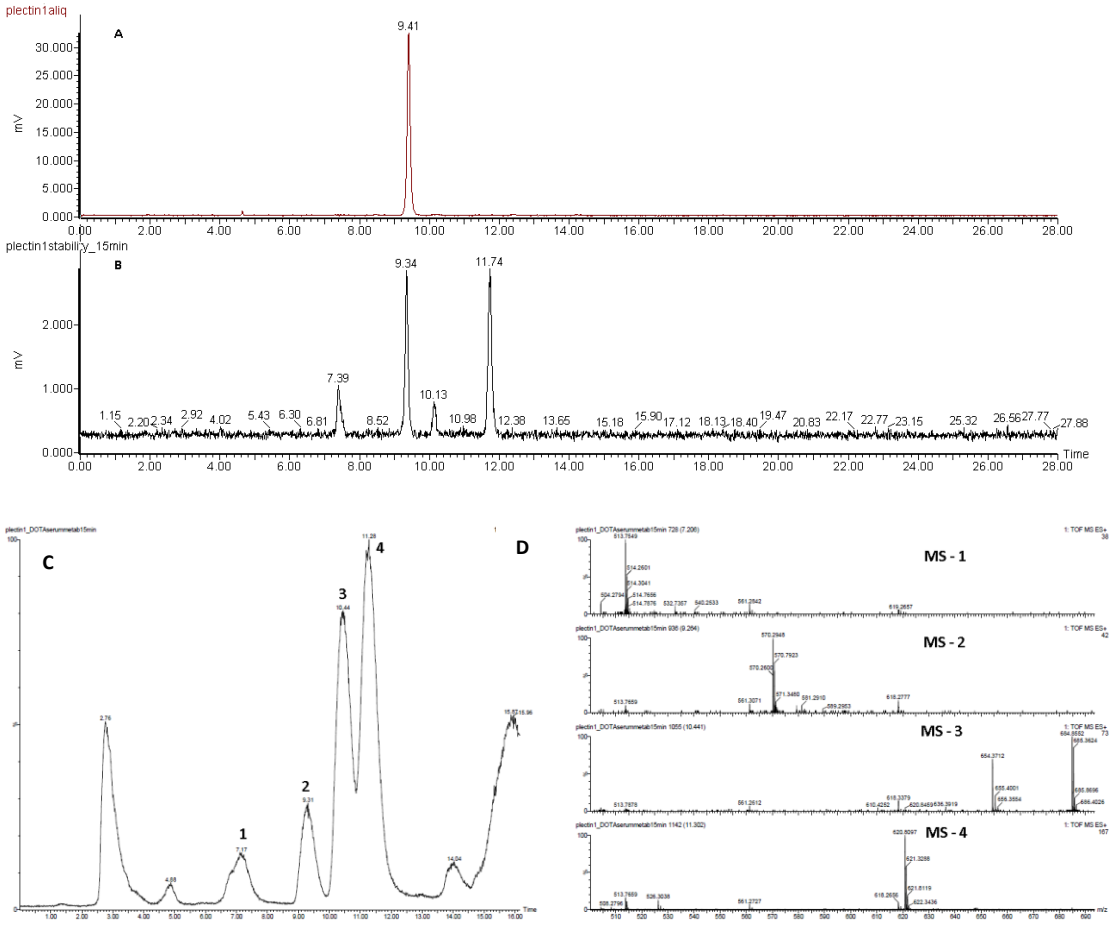

Figure 4.6: Metabolism of plectin-1 targeted peptide in human serum. A, Radio-HPLC signal of ^{177}Lu-PTP-DO3A before incubation; B, radio-HPLC signal of the degradants of ^{177}Lu-PTP-DO3A after 15 min incubation; C, total ion chromatography of PTP-DO3A after 15 min incubation; D, the corresponding mass-spectra of peak 1-4.

4.3.6 Synthesis and Characterization of PTP-HPMA Conjugates

Click reaction has shown improved conjugation efficiency as compared to many other bio-conjugation methods. In order to prepare the “click” reactive HPMA copolymer, we first developed a monomer bearing the azide functional group. The monomer AzMA was synthesized by reacting methacrylic acid with the 11-Azido-3, 6, 9-trioxaundecan-1-amine (Figure 4.7). The PEG3 linker between the azide group and the HPMA backbone was considered to help increase the conjugation efficiency by decreasing the steric hindrance. HPMA copolymers containing APMA and AzMA were prepared by RAFT polymerization using CTP as the chain transfer agent and AIBN as initiator. Dioxane and water mixture (v/v, 2/1) was used to solubilize all the monomer content. The copolymer had a molecular weight 25,610 Da and the PDI 1.2 based on the static light scattering measurement. The mole content of HPMA, APMA and AzMA unit in the copolymer was determined by ^{1}H NMR (Figure 4.8). The copolymer had 14.5 mole% and AzMA 1.2 mole% APMA, which corresponded to 132 molecules of HPMA unit, 23 molecules of AzMA unit and 2 molecule of APMA on average in each copolymer backbone. The PTP analogues 7 and 8 were successfully conjugated to the HPMA copolymer by “click chemistry”, as confirmed by the ^{19}F NMR. Initially we tried to use D-propargylglycine, which was commercially available, to introduce the alkyne group into the peptide but the resulting peptide did not conjugate well with the polymer, possibly due to steric restriction. We switched to the 5-hexynoate-D-lysine as it had longer distance between the alkyne group and the amino acid back bone, which should help increase the conjugation efficiency. We also optimized the “click chemistry” reaction conditions to increase the conjugation efficiency. The amount of $CuSO_4$ we used was one molar equivalent to the alkyne group. This is a much larger quantity as compared to amounts other researchers reported (normally between 0.01 to 0.1 mole equivalent). The amount

of peptide conjugated to the HPMA copolymer was determined by quantitative ^{19}F NMR. Known amounts of the 4-fluoro-3-nitrobenzotrifluoride were added as the internal standard. The peptide content was calculated out based on the ^{19}F NMR integral area ratio between the -CF3 peak (0 ppm) from the internal standard and the –PhF peak (56.7 ppm) from the D-phenylalanine residual (4-F). We obtained a high conjugation yield with 10.4 mole% peptide 7 and 8.9 mole% peptide 8 conjugated to the HPMA copolymer, corresponding to 71.1% and 60.8% conjugation efficiency. The average number of peptides in the copolymer was about 16 for peptide 7 and 14 for peptide 8. The conjugated peptides in the copolymer were subsequently deprotected by piperidine and then TFA cocktail, after conjugation with DOTA$(tBu)_3$. Ninhydrin assays showed that 23% and 25% of APMA in the copolymers were linked with DOTA$(tBu)_3$, respectively.

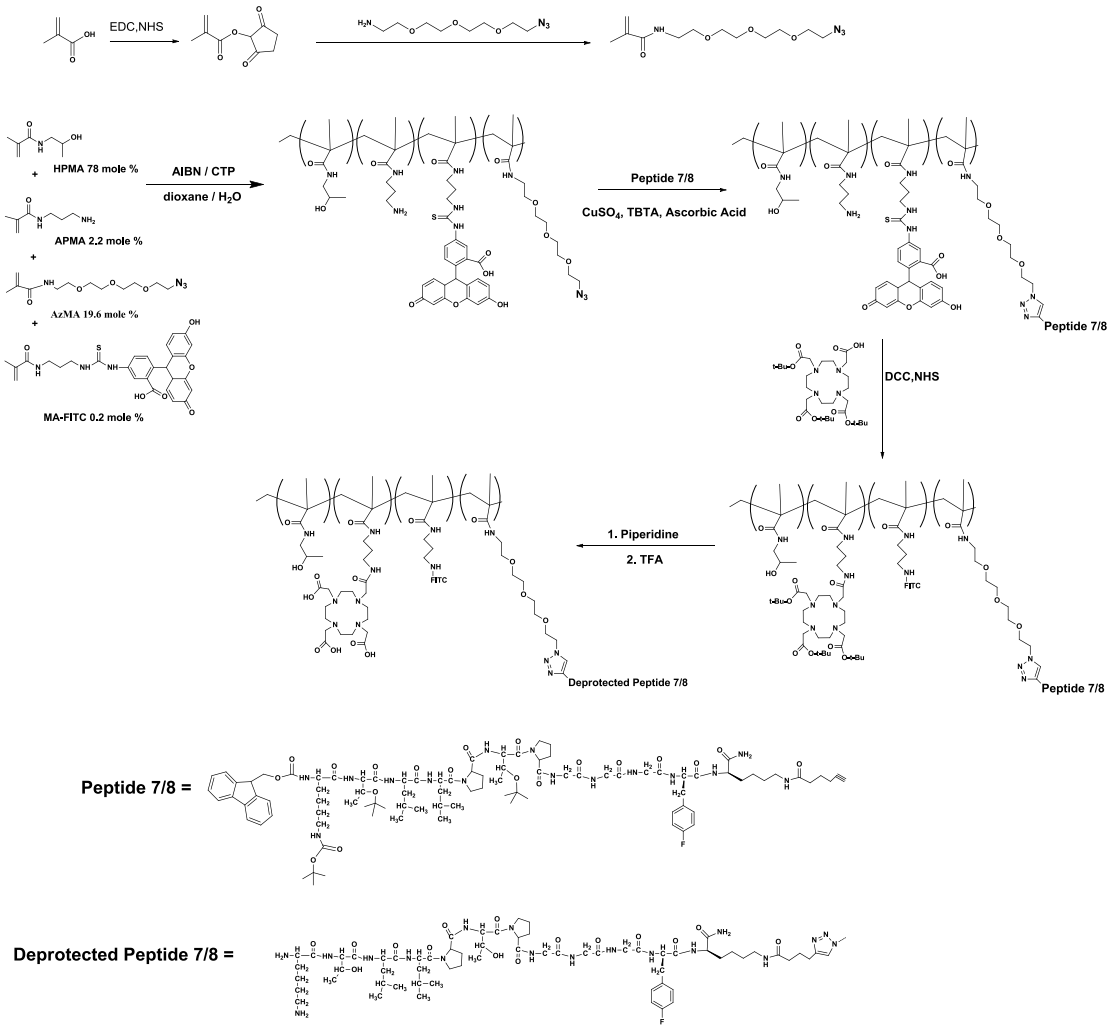

Figure 4.7: Synthesis of HPMA-AzMA-APMA copolymer and plectin-1 targeted peptide conjugated HPMA copolymers (PTP-HPMA) and the control (D-PTP-HPMA).

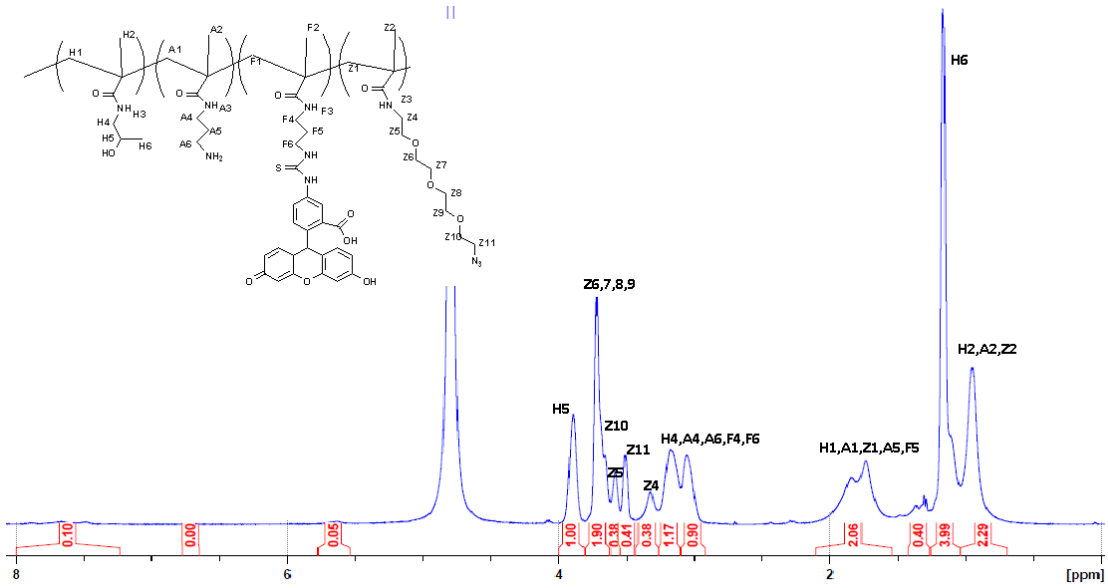

Figure 4.8: ^{1}H NMR spectra of “click” reactive HPMA-AzMA-APMA copolymer in D_2O solvent. The corresponding position of each hydrogen atom is denoted in the spectra.

4.3.7 Internalization Study of PTP-HPMA conjugates

The efficacy of the plectin-1 targeted peptide conjugated HPMA copolymer (PTP-HPMA) and the corresponding control conjugate (D-PTP-HPMA) for pancreatic tumor targeting was evaluated by flow cytometry (Figure 4.9). At 200 μg/ml concentration, the D-PTP-HPMA conjugate didn't show any uptake from 6 to 24 h. At 6 h, there wasn't any uptake difference between the PTP-HPMA conjugate and the D-PTP-HPMA conjugate. The PTP-HPMA conjugate had a significantly higher uptake than the D-PTP-HPMA conjugate at 24 h. However, such increase didn't seem to be mediated by plectin-1, as an excess amount of free PTP-NH_2 couldn't block the uptake after a 24 h co-incubation.

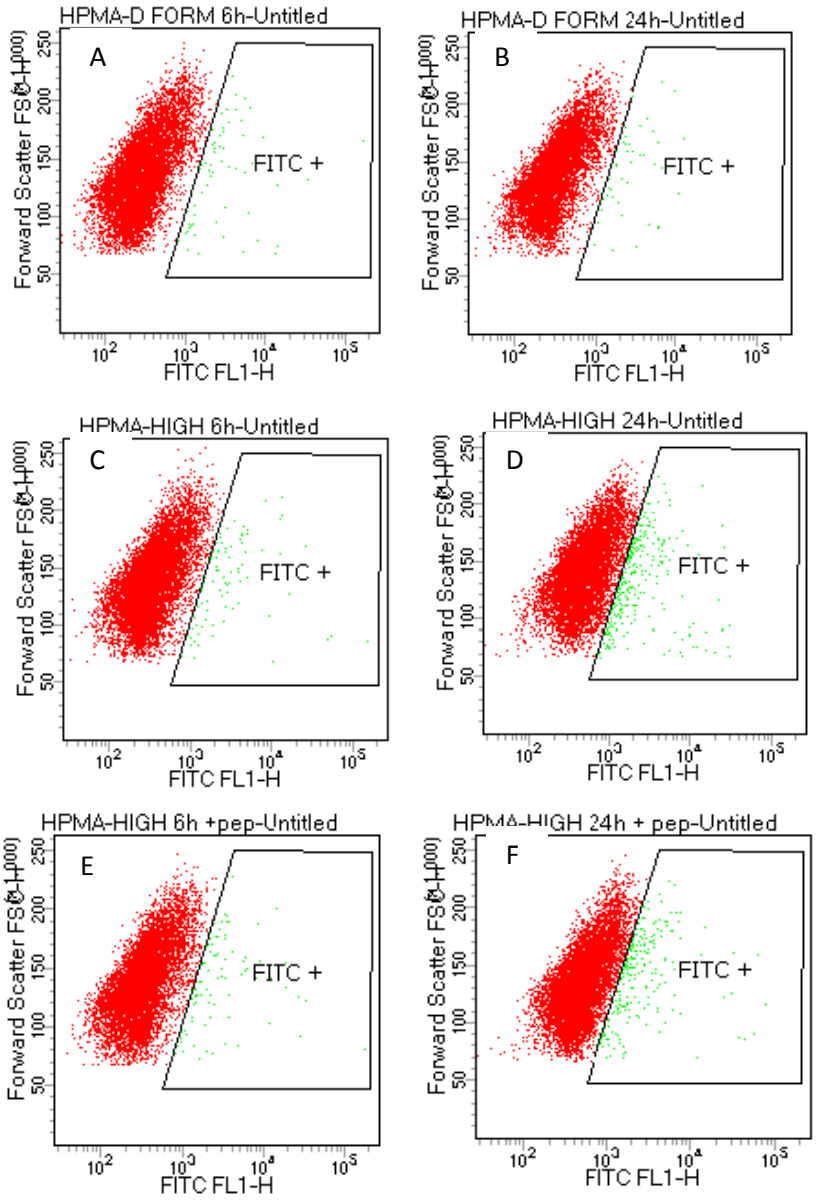

Figure 4.9: Analysis of FITC-labeled peptide-HPMA conjugate cell uptake at 6 and 24 h. A and B, uptake of D-PTP-HPMA conjugate at 6 and 24 h; C and D, uptake of PTP-HPMA conjugate at 6 and 24 h; E and F, uptake of PTP-HPMA conjugate after co-incubation with 200 μg/ml PTP-NH_2 at 6 and 24 h.

The internalization of PTP-HPMA conjugate in pancreatic tumor cells was also investigated using radiolabeled conjugates. Both conjugates could be labeled with ^{177}Lu easily with efficiency > 80%. But the ^{177}Lu-labeled, PTP-HPMA copolymer had very minimal amounts of cell uptake, even though slightly higher than the ^{177}Lu-labeled, D-PTP-HPMA copolymer at 6 h, but their cellular uptake was not significantly different at 24 h (Figure 10). An excess amount of free PTP-NH_2 again did not affect the overall internalization of ^{177}Lu-PTP-HPMA at 6 or 24 h. Overall, the ^{177}Lu-labeled, PTP-HPMA exhibited much lower cell uptake as compared to the free peptide ^{177}Lu-PTP-DO3A.

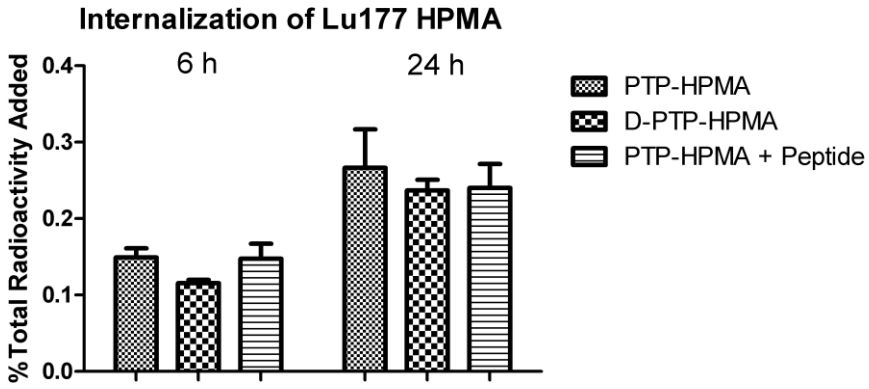

Figure 4.10: Internalization of ^{177}Lu-PTP-HPMA conjugates in HPAC cells at 6 and 24 h. The uptake of ^{177}Lu-PTP-HPMA conjugate was slightly higher at 6 h but not significantly different from ^{177}Lu-PTP-HPMA conjugate at 24 h.

The interaction between PTP-HPMA conjugate and the plectin-1 was also examined by competitive binding study. However, even with 200 µg/ml of PTP-HPMA conjugate present in the media, the uptake of ^{177}Lu-PTP-DO3A wasn't decreased. This, in another aspect, showed the conjugate didn't exhibit any plectin-1 binding capability.

4.4 DISCUSSION

There is an urgent need to develop better diagnostic agents for pancreatic cancer detection and staging [184, 185]. Recent reports by Kelly and colleagues identify plectin-1 as a potential biomarker for PDAC [14]. Plectin-1 is a cytoskeleton protein that is ubiquitously expressed in cells, but is normally constrained to the intracellular compartment. However, in the case of PDAC, plectin-1 becomes aberrantly expressed on the extracellular surface. Plectin-1 appears to be a potentially valuable molecular target for diagnostic applications for PDAC. Herein, we prepared two different plectin-1 targeted carriers, the small peptide and the peptide HPMA conjugates and radiolabeled these carriers with ^{177}Lu. We evaluated the in vitro and in vivo properties of these carriers using the HPAC human pancreatic cancer cell line.

Based on existing knowledge, the C-terminus of the PTP can be modified without substantial loss in binding affinity to plectin-1. However, based on our results from incorporating a N-terminal DOTA (peptide 2), the N-terminus was found to be more sensitive to modification, greater than a 100 fold decrease in binding affinity relative to C-terminally modified PTP-DO3A (peptide 5), thus suggesting that the N-terminal amino acids are crucial for activity. In addition to modification of the termini of the peptide, we investigated the D-form analogue of the PTP (D-PTP-DO3A, Peptide 6) to determine

what role the physiochemical properties of the targeting vector plays in cell-association activity. The D-form of the PTP (^{177}Lu-D-PTP-DO3A) demonstrated negligible cell-association toward the HPAC cells and lacked the ability to competitively inhibit the binding of the L-form of the PTP to plectin-1. These studies suggests that the cell-association/binding of the PTP is target-specific and not due to any contribution from non-specific binding.

Using a fluorescently labeled PTP analogue (Peptide 10), the cell trafficking of the PTP was investigated in the HPAC cell line. At the 4 h time-point, it was found that the PTP localizes on the cell membrane with little evidence of internalization, which is consistent with reported findings. This data was important for the subsequent interpretation of the internalization and efflux data of the PTP. The C-terminal modified PTP (^{177}Lu-PTP-DO3A) exhibited a high percentage of cell associated radioactivity in as little as 15 min and plateaued after 45 min. Attempts to distinguish internalized radioactivity from surface-bound, using was acid buffer washes, initially led us to believe that the radio-conjugate was being internalized. However, based on the confocal studies, it seems that the standard acid buffer wash is unable to remove radiolabeled PTP from the cell surface. We are currently working on developing more rigorous surface removal buffers to adequately distinguish surface-bound from internalized radioactivity. One alternative explanation for this observation is the possibility that the fluorescently labeled peptide (peptide 10) has markedly different internalization properties relative to ^{177}Lu-PTP-DO3A. However, this seems unlikely since distance of the chelator/fluorophore from the pharmacophore is quite large, relative to other receptor-targeted peptides, and would not be expected to generate such a contrasting phenomenon in terms of internalization profiles.

Encouraged by the in vitro results, we investigated ^{177}Lu-PTP-DO3A in an HPAC xenograft mouse model. At the 1 h time-point, the radio-conjugate cleared rapidly from the blood and other non-target tissues and was excreted from the mice largely by the renal system. Due to this excretion profile, the kidneys were found to have the highest radioactivity retention with 4.33 ± 1.59 %ID/g and 2.50 ± 0.30 %ID/g at the 1 and 4 h post-injection time-points, respectively. While the HPAC tumors sites had the second highest uptake among all tissues, the tumor uptake was only 0.72 ± 0.28 ID/g at 1 h and had essentially cleared all remaining activity by the 4 h time-point. These results are disappointing, particularly in light of reports by Kelly and co-workers in which they describe the successful application of a tetrameric PTP which demonstrated good in vivo targeting [14]. Based on their reports, it seems likely that the tetrameric PTP radio-conjugate allows for better in vivo targeting and/or metabolic stability (due to sterics) relative to the monomeric ^{177}Lu-PTP-DO3A. Based on the strong in vitro performance of the ^{177}Lu-PTP-DO3A, it seems likely that the poor in vivo performance is due, at least partially, to the metabolic instability of the PTP. It is well known that peptides with a free N-terminus can be susceptible to certain proteases called aminopeptidases [186], which are also known to exist in the blood and on the surface of the tumor vasculature [187]. The rapid in vivo metabolism of ^{177}Lu-PTP-DO3A would explain both the poor initial uptake at 1 h and rapid clearance by the 4 h time-point.

To further examine the metabolic stability of ^{177}Lu-PTP-DO3A, an in vitro serum stability study was conducted using both radiolabeled and un-metallated peptides. Using radio-HPLC and LC-MS, it was found that PTP was easily degraded in serum leading to one major and two minor metabolites. The major metabolite corresponded to the loss of the first lysine residue, while the other two minor metabolites corresponded to cleavages

at the subsequent amino acids ^{2}T-^{3}L and ^{3}L-^{4}L. The sequential nature of these degradations is consistent with what would be expected from an aminopeptidase [188]. However, to further confirm this, a protease inhibition study should be performed in the future. Given this and the in vivo biodistribution data, it is clear that alterations to the PTP are needed to increase the in vivo metabolic stability of future PTP radio-conjugates.

The peptide-polymer conjugate is a promising targeting platform for targeted diagnostic and therapeutic agent development due to the potential of the multi-valency effect [189]. We prepared “click” reactive HPMA copolymers bearing azide groups on the side chains and conjugated it with an alkyne group functionalized PTP (peptide 7). The “click” chemistry resulted in incorporation efficiencies of greater than 60%. It has been shown that the incorporation of receptor-targeted peptides of just 10 mole% into HPMA copolymers has led to substantial increases in multivalent binding [190], however, the resulting PTP-HPMA conjugate demonstrated substantially lower than expected binding towards pancreatic tumors, as established by flow cytometry and the competitive binding studies. This is particularly evident, when one compares the cell-associated activity of the ^{177}Lu-PTP-HPMA conjugate to the ^{177}Lu-PTP-DO3A peptide from the internalization and efflux studies. The reason why the plectin-1 binding for the PTP- HPMA conjugate is so poor remains unknown. One possible explanation is that the steric hindrance between the peptide and the polymer backbone is impeding plectin-1 binding. In such a case, a possible solution might be the insertion of a longer PEG chain between the PTP and the HPMA copolymer to alleviate steric interference.

4.5 CONCLUSION

In this study, we found that the PTP analogue with DOTA conjugated to the C terminal (PTP-DO3A) had significantly higher binding affinity and cellular uptake as compared to the N terminal DOTA conjugated PTP (DO3A-PTP). The PTP-DO3A was un-stable in vivo, leading to decreased targeting efficacy to pancreatic tumor in a xenograft mouse model. PTP can be efficiently conjugated to HPMA copolymer by “click chemistry”, but the resulting PTP-HPMA conjugate lost the binding affinity towards plectin-1, possibly due to steric hindrance. The ^{177}Lu-labeled PTP-HPMA exhibited much lower targeting ability to pancreatic tumors as compared to ^{177}Lu-labeled PTP in vitro.

Chapter 5

Summary

Pancreatic tumor remains difficult to diagnose at the early stages and all clinically available biomarkers and diagnostic tools fail to detect early stage PDAC or suffer from low specificity and sensitivity [14]. SPECT/CT imaging can provide information about the anatomical structures as well as the functional, metabolic or molecular status of specific tissues or organs and holds great potential for PDAC diagnosis because of its high sensitivity and spatial resolution [191]. However, the application of SPECT/CT in PDAC diagnostic imaging is hampered by the lack of an effective clinical radiotracer. There is an urgent need for the development of more effective SPECT/CT probes for the diagnosis of pancreatic tumors.

The advancement of nanomedicine has offered new opportunities for the development of novel probes for the effective targeting of cancer [192]. Nanomedicine has many advantages such as the increased circulation time and targeted drug delivery [193]. Nanomaterials can passively target tumor sites due to the EPR effect [40]. Those nanomaterials can be multifunctional and modified to carry diagnostic probes and/or therapeutic drugs with the targeting ligands at the same time [194]. Many nanomedicine platforms have been evaluated for pancreatic cancer diagnosis [195]. One of the platforms we are interested in is HPMA copolymers. HPMA copolymers are non-toxic and non-immunogenic and many of HPMA-drug conjugates have been evaluated in clinical trials without causing any major side effects [62]. HPMA copolymers can effectively accumulate in the tumor sites through the EPR effect. HPMA copolymers can

be multifunctional and modified to introduce diagnostic probes such as radioisotopes or fluorescent dyes, or carry therapeutic drugs and targeting ligands. Radiolabeled HPMA copolymers have been successfully applied to for tumor imaging with the imaging modality SPECT/CT. However, a major problem associated the radiolabeled HPMA copolymers, as well as other nanomedicine platforms, is their opsonization and sequestration by the mononuclear phagocyte system [196]. As a result of MPS uptake, these polymeric drugs tend to accumulate in the liver and spleen. This MPS accumulation in non-target organs can hinder identification of resident or nearby metastatic malignant lesions thereby decreasing the diagnostic efficacy of polymer based diagnostic agents. With regard to therapeutic applications, the non-target accumulation of these polymeric drugs can lead to significant toxicities which may be dose-limiting [181].

We are interested in developing new approaches in which radiolabeled HPMA copolymers can be synthetically modified to significantly reduce the MPS accumulation and/or to increase the tumor accumulation, thereby enhancing the diagnostic and/or radiotherapeutic efficacy of the agents. In **chapter 2**, we incorporated metabolic active linkers (MAL) into radiolabeled HPMA copolymers in order to reduce the MPS radioactivity accumulation. Those linkers are peptide substrates for cathepsin B and S, which have higher levels of expression in MPS tissues as compared to tumor tissues. We confirmed the in vitro cleavage of these linkers and conjugated them to a 343 kDa HPMA copolymer prepared by RAFT polymerization. We further investigated the cellular uptake of those conjugates; all the conjugates were easily taken up by differentiated macrophages while little uptake was observed in human pancreatic tumor cells. All the polymer conjugates were labeled efficiently with ^{177}Lu. The in vitro serum stability studies

of all the radiolabeled conjugates revealed no significant proteolysis. However, we found that after treatment with cathepsins, small molecule radio-metabolites were generated from radiolabeled HPMA bearing MAL. The small molecular weight and hydrophilic radio-metabolite were considered to be favorably cleared away from the MPS tissues after in vivo accumulation. In a pancreatic tumor xenograft mice model, the synthesized cathepsin B and S cleavable HPMA copolymers: ^{177}Lu-MAC1 and ^{177}Lu-MAC2 demonstrated a substantial decrease in long-term liver and spleen retention relative to the non-cleavable HPMA copolymer control (^{177}Lu-MAC0). The significant reduction in liver and spleen retention observed in these studies prove that the MAL design is capable of enhancing radioactivity clearance from the MPS tissues.

The promising results from the previous study prompted us to further develop a better HPMA copolymer based diagnostic agent used for SPECT/CT imaging. In **chapter 3**, an HPMA copolymer with molecular weight 109 kDa and PDI 1.3 was prepared by RAFT and conjugated to three different cathepsin S cleavable linkers in order to evaluate the structure-activity relationship with regard to the length of the linking groups on the in vitro and in vivo efficacy of radiolabeled cathepsin S cleavable HPMA. The 109 kDa allowed efficient tumor targeting due to the molecular weight being above the renal clearance threshold (~45 kDa), but also demonstrated relatively fast clearance from the blood to achieve satisfying tumor to blood ratio. In vitro cleavage assays showed that the longest linking group (13 atoms) possessed the highest cathepsin S cleavage kinetics. In addition, confocal microscopy confirmed the selective uptake of HPMA conjugates in differentiated macrophages and trafficking to the lysosomal cellular compartments. Contrary to in vitro observations, in vivo biodistribution studies in pancreatic tumor bearing mice revealed that the linking group length in the cathepsin S

cleavable linker design did not substantially impact the non-target clearance of radiolabeled cathepsin S cleavable HPMA. However, in the case of HPAC tumor retention, the one with the shortest length linker - CSC1 demonstrated significantly higher levels of retention relative to the other cathepsin S cleavable HPMA copolymers. This gave CSC1 superior tumor-to-non-target ratios as confirmed by longitudinal SPECT/CT imaging studies. Our results demonstrated that the introduction of cathepsin S cleavable linkers can substantially improve the non-target radioactivity clearance of HPMA copolymer based radiopharmaceuticals, and likely many other nanomedicine platforms, leading to an enhancement in the tumor-to-non-target ratios and ultimately clinical translation.

Many peptide ligands have been conjugated to polymers and have successfully increased the in vitro and/or in vivo targeting ability of polymers [197]. Pancreatic tumors can highly express many biomarker proteins[44] and these biomarkers can become potential targets to increase the tumor targeting efficacy of HPMA copolymers. The plectin-1 protein is a recently discovered biomarker that is aberrantly expressed on the extracellular surface of PDAC [14]. The peptide sequence KTLLPTP, discovered by phage display,[37] was found to have submicromolar affinity for plectin-1. In **chapter 4**, to further improve the pancreatic tumor targeting ability of HPMA copolymer and solve the problem associated with the low tumor uptake of plectin-1 targeted peptide (PTP) in vivo, we prepared a ^{177}Lu-labeled PTP-HPMA conjugate and evaluated its targeting efficacy. We found even though up to 10 mole% PTP could be successfully conjugated with HPMA copolymers through “click chemistry”, the PTP-HPMA conjugate did not display any multivalent effects but rather lost the binding affinity towards plectin-1. The ^{177}Lu-labeled HPMA-PTP exhibited very little uptake in pancreatic cancer cells while the

^{177}Lu-labeled PTP showed very efficient uptake in vitro. Incorporation of the PTP into the HPMA copolymer diminished the activity of the peptide. One possible explanation is that steric hindrance, between the targeting peptide and the polymer backbone, inhibits plectin-1 binding. A possible solution can be inserting longer PEG chains between the targeting peptide and the HPMA copolymer.

Future Studies

Even though the above studies proved the great potential of ^{177}Lu radiolabeled cathepsin S cleavable HPMA for pancreatic tumor imaging, the agent can be improved to achieve better efficacy.

1) The efficacy of ^{177}Lu-labeled cathepsin S cleavable HPMA for pancreatic tumor imaging should be determined in a transgenic mice model. In chapter 2 and 3, we evaluated the cathepsin S cleavable HPMA in a subcutaneous xenograft mouse model and had encouraging results. The xenograft mouse model provides a relevant and convenient model for the initial evaluation of many investigational drugs. However, it is well-known that there are many great differences between the xenograft mouse model and the transgenic mouse model. The transgenic mouse model can offer many advantages in our future study: (1) the mice are immuno-competent such that the tumor microenvironment can be mirrored as much as possible in a murine model; (2) specific genetic abnormalities present in human tumors can be reproduced, in an inducible manner, at specific ages in the tissue-type of origin; (3) the stages of tumor progression can be studied over time; (4) several therapeutic approaches can be explored at various stages of tumor development [198]. The model we will use is the LSL-Kras^{G12D}; p53^{R172H};

Pdx-1-Cre (KPC) mouse model. The KPC model is well validated as a clinically relevant model of the morphology, metastatic spread, and chemotherapeutic response of pancreatic cancer. For example, treatment of the KPC model with gemcitabine gave only a 10-15% response rate, correlating well with the clinical disease profile. The evaluation of our agents in a transgenic mouse model will help to better measure the potential towards clinical translation.

2) Other biomarkers and targeting ligands can be exploited for pancreatic tumor targeting. In this thesis, we have successfully explored the feasibility of incorporating targeted peptide ligands (PTP) into HPMA copolymers even though the final conjugate did not exhibit significant binding affinity. The failure may be due to the steric hindrance problem. We'd like to investigate whether adding longer spacers between the peptide ligand and polymer backbone can increase the interaction. Pancreatic tumors also express many other receptors such as EGFR and uPAR, which can become potential targets [199, 200]. Peptide ligands with high affinity to those receptors have been reported previously and can be conjugated to HPMA copolymers using similar strategies. However, those peptide polymer conjugates should be designed carefully and investigated in detail using various in vitro and in vivo studies to determine their structure-activity relationships.

3) Radiotherapeutic efficacy study can be carried out to prove another advantage of ^{177}Lu labeled cathepsin S cleavable HPMA. ^{177}Lu is also an effective beta emitter, which enables the application of ^{177}Lu-labeled cathepsin S cleavable HPMA for tumor targeted radiotherapy. The cathepsin S cleavable HPMA can lead to lower liver and spleen radioactivity accumulation, which should help increase the therapeutic index. This

means we can deliver a higher dose of radioactivity to the tumor site without causing any greater damage to other non-target tissues. The maximum tolerated doses for the ^{177}Lu radiolabeled cathepsin S cleavable HPMA copolymers is expected to be higher than the non-cleavable control copolymer and can be easily determined in a mouse model.

BIBLIOGRAPHY

[1] Siegel RL, Miller KD, Jemal A. Cancer statistics, 2015. CA: a cancer journal for clinicians. 2015;65:5-29.

[2] Koorstra JB, Hustinx SR, Offerhaus GJ, Maitra A. Pancreatic carcinogenesis. Pancreatology. 2008;8:110-25.

[3] Hezel AF, Kimmelman AC, Stanger BZ, Bardeesy N, Depinho RA. Genetics and biology of pancreatic ductal adenocarcinoma. Genes & development. 2006;20:1218-49.

[4] Maitra A, Fukushima N, Takaori K, Hruban RH. Precursors to invasive pancreatic cancer. Advances in anatomic pathology. 2005;12:81-91.

[5] Matthaei H, Schulick RD, Hruban RH, Maitra A. Cystic precursors to invasive pancreatic cancer. Nature reviews Gastroenterology & hepatology. 2011;8:141-50.

[6] Hruban RH, Goggins M, Parsons J, Kern SE. Progression model for pancreatic cancer. Clinical cancer research : an official journal of the American Association for Cancer Research. 2000;6:2969-72.

[7] Hruban RH, Maitra A, Goggins M. Update on pancreatic intraepithelial neoplasia. International journal of clinical and experimental pathology. 2008;1:306-16.

[8] Shi S, Yao W, Xu J, Long J, Liu C, Yu X. Combinational therapy: new hope for pancreatic cancer? Cancer letters. 2012;317:127-35.

[9] Waghray M, Yalamanchili M, di Magliano MP, Simeone DM. Deciphering the role of stroma in pancreatic cancer. Current opinion in gastroenterology. 2013;29:537-43.

[10] Von Hoff DD, Ervin T, Arena FP, Chiorean EG, Infante J, Moore M, et al. Increased survival in pancreatic cancer with nab-paclitaxel plus gemcitabine. The New England journal of medicine. 2013;369:1691-703.

[11] Hsueh CT. Pancreatic cancer: current standards, research updates and future directions. Journal of gastrointestinal oncology. 2011;2:123-5.

[12] Chari ST, Kelly K, Hollingsworth MA, Thayer SP, Ahlquist DA, Andersen DK, et al. Early Detection of Sporadic Pancreatic Cancer: Summative Review. Pancreas. 2015.

[13] Furukawa H, Okada S, Saisho H, Ariyama J, Karasawa E, Nakaizumi A, et al. Clinicopathologic features of small pancreatic adenocarcinoma. A collective study. Cancer. 1996;78:986-90.

[14] Bausch D, Thomas S, Mino-Kenudson M, Fernandez-del CC, Bauer TW, Williams M, et al. Plectin-1 as a novel biomarker for pancreatic cancer. Clinical cancer research : an official journal of the American Association for Cancer Research. 2011;17:302-9.

[15] Goggins M. Identifying molecular markers for the early detection of pancreatic neoplasia. Seminars in oncology. 2007;34:303-10.

[16] Riker A, Libutti SK, Bartlett DL. Advances in the early detection, diagnosis, and staging of pancreatic cancer. Surgical oncology. 1997;6:157-69.

[17] Steinberg W. The clinical utility of the CA 19-9 tumor-associated antigen. The American journal of gastroenterology. 1990;85:350-5.

[18] Goonetilleke KS, Siriwardena AK. Systematic review of carbohydrate antigen (CA 19-9) as a biochemical marker in the diagnosis of pancreatic cancer. European journal of surgical oncology : the journal of the European Society of Surgical Oncology and the British Association of Surgical Oncology. 2007;33:266-70.

[19] Duffy MJ. CA 19-9 as a marker for gastrointestinal cancers: a review. Annals of clinical biochemistry. 1998;35 (Pt 3):364-70.

[20] Miura F, Takada T, Amano H, Yoshida M, Furui S, Takeshita K. Diagnosis of pancreatic cancer. HPB : the official journal of the International Hepato Pancreato Biliary Association. 2006;8:337-42.

[21] Rosewicz S, Wiedenmann B. Pancreatic carcinoma. Lancet. 1997;349:485-9.

[22] Muller MF, Meyenberger C, Bertschinger P, Schaer R, Marincek B. Pancreatic tumors: evaluation with endoscopic US, CT, and MR imaging. Radiology. 1994;190:745-51.

[23] Rickes S, Unkrodt K, Neye H, Ocran KW, Wermke W. Differentiation of pancreatic tumours by conventional ultrasound, unenhanced and echo-enhanced power Doppler sonography. Scandinavian journal of gastroenterology. 2002;37:1313-20.

[24] Tummala P, Junaidi O, Agarwal B. Imaging of pancreatic cancer: An overview. J Gastrointest Oncol. 2011;2:168-74.

[25] Catalano C, Laghi A, Fraioli F, Pediconi F, Napoli A, Danti M, et al. Pancreatic carcinoma: the role of high-resolution multislice spiral CT in the diagnosis and assessment of resectability. European radiology. 2003;13:149-56.

[26] Takeshita K, Kutomi K, Haruyama T, Watanabe A, Furui S, Fukushima J, et al. Imaging of early pancreatic cancer on multidetector row helical computed tomography. The British journal of radiology. 2010;83:823-30.

[27] Takakura K, Sumiyama K, Munakata K, Ashida H, Arihiro S, Kakutani H, et al. Clinical usefulness of diffusion-weighted MR imaging for detection of pancreatic cancer: comparison with enhanced multidetector-row CT. Abdominal imaging. 2011;36:457-62.

[28] Jenkins JP, Braganza JM, Hickey DS, Isherwood I, Machin M. Quantitative tissue characterisation in pancreatic disease using magnetic resonance imaging. The British journal of radiology. 1987;60:333-41.

[29] Johnson PT, Outwater EK. Pancreatic carcinoma versus chronic pancreatitis: dynamic MR imaging. Radiology. 1999;212:213-8.

[30] Barrios-Lopez B, Bergstrom K. Radiolabeled Sugars used for PET and SPECT Imaging: Mini-Review. Current radiopharmaceuticals. 2015.

[31] Heinrich S, Goerres GW, Schafer M, Sagmeister M, Bauerfeind P, Pestalozzi BC, et al. Positron emission tomography/computed tomography influences on the management

of resectable pancreatic cancer and its cost-effectiveness. Annals of surgery. 2005;242:235-43.

[32] Diederichs CG, Staib L, Glatting G, Beger HG, Reske SN. FDG PET: elevated plasma glucose reduces both uptake and detection rate of pancreatic malignancies. Journal of nuclear medicine : official publication, Society of Nuclear Medicine. 1998;39:1030-3.

[33] Yoshimoto M, Hayakawa T, Mutoh M, Imai T, Tsuda K, Kimura S, et al. In vivo SPECT imaging with 111In-DOTA-c(RGDfK) to detect early pancreatic cancer in a hamster pancreatic carcinogenesis model. Journal of nuclear medicine : official publication, Society of Nuclear Medicine. 2012;53:765-71.

[34] Liu Z, Liu H, Ma T, Sun X, Shi J, Jia B, et al. Integrin alphavbeta6-Targeted SPECT Imaging for Pancreatic Cancer Detection. Journal of nuclear medicine : official publication, Society of Nuclear Medicine. 2014;55:989-94.

[35] Hosotani R, Kawaguchi M, Masui T, Koshiba T, Ida J, Fujimoto K, et al. Expression of integrin alphaVbeta3 in pancreatic carcinoma: relation to MMP-2 activation and lymph node metastasis. Pancreas. 2002;25:e30-5.

[36] McCusker CF, Kocienski PJ, Boyle FT, Schatzlein AG. Solid-phase synthesis of c(RGDfK) derivatives: on-resin cyclisation and lysine functionalisation. Bioorganic & medicinal chemistry letters. 2002;12:547-9.

[37] Kelly KA, Bardeesy N, Anbazhagan R, Gurumurthy S, Berger J, Alencar H, et al. Targeted nanoparticles for imaging incipient pancreatic ductal adenocarcinoma. PLoS medicine. 2008;5:e85.

[38] Fan Z, Fu PP, Yu H, Ray PC. Theranostic nanomedicine for cancer detection and treatment. Journal of food and drug analysis. 2014;22:3-17.

[39] Lundqvist M, Stigler J, Elia G, Lynch I, Cedervall T, Dawson KA. Nanoparticle size and surface properties determine the protein corona with possible implications for

biological impacts. Proceedings of the National Academy of Sciences of the United States of America. 2008;105:14265-70.

[40] Greish K. Enhanced permeability and retention (EPR) effect for anticancer nanomedicine drug targeting. Methods Mol Biol. 2010;624:25-37.

[41] Maeda H. Tumor-selective delivery of macromolecular drugs via the EPR effect: background and future prospects. Bioconjugate chemistry. 2010;21:797-802.

[42] Mukherjee B, Satapathy BS, Mondal L, Dey NS, Maji R. Potentials and challenges of active targeting at the tumor cells by engineered polymeric nanoparticles. Current pharmaceutical biotechnology. 2013;14:1250-63.

[43] Yang F, Jin C, Subedi S, Lee CL, Wang Q, Jiang Y, et al. Emerging inorganic nanomaterials for pancreatic cancer diagnosis and treatment. Cancer treatment reviews. 2012;38:566-79.

[44] Bhat K, Wang F, Ma Q, Li Q, Mallik S, Hsieh TC, et al. Advances in biomarker research for pancreatic cancer. Current pharmaceutical design. 2012;18:2439-51.

[45] Hedgire SS, Mino-Kenudson M, Elmi A, Thayer S, Fernandez-del Castillo C, Harisinghani MG. Enhanced primary tumor delineation in pancreatic adenocarcinoma using ultrasmall super paramagnetic iron oxide nanoparticle-ferumoxytol: an initial experience with histopathologic correlation. International journal of nanomedicine. 2014;9:1891-6.

[46] Yang L, Mao H, Cao Z, Wang YA, Peng X, Wang X, et al. Molecular imaging of pancreatic cancer in an animal model using targeted multifunctional nanoparticles. Gastroenterology. 2009;136:1514-25 e2.

[47] He Y, Liu XD, Chen ZY, Zhu J, Xiong Y, Li K, et al. Interaction between cancer cells and stromal fibroblasts is required for activation of the uPAR-uPA-MMP-2 cascade in pancreatic cancer metastasis. Clinical cancer research : an official journal of the American Association for Cancer Research. 2007;13:3115-24.

[48] Troiani T, Martinelli E, Capasso A, Morgillo F, Orditura M, De Vita F, et al. Targeting EGFR in pancreatic cancer treatment. Current drug targets. 2012;13:802-10.

[49] Yang L, Mao H, Wang YA, Cao Z, Peng X, Wang X, et al. Single chain epidermal growth factor receptor antibody conjugated nanoparticles for in vivo tumor targeting and imaging. Small. 2009;5:235-43.

[50] Zhang H, Yee D, Wang C. Quantum dots for cancer diagnosis and therapy: biological and clinical perspectives. Nanomedicine (Lond). 2008;3:83-91.

[51] Ding H, Yong KT, Law WC, Roy I, Hu R, Wu F, et al. Non-invasive tumor detection in small animals using novel functional Pluronic nanomicelles conjugated with anti-mesothelin antibody. Nanoscale. 2011;3:1813-22.

[52] Liu L, Yong KT, Roy I, Law WC, Ye L, Liu J, et al. Bioconjugated pluronic triblock-copolymer micelle-encapsulated quantum dots for targeted imaging of cancer: in vitro and in vivo studies. Theranostics. 2012;2:705-13.

[53] Hu R, Yong KT, Roy I, Ding H, Law WC, Cai H, et al. Functionalized near-infrared quantum dots for in vivo tumor vasculature imaging. Nanotechnology. 2010;21:145105.

[54] Gabizon AA, Shmeeda H, Zalipsky S. Pros and cons of the liposome platform in cancer drug targeting. Journal of liposome research. 2006;16:175-83.

[55] Yang F, Jin C, Jiang Y, Li J, Di Y, Ni Q, et al. Liposome based delivery systems in pancreatic cancer treatment: from bench to bedside. Cancer treatment reviews. 2011;37:633-42.

[56] Yoshida M, Takimoto R, Murase K, Sato Y, Hirakawa M, Tamura F, et al. Targeting anticancer drug delivery to pancreatic cancer cells using a fucose-bound nanoparticle approach. PloS one. 2012;7:e39545.

[57] Deng L, Ke X, He Z, Yang D, Gong H, Zhang Y, et al. A MSLN-targeted multifunctional nanoimmunoliposome for MRI and targeting therapy in pancreatic cancer. International journal of nanomedicine. 2012;7:5053-65.

[58] Eser S, Messer M, Eser P, von Werder A, Seidler B, Bajbouj M, et al. In vivo diagnosis of murine pancreatic intraepithelial neoplasia and early-stage pancreatic cancer by molecular imaging. Proceedings of the National Academy of Sciences of the United States of America. 2011;108:9945-50.

[59] Kunjachan S, Pola R, Gremse F, Theek B, Ehling J, Moeckel D, et al. Passive versus active tumor targeting using RGD- and NGR-modified polymeric nanomedicines. Nano letters. 2014;14:972-81.

[60] Buckway B, Wang Y, Ray A, Ghandehari H. Overcoming the stromal barrier for targeted delivery of HPMA copolymers to pancreatic tumors. International journal of pharmaceutics. 2013;456:202-11.

[61] Lu ZR. Molecular imaging of HPMA copolymers: visualizing drug delivery in cell, mouse and man. Advanced drug delivery reviews. 2010;62:246-57.

[62] Kopecek J, Kopeckova P. HPMA copolymers: origins, early developments, present, and future. Advanced drug delivery reviews. 2010;62:122-49.

[63] Duncan R, Vicent MJ. Do HPMA copolymer conjugates have a future as clinically useful nanomedicines? A critical overview of current status and future opportunities. Advanced drug delivery reviews. 2010;62:272-82.

[64] Mitra A, Nan A, Papadimitriou JC, Ghandehari H, Line BR. Polymer-peptide conjugates for angiogenesis targeted tumor radiotherapy. Nuclear medicine and biology. 2006;33:43-52.

[65] Buckway B, Wang Y, Ray A, Ghandehari H. In vitro evaluation of HPMA-copolymers targeted to HER2 expressing pancreatic tumor cells for image guided drug delivery. Macromolecular bioscience. 2014;14:92-9.

[66] Ogbomo SM, Shi W, Wagh NK, Zhou Z, Brusnahan SK, Garrison JC. 177Lu-labeled HPMA copolymers utilizing cathepsin B and S cleavable linkers: synthesis,

characterization and preliminary in vivo investigation in a pancreatic cancer model. Nuclear medicine and biology. 2013;40:606-17.

[67] Pimm MV, Perkins AC, Strohalm J, Ulbrich K, Duncan R. Gamma scintigraphy of the biodistribution of 123I-labelled N-(2-hydroxypropyl)methacrylamide copolymer-doxorubicin conjugates in mice with transplanted melanoma and mammary carcinoma. Journal of drug targeting. 1996;3:375-83.

[68] Seymour LW, Miyamoto Y, Maeda H, Brereton M, Strohalm J, Ulbrich K, et al. Influence of molecular weight on passive tumour accumulation of a soluble macromolecular drug carrier. Eur J Cancer. 1995;31A:766-70.

[69] Pimm MV, Perkins AC, Duncan R, Ulbrich K. Targeting of N-(2-hydroxypropyl)methacrylamide copolymer-doxorubicin conjugate to the hepatocyte galactose-receptor in mice: visualisation and quantification by gamma scintigraphy as a basis for clinical targeting studies. Journal of drug targeting. 1993;1:125-31.

[70] Mitra A, Mulholland J, Nan A, McNeill E, Ghandehari H, Line BR. Targeting tumor angiogenic vasculature using polymer-RGD conjugates. Journal of controlled release : official journal of the Controlled Release Society. 2005;102:191-201.

[71] Herth MM, Barz M, Moderegger D, Allmeroth M, Jahn M, Thews O, et al. Radioactive labeling of defined HPMA-based polymeric structures using [18F]FETos for in vivo imaging by positron emission tomography. Biomacromolecules. 2009;10:1697-703.

[72] Herth MM, Barz M, Jahn M, Zentel R, Rosch F. 72/74As-labeling of HPMA based polymers for long-term in vivo PET imaging. Bioorganic & medicinal chemistry letters. 2010;20:5454-8.

[73] Kissel M, Peschke P, Subr V, Ulbrich K, Schuhmacher J, Debus J, et al. Synthetic macromolecular drug carriers: biodistribution of poly[(N-2-hydroxypropyl)methacrylamide]

copolymers and their accumulation in solid rat tumors. PDA journal of pharmaceutical science and technology / PDA. 2001;55:191-201.

[74] Kissel M, Peschke P, Subr V, Ulbrich K, Strunz AM, Kuhnlein R, et al. Detection and cellular localisation of the synthetic soluble macromolecular drug carrier pHPMA. European journal of nuclear medicine and molecular imaging. 2002;29:1055-62.

[75] Lammers T, Kuhnlein R, Kissel M, Subr V, Etrych T, Pola R, et al. Effect of physicochemical modification on the biodistribution and tumor accumulation of HPMA copolymers. Journal of controlled release : official journal of the Controlled Release Society. 2005;110:103-18.

[76] Lammers T, Peschke P, Kuhnlein R, Subr V, Ulbrich K, Huber P, et al. Effect of intratumoral injection on the biodistribution and the therapeutic potential of HPMA copolymer-based drug delivery systems. Neoplasia. 2006;8:788-95.

[77] Mitra A, Nan A, Ghandehari H, McNeill E, Mulholland J, Line BR. Technetium-99m-Labeled N-(2-hydroxypropyl) methacrylamide copolymers: synthesis, characterization, and in vivo biodistribution. Pharmaceutical research. 2004;21:1153-9.

[78] Zhang R, Luo K, Yang J, Sima M, Sun Y, Janat-Amsbury MM, et al. Synthesis and evaluation of a backbone biodegradable multiblock HPMA copolymer nanocarrier for the systemic delivery of paclitaxel. Journal of controlled release : official journal of the Controlled Release Society. 2013;166:66-74.

[79] Zhang R, Yang J, Sima M, Zhou Y, Kopecek J. Sequential combination therapy of ovarian cancer with degradable N-(2-hydroxypropyl)methacrylamide copolymer paclitaxel and gemcitabine conjugates. Proceedings of the National Academy of Sciences of the United States of America. 2014;111:12181-6.

[80] Allmeroth M, Moderegger D, Biesalski B, Koynov K, Rosch F, Thews O, et al. Modifying the body distribution of HPMA-based copolymers by molecular weight and aggregate formation. Biomacromolecules. 2011;12:2841-9.

[81] Allmeroth M, Moderegger D, Gundel D, Buchholz HG, Mohr N, Koynov K, et al. PEGylation of HPMA-based block copolymers enhances tumor accumulation in vivo: a quantitative study using radiolabeling and positron emission tomography. Journal of controlled release : official journal of the Controlled Release Society. 2013;172:77-85.

[82] Wall DA, Hubbard AL. Galactose-specific recognition system of mammalian liver: receptor distribution on the hepatocyte cell surface. The Journal of cell biology. 1981;90:687-96.

[83] Seymour LW, Ulbrich K, Wedge SR, Hume IC, Strohalm J, Duncan R. N-(2-hydroxypropyl)methacrylamide copolymers targeted to the hepatocyte galactose-receptor: pharmacokinetics in DBA2 mice. British journal of cancer. 1991;63:859-66.

[84] Pimm MV, Perkins AC, Strohalm J, Ulbrich K, Duncan R. Gamma scintigraphy of a 123I-labelled N-(2-hydroxypropyl)methacrylamide copolymer-doxorubicin conjugate containing galactosamine following intravenous administration to nude mice bearing hepatic human colon carcinoma. Journal of drug targeting. 1996;3:385-90.

[85] Ledermann JA, Canevari S, Thigpen T. Targeting the Folate Receptor: Diagnostic and therapeutic approaches to personalize cancer treatments. Annals of oncology : official journal of the European Society for Medical Oncology / ESMO. 2015.

[86] Schieferstein H, Kelsch A, Reibel A, Koynov K, Barz M, Buchholz HG, et al. 18F-Radiolabeling, preliminary evaluation of folate-pHPMA conjugates via PET. Macromolecular bioscience. 2014;14:1396-405.

[87] Rivera LB, Bergers G. Angiogenesis. Targeting vascular sprouts. Science. 2014;344:1449-50.

[88] Ranieri G. Hot topic: targeting tumor angiogenesis: an update. Current medicinal chemistry. 2012;19:937.

[89] Garanger E, Boturyn D, Dumy P. Tumor targeting with RGD peptide ligands-design of new molecular conjugates for imaging and therapy of cancers. Anti-cancer agents in medicinal chemistry. 2007;7:552-8.

[90] Line BR, Mitra A, Nan A, Ghandehari H. Targeting tumor angiogenesis: comparison of peptide and polymer-peptide conjugates. Journal of nuclear medicine : official publication, Society of Nuclear Medicine. 2005;46:1552-60.

[91] Mitra A, Coleman T, Borgman M, Nan A, Ghandehari H, Line BR. Polymeric conjugates of mono- and bi-cyclic alphaVbeta3 binding peptides for tumor targeting. Journal of controlled release : official journal of the Controlled Release Society. 2006;114:175-83.

[92] Deutscher SL, Figueroa SD, Kumar SR. Tumor targeting and SPECT imaging properties of an (111)In-labeled galectin-3 binding peptide in prostate carcinoma. Nuclear medicine and biology. 2009;36:137-46.

[93] Inohara H, Akahani S, Koths K, Raz A. Interactions between galectin-3 and Mac-2-binding protein mediate cell-cell adhesion. Cancer research. 1996;56:4530-4.

[94] Yang Y, Li L, Zhou Z, Yang Q, Liu C, Huang Y. Targeting prostate carcinoma by G3-C12 peptide conjugated N-(2-hydroxypropyl)methacrylamide copolymers. Molecular pharmaceutics. 2014;11:3251-60.

[95] Lammers T, Ulbrich K. HPMA copolymers: 30 years of advances. Advanced drug delivery reviews. 2010;62:119-21.

[96] Vasey PA, Kaye SB, Morrison R, Twelves C, Wilson P, Duncan R, et al. Phase I clinical and pharmacokinetic study of PK1 [N-(2-hydroxypropyl)methacrylamide copolymer doxorubicin]: first member of a new class of chemotherapeutic agents-drug-polymer conjugates. Cancer Research Campaign Phase I/II Committee. Clin Cancer Res. 1999;5:83-94.

[97] Huis In 't Veld R, Storm G, Hennink WE, Kiessling F, Lammers T. Macromolecular nanotheranostics for multimodal anticancer therapy. Nanoscale. 2011;3:4022-34.

[98] Buckway B, Frazier N, Gormley AJ, Ray A, Ghandehari H. Gold nanorod-mediated hyperthermia enhances the efficacy of HPMA copolymer-90Y conjugates in treatment of prostate tumors. Nuclear medicine and biology. 2014;41:282-9.

[99] Blanco E, Kessinger CW, Sumer BD, Gao J. Multifunctional micellar nanomedicine for cancer therapy. Exp Biol Med (Maywood). 2009;234:123-31.

[100] Duncan R. The dawning era of polymer therapeutics. Nat Rev Drug Discov. 2003;2:347-60.

[101] Hamoudeh M, Kamleh MA, Diab R, Fessi H. Radionuclides delivery systems for nuclear imaging and radiotherapy of cancer. Advanced drug delivery reviews. 2008;60:1329-46.

[102] Kawaguchi T, Honda T, Nishihara M, Yamamoto T, Yokoyama M. Histological study on side effects and tumor targeting of a block copolymer micelle on rats. J Control Release. 2009;136:240-6.

[103] Kopeček J, Kopečková P, Minko T, Lu Z. HPMA copolymer-anticancer drug conjugates: design, activity, and mechanism of action. Eur J Pharm Biopharm. 2000;50:61-81.

[104] Mitra A, Coleman T, Borgman M, Nan A, Ghandehari H, Line BR. Polymeric conjugates of mono- and bi-cyclic alpha(V)beta(3) binding peptides for tumor targeting. J Control Release. 2006;114:175-83.

[105] Mitra A, Nan A, Papadimitriou JC, Ghandehari H, Line BR. Polymer-peptide conjugates for angiogenesis targeted tumor radiotherapy. Nucl Med Biol. 2006;33:43-52.

[106] Lammers T, Kühnlein R, Kissel M, Subr V, Etrych T, Pola R, et al. Effect of physicochemical modification on the biodistribution and tumor accumulation of HPMA copolymers. J Control Release. 2005;110:103-18.

[107] Mitra A, Mulholland J, Nan A, McNeill E, Ghandehari H, Line BR. Targeting tumor angiogenic vasculature using polymer-RGD conjugates. J Control Release. 2005;102:191-201.

[108] Line BR, Mitra A, Nan A, Ghandehari H. Targeting tumor angiogenesis: Comparison of peptide and polymer-peptide conjugates. J Nucl Med. 2005;46:1552-60.

[109] Julyan PJ, Seymour LW, Ferry DR, Daryani S, Boivin CM, Doran J, et al. Preliminary clinical study of the distribution of HPMA copolymers bearing doxorubicin and galactosamine. J Control Release. 1999;57:281-90.

[110] Mitra A, Nan A, Ghandehari H, McNeill E, Mulholland J, Line BR. Technetium-99m-labeled N-(2-hydroxypropyl) methacrylamide copolymers: Synthesis, characterization, and in vivo biodistribution. Pharm Res. 2004;21:1153-9.

[111] Berdowska I. Cysteine proteases as disease markers. Clin Chim Acta. 2004;342:41-69.

[112] Yasuda Y, Kaleta J, Brömme D. The role of cathepsins in osteoporosis and arthritis: rationale for the design of new therapeutics. Adv Drug Deliv Rev. 2005;57:973-93.

[113] Shuja S, Sheahan K, Murnane MJ. Cysteine endopeptidase activity levels in normal human tissues, colorectal adenomas and carcinomas. Int J Cancer. 1991;49:341-6.

[114] Qian F, Bajkowski AS, Steiner DF, Chan SJ, Frankfater A. Expression of five cathepsins in murine melanomas of varying metastatic potential and normal tissues. Cancer Res. 1989;49:4870-5.

[115] Petanceska S, Canoll P, Devi LA. Expression of rat cathepsin S in phagocytic cells. J Biol Chem. 1996;271:4403-9.

[116] Shi GP, Webb AC, Foster KE, Knoll JH, Lemere CA, Munger JS, et al. Human cathepsin S: chromosomal localization, gene structure, and tissue distribution. J Biol Chem. 1994;269:11530-6.

[117] Villadangos JA, Ploegh HL. Proteolysis in MHC class II antigen presentation: who's in charge? Immunity. 2000;12:233-9.

[118] Christie RJ, Grainger DW. Design strategies to improve soluble macromolecular delivery constructs. Advanced drug delivery reviews. 2003;55:421-37.

[119] Kukis DL, Novak-Hofer I, DeNardo SJ. Cleavable linkers to enhance selectivity of antibody-targeted therapy of cancer. Cancer Biother Radiopharm. 2001;16:457-67.

[120] York AW, Scales CW, Huang F, McCormick CL. Facile Synthetic Procedure for ω, Primary Amine Functionalization Directly in Water for Subsequent Fluorescent Labeling and Potential Bioconjugation of RAFT-Synthesized (Co)Polymers†. Biomacromolecules. 2007;8:2337-41.

[121] Li M, Meares CF. Synthesis, metal chelate stability studies, and enzyme digestion of a peptide-linked DOTA derivative and its corresponding radiolabeled immunoconjugates. Bioconjug Chem. 1993;4:275-83.

[122] Lützner N, Kalbacher H. Quantifying cathepsin S activity in antigen presenting cells using a novel specific substrate. J Biol Chem. 2008;283:36185-94.

[123] Greish K. Enhanced permeability and retention of macromolecular drugs in solid tumors: A royal gate for targeted anticancer nanomedicines. J Drug Target. 2007;15:457-64.

[124] Greish K. Enhanced permeability and retention (EPR) effect for anticancer nanomedicine drug targeting. Methods Mol Biol. 2010;624:25-37.

[125] Owens DE, 3rd, Peppas NA. Opsonization, biodistribution, and pharmacokinetics of polymeric nanoparticles. Int J Pharm. 2006;307:93-102.

[126] Nie S. Understanding and overcoming major barriers in cancer nanomedicine. Nanomedicine (Lond). 2010;5:523-8.

[127] De Leon-Rodriguez LM, Kovacs Z. The synthesis and chelation chemistry of DOTA-peptide conjugates. Bioconjug Chem. 2008;19:391-402.

[128] Kwekkeboom DJ, Teunissen JJ, Bakker WH, Kooij PP, de Herder WW, Feelders RA, et al. Radiolabeled somatostatin analog [Lu-177-DOTA(0),Tyr(3)] octreotate in patients with endocrine gastroenteropancreatic tumors. J Clin Oncol. 2005;23:2754-62.

[129] Minchinton AI, Tannock IF. Drug penetration in solid tumours. Nat Rev Cancer. 2006;6:583-92.

[130] Lutzner N, Kalbacher H. Quantifying cathepsin S activity in antigen presenting cells using a novel specific substrate. J Biol Chem. 2008;283:36185-94.

[131] Seymour LW, Duncan R, Strohalm J, Kopeček J. Effect of molecular weight (M_w) of N-(2-hydroxypropyl)methacrylamide copolymers on body distribution and rate of excretion after subcutaneous, intraperitoneal, and intravenous administration to rats. J Biomed Mater Res. 1987;21:1341-58.

[132] Siegel R, Naishadham D, Jemal A. Cancer statistics, 2013. CA: a cancer journal for clinicians. 2013;63:11-30.

[133] Hidalgo M. Pancreatic cancer. The New England journal of medicine. 2010;362:1605-17.

[134] Ying JE, Zhu LM, Liu BX. Developments in metastatic pancreatic cancer: is gemcitabine still the standard? World journal of gastroenterology : WJG. 2012;18:736-45.

[135] Fass L. Imaging and cancer: a review. Molecular oncology. 2008;2:115-52.

[136] Bockisch A, Freudenberg LS, Schmidt D, Kuwert T. Hybrid imaging by SPECT/CT and PET/CT: proven outcomes in cancer imaging. Seminars in nuclear medicine. 2009;39:276-89.

[137] Duncan R. Polymer therapeutics as nanomedicines: new perspectives. Current opinion in biotechnology. 2011;22:492-501.

[138] Yuan J, Zhang H, Kaur H, Oupicky D, Peng F. Synthesis and characterization of theranostic poly(HPMA)-c(RGDyK)-DOTA-64Cu copolymer targeting tumor

angiogenesis: tumor localization visualized by positron emission tomography. Molecular imaging. 2013;12:203-12.

[139] Borgman MP, Coleman T, Kolhatkar RB, Geyser-Stoops S, Line BR, Ghandehari H. Tumor-targeted HPMA copolymer-(RGDfK)-(CHX-A''-DTPA) conjugates show increased kidney accumulation. Journal of controlled release : official journal of the Controlled Release Society. 2008;132:193-9.

[140] Lammers T, Subr V, Ulbrich K, Peschke P, Huber PE, Hennink WE, et al. HPMA-based polymer therapeutics improve the efficacy of surgery, of radiotherapy and of chemotherapy combinations. Nanomedicine (Lond). 2010;5:1501-23.

[141] Kopeček J, Kopečková P. HPMA copolymers: origins, early developments, present, and future. Adv Drug Deliv Rev. 2010;62:122-49.

[142] Kopeček J, Kopečková P, Minko T, Lu Z. HPMA copolymer-anticancer drug conjugates: design, activity, and mechanism of action. Eur J Pharm Biopharm. 2000;50:61-81.

[143] Allmeroth M, Moderegger D, Biesalski B, Koynov K, Rösch F, Thews O, et al. Modifying the body distribution of HPMA-based copolymers by molecular weight and aggregate formation. Biomacromolecules. 2011;12:2841-9.

[144] Pike DB, Ghandehari H. HPMA copolymer-cyclic RGD conjugates for tumor targeting. Adv Drug Deliv Rev. 2010;62:167-83.

[145] Owens DE, 3rd, Peppas NA. Opsonization, biodistribution, and pharmacokinetics of polymeric nanoparticles. International Journal of Pharmaceutics. 2006;307:93-102.

[146] Ogbomo SM, Shi W, Wagh NK, Zhou Z, Brusnahan SK, Garrison JC. ^{177}Lu-labeled HPMA copolymers utilizing cathepsin B and S cleavable linkers: Synthesis, characterization and preliminary in vivo investigation in a pancreatic cancer model. Nucl Med Biol. 2013;40:606-17.

[147] Petanceska S, Canoll P, Devi LA. Expression of rat cathepsin S in phagocytic cells. The Journal of biological chemistry. 1996;271:4403-9.

[148] Shi GP, Webb AC, Foster KE, Knoll JH, Lemere CA, Munger JS, et al. Human cathepsin S: chromosomal localization, gene structure, and tissue distribution. The Journal of biological chemistry. 1994;269:11530-6.

[149] Gude M, Ryf J, White P. An accurate method for the quantitation of Fmoc-derivatized solid phase supports. International Journal of Peptide Research and Therapeutics. 2002;9:203-6.

[150] Lützner N, Kalbacher H. Quantifying cathepsin S activity in antigen presenting cells using a novel specific substrate. The Journal of biological chemistry. 2008;283:36185-94.

[151] Ulbrich K, Koňák Č, Tuzar Z, Kopeček J. Solution properties of drug carriers based on poly[N-(2-hydroxypropyl)methacrylamide] containing biodegradable bonds. Die Makromolekulare Chemie. 1987;188:1261-72.

[152] Pan H, Kopeckova P, Wang D, Yang J, Miller S, Kopecek J. Water-soluble HPMA copolymer--prostaglandin E1 conjugates containing a cathepsin K sensitive spacer. Journal of Drug Targeting. 2006;14:425-35.

[153] De Jong WH, Borm PJ. Drug delivery and nanoparticles:applications and hazards. International journal of nanomedicine. 2008;3:133-49.

[154] Riese RJ, Wolf PR, Bromme D, Natkin LR, Villadangos JA, Ploegh HL, et al. Essential role for cathepsin S in MHC class II-associated invariant chain processing and peptide loading. Immunity. 1996;4:357-66.

[155] Driessen C, Lennon-Dumenil AM, Ploegh HL. Individual cathepsins degrade immune complexes internalized by antigen-presenting cells via Fcgamma receptors. European journal of immunology. 2001;31:1592-601.

[156] Plüger EB, Boes M, Alfonso C, Schröter CJ, Kalbacher H, Ploegh HL, et al. Specific role for cathepsin S in the generation of antigenic peptides in vivo. European journal of immunology. 2002;32:467-76.

[157] Shen L, Sigal LJ, Boes M, Rock KL. Important role of cathepsin S in generating peptides for TAP-independent MHC class I crosspresentation in vivo. Immunity. 2004;21:155-65.

[158] Baay M, Brouwer A, Pauwels P, Peeters M, Lardon F. Tumor cells and tumor-associated macrophages: secreted proteins as potential targets for therapy. Clin Dev Immunol. 2011;2011:565187.

[159] Omelyanenko V, Kopečková P, Gentry C, Kopeček J. Targetable HPMA copolymer-adriamycin conjugates. Recognition, internalization, and subcellular fate. Journal of Controlled Release. 1998;53:25-37.

[160] Liu J, Bauer H, Callahan J, Kopečková P, Pan H, Kopeček J. Endocytic uptake of a large array of HPMA copolymers: Elucidation into the dependence on the physicochemical characteristics. Journal of controlled release : official journal of the Controlled Release Society. 2010;143:71-9.

[161] Alexis F, Pridgen E, Molnar LK, Farokhzad OC. Factors affecting the clearance and biodistribution of polymeric nanoparticles. Molecular pharmaceutics. 2008;5:505-15.

[162] Ulery BD, Phanse Y, Sinha A, Wannemuehler MJ, Narasimhan B, Bellaire BH. Polymer chemistry influences monocytic uptake of polyanhydride nanospheres. Pharm Res. 2009;26:683-90.

[163] Beduneau A, Ma Z, Grotepas CB, Kabanov A, Rabinow BE, Gong N, et al. Facilitated monocyte-macrophage uptake and tissue distribution of superparmagnetic iron-oxide nanoparticles. PLoS One. 2009;4:e4343.

[164] Greiner A, Lautwein A, Overkleeft HS, Weber E, Driessen C. Activity and subcellular distribution of cathepsins in primary human monocytes. Journal of Leukocyte Biology. 2003;73:235-42.

[165] Greish K. Enhanced permeability and retention of macromolecular drugs in solid tumors: A royal gate for targeted anticancer nanomedicines. Journal of Drug Targeting. 2007;15:457-64.

[166] Wong TZ, Turkington TG, Polascik TJ, Coleman RE. ProstaScint (capromab pendetide) imaging using hybrid gamma camera-CT technology. AJR American Journal of Roentgenology. 2005;184:676-80.

[167] Jusko WJ, Kung LP, Schmelter RF. Immunopharmacokinetics of 111In-CYT-103 in ovarian cancer patients. Targeted Diagnosis and Therapy. 1992;6:177-90.

[168] Abdel-Nabi H, Doerr RJ, Chan HW, Balu D, Schmelter RF, Maguire RT. In-111-labeled monoclonal antibody immunoscintigraphy in colorectal carcinoma: safety, sensitivity, and preliminary clinical results. Radiology. 1990;175:163-71.

[169] DeNardo SJ, Denardo GL. Targeted radionuclide therapy for solid tumors: an overview. Int J Radiat Oncol Biol Phys. 2006;66:S89-95.

[170] Thariat J, Hannoun-Levi JM, Sun Myint A, Vuong T, Gérard JP. Past, present, and future of radiotherapy for the benefit of patients. Nature reviews Clinical oncology. 2013;10:52-60.

[171] Sadeghi M, Enferadi M, Shirazi A. External and internal radiation therapy: past and future directions. Journal of cancer research and therapeutics. 2010;6:239-48.

[172] Pouget JP, Lozza C, Deshayes E, Boudousq V, Navarro-Teulon I. Introduction to radiobiology of targeted radionuclide therapy. Frontiers in medicine. 2015;2:12.

[173] Williams LE, DeNardo GL, Meredith RF. Targeted radionuclide therapy. Med Phys. 2008;35:3062-8.

[174] Sgouros G. Alpha-particles for targeted therapy. Adv Drug Deliv Rev. 2008;60:1402-6.

[175] Vaidyanathan G, Zalutsky MR. Applications of ^{211}At and ^{223}Ra in targeted alpha-particle radiotherapy. Current radiopharmaceuticals. 2011;4:283-94.

[176] de Jong M, Breeman WAP, Valkema R, Bernard BF, Krenning EP. Combination radionuclide therapy using Lu-177- and Y-90-Labeled somatostatin analogs. J Nucl Med. 2005;46:13s-7s.

[177] DeNardo SJ. Radioimmunodetection and therapy of breast cancer. Semin Nucl Med. 2005;35:143-51.

[178] Sofou S. Radionuclide carriers for targeting of cancer. Int J Nanomedicine. 2008;3:181-99.

[179] Sonnenberg A, Liem RK. Plakins in development and disease. Exp Cell Res. 2007;313:2189-203.

[180] Bausch D, Thomas S, Mino-Kenudson M, Fernandez-del CC, Bauer TW, Williams M, et al. Plectin-1 as a novel biomarker for pancreatic cancer. Clin Cancer Res. 2011;17:302-9.

[181] Shi W, Ogbomo SM, Wagh NK, Zhou Z, Jia Y, Brusnahan SK, et al. The influence of linker length on the properties of cathepsin S cleavable (177)Lu-labeled HPMA copolymers for pancreatic cancer imaging. Biomaterials. 2014;35:5760-70.

[182] Zhou Z, Wagh NK, Ogbomo SM, Shi W, Jia Y, Brusnahan SK, et al. Synthesis and In Vitro and In Vivo Evaluation of Hypoxia-Enhanced 111In-Bombesin Conjugates for Prostate Cancer Imaging. J Nucl Med. 2013;54:1605-12.

[183] DeNardo SJ, Yao Z, Lam KS, Song A, Burke PA, Mirick GR, et al. Effect of molecular size of pegylated peptide on the pharmacokinetics and tumor targeting in lymphoma-bearing mice. Clinical cancer research : an official journal of the American Association for Cancer Research. 2003;9:3854S-64S.

[184] Al-Hawary MM, Kaza RK, Wasnik AP, Francis IR. Staging of pancreatic cancer: role of imaging. Seminars in roentgenology. 2013;48:245-52.

[185] Hanada K, Okazaki A, Hirano N, Izumi Y, Teraoka Y, Ikemoto J, et al. Diagnostic strategies for early pancreatic cancer. Journal of gastroenterology. 2015;50:147-54.

[186] Bernkop-Schnurch A, Marschutz MK. Development and in vitro evaluation of systems to protect peptide drugs from aminopeptidase N. Pharmaceutical research. 1997;14:181-5.

[187] Guzman-Rojas L, Rangel R, Salameh A, Edwards JK, Dondossola E, Kim YG, et al. Cooperative effects of aminopeptidase N (CD13) expressed by nonmalignant and cancer cells within the tumor microenvironment. Proceedings of the National Academy of Sciences of the United States of America. 2012;109:1637-42.

[188] Hui M, Hui KS. A novel aminopeptidase with highest preference for lysine. Neurochemical research. 2006;31:95-102.

[189] Kakwere H, Chun CK, Jolliffe KA, Payne RJ, Perrier S. Polymer-peptide chimeras for the multivalent display of immunogenic peptides. Chem Commun (Camb). 2010;46:2188-90.

[190] Morimoto J, Sarkar M, Kenrick S, Kodadek T. Dextran as a generally applicable multivalent scaffold for improving immunoglobulin-binding affinities of peptide and peptidomimetic ligands. Bioconjugate chemistry. 2014;25:1479-91.

[191] Seo Y, Mari C, Hasegawa BH. Technological development and advances in single-photon emission computed tomography/computed tomography. Seminars in nuclear medicine. 2008;38:177-98.

[192] Liu Y, Miyoshi H, Nakamura M. Nanomedicine for drug delivery and imaging: a promising avenue for cancer therapy and diagnosis using targeted functional nanoparticles. International journal of cancer Journal international du cancer. 2007;120:2527-37.

[193] Wicki A, Witzigmann D, Balasubramanian V, Huwyler J. Nanomedicine in cancer therapy: challenges, opportunities, and clinical applications. Journal of controlled release : official journal of the Controlled Release Society. 2015;200:138-57.

[194] Zhang H. Multifunctional nanomedicine platforms for cancer therapy. Journal of nanoscience and nanotechnology. 2012;12:4012-8.

[195] McCarroll J, Teo J, Boyer C, Goldstein D, Kavallaris M, Phillips PA. Potential applications of nanotechnology for the diagnosis and treatment of pancreatic cancer. Frontiers in physiology. 2014;5:2.

[196] Chaudhari KR, Ukawala M, Manjappa AS, Kumar A, Mundada PK, Mishra AK, et al. Opsonization, biodistribution, cellular uptake and apoptosis study of PEGylated PBCA nanoparticle as potential drug delivery carrier. Pharmaceutical research. 2012;29:53-68.

[197] Wester HJ, Kessler H. Molecular targeting with peptides or peptide-polymer conjugates: just a question of size? Journal of nuclear medicine : official publication, Society of Nuclear Medicine. 2005;46:1940-5.

[198] Richmond A, Su Y. Mouse xenograft models vs GEM models for human cancer therapeutics. Disease models & mechanisms. 2008;1:78-82.

[199] Hu WG, Wang CY, Liu T, Xiong JX, Yang ZY. [Expression of sonic hedgehog, EGFR and PCNA proteins in pancreatic cancer and their correlations to cell proliferation]. Ai zheng = Aizheng = Chinese journal of cancer. 2007;26:947-51.

[200] Gorantla B, Asuthkar S, Rao JS, Patel J, Gondi CS. Suppression of the uPAR-uPA system retards angiogenesis, invasion, and in vivo tumor development in pancreatic cancer cells. Molecular cancer research : MCR. 2011;9:377-89.